

**Measurement of the Top Quark Mass by
Dynamical Likelihood Method
using the Dilepton Events
with the Collider Detector at Fermilab**

Ryo Tsuchiya

2006

**Measurement of the Top Quark Mass by
Dynamical Likelihood Method
using the Dilepton Events
with the Collider Detector at Fermilab**

Ryo Tsuchiya
(Doctoral Program in Physics)

Submitted in partial fulfillment
of the requirements for
the degree of Doctor of Philosophy

Waseda University
Tokyo, Japan
March 2006

Preface

We report the top quark mass measurement with DLM (Dynamical Likelihood Method) in the Top dilepton channel by using the CDF Run II detector at the Fermilab Tevatron Collider. For each event, the parton level kinematics is reconstructed by generating (a) the invariant mass squares for t , \bar{t} and W^\pm , (b) the b -quark energies and (c) the sum of the neutrino transverse momentum. The generating functions for (a) are propagator factors, and those for (b) and (c) are transfer functions. The differential cross-section at the parton level is used to define the likelihood of the reconstructed kinematics as a function of the top quark mass. The likelihood in an event is summed up, and the event likelihoods are multiplied each other to get the mass joint likelihood. The maximum likelihood estimate and its uncertainty was obtained by the standard treatment. The Monte Carlo Generator HERWIG with $M_t = 178 \text{ GeV}/c^2$ Top Mass Sample was used to validate the method, and we expect a statistical uncertainty of $+7.3 - 6.7 \text{ GeV}/c^2$ and a systematic uncertainty of $3.2 \text{ GeV}/c^2$. By using the 32 events observed with $\int L dt = 340.5 \text{ pb}^{-1}$ of data, we measured the top quark mass of $166.6 \text{ GeV}/c^2$.

Acknowledgments

First, I would like to thank my supervisor, Professor Kunitaka Kondo for his valuable guidance, great support, helping me understand and learn this analysis, inviting me to impressive dinner so many times and giving me the wonderful opportunity to work at Fermi laboratory and to measure the top physics described in this dissertation.

Also I would like to thank Professor Ichiro Ohba and Professor Shin-Hong Kim for all of their help and supportive mind.

I am extremely thankful to Dr. Kaori Maeshima for giving me great opportunity to work on CDF online monitoring system. The knowledge and experience on that were particular valuable things for me.

I would like to thank CDF Top and Top mass group conveners of CDF collaboration, Evelyn Thomson, Takasumi Maruyama, Douglas Glenzinski, Un-ki Yang and Eva Halkiadakis, who were very supportive and gave me precise advice and productive comments. Special thanks are due to Monica Tecchio and Daniel Whiteson, who have given me technical advice for the top measurement and shared good discussion and knowledge with me.

I am deeply grateful to Dr. Tomonobu Tomura for his continual support and valuable consultation with me. Without his encouragement and his human color, I might not have completed this analysis. Special thanks are due to Dr. Kohei Yorita for meaningful discussion and teaching me about every human life as my senior.

I am obliged to all folks at Waseda University and University of Tsukuba who have been sharing well-lived days during my Ph.D course years, and would like to express my great appreciation to so many people for helping me with substantial calculation of my analysis on CDF Central Analysis Farm.

We thank the Fermilab staff and the technical staffs of the participating institutions for their vital contributions. This work was supported by the U.S. Department of Energy and National Science Foundation; the Italian Istituto Nazionale di Fisica Nucleare; the Ministry of Education, Culture, Sports, Science and Technology of Japan; the Natural Sciences and Engineering Research Council of Canada; the National Science Council of the Republic of China; the Swiss National Science Foundation; the A.P. Sloan Foundation; the Bundesministerium für Bildung und Forschung, Germany; the Korean Science and Engineering Foundation and the

Korean Research Foundation; the Particle Physics and Astronomy Research Council and the Royal Society, UK; the Russian Foundation for Basic Research; the Comisión Interministerial de Ciencia y Tecnología, Spain; in part by the European Community's Human Potential Programme under contract HPRN-CT-2002-00292; and the Academy of Finland.

And also I quoted several figures, tables and expressions from Fermilab web page [1] and Technical Design Report of the CDF II Detector [2] due to this thesis.

Lastly, I would like to appreciate My family's incredible and terrific love and great understanding to my lives.

Contents

Preface	i
Acknowledgments	iii
1 Introduction	1
1.1 The Standard Model	2
1.1.1 The fundamental particles	2
1.1.2 Higgs mechanism	6
1.2 Top Quark Physics	10
1.2.1 The Top Quark Mass	12
2 Experimental Design	17
2.1 The Accelerator Complex	17
2.1.1 Proton Production and Boosting	19
2.1.2 Main Injector	20
2.1.3 Antiproton Production	20
2.1.4 Recycler Ring	21
2.1.5 Tevatron	21
2.1.6 Beam Monitors	21
2.2 The CDF Detector	22
2.3 Tracking System	23
2.3.1 Silicon Vertex Detector	23
2.3.2 Central Outer Tracker	24
2.3.3 Time of flight	24
2.3.4 Magnet	25
2.4 Calorimetry	25
2.4.1 Overview	25
2.4.2 Central Calorimeter	26
2.4.3 Plug Calorimeter Upgrade	27
2.5 Muon Chambers	29

2.5.1	Central Muon Detectors	32
2.5.2	Intermediate Muon Detectors	32
2.6	Data Acquisition and Trigger	32
2.6.1	Level 1 trigger	32
2.6.2	Level 2 trigger	34
2.6.3	Level 3 trigger	35
2.6.4	Online Monitoring	35
3	Event selection	37
3.1	Particle Identification	37
3.1.1	Electron Identification	37
3.1.2	Muon Identification	41
3.1.3	Jet Reconstruction	41
3.1.4	Missing Transverse Energy Reconstruction	45
3.2	Event selection	45
3.2.1	Selection criterion	46
4	Top Quark Mass Measurement	49
4.1	Dynamical Likelihood Method	49
4.1.1	General	49
4.1.2	Reconstruction of parton kinematics	51
4.1.3	DLM in dilepton channel	52
4.1.4	Neutrino kinematics	53
4.1.5	Neutrino kinematics weight	55
4.2	Transfer Function	61
4.2.1	Transfer functions for observable quantities	61
4.2.2	Jet transfer function	62
4.2.3	Missing Transverse energies transfer function	63
4.2.4	Transfer Function Summary	66
4.3	Top Quark Mass Estimation	68
4.3.1	Likelihood Calculation	68
4.3.2	Uncertainty of Likelihood	70
4.4	Background Study	74
4.4.1	Additional Event Selection	74
4.4.2	Pseudo Experiment Test	77
5	Results	83
5.1	Data	83
5.1.1	Latest result of cross section in dilepton channel	83

5.1.2	Result of Top Mass Determination	83
6	Systematic Uncertainties	87
6.1	Systematic Uncertainty	87
6.1.1	Jet Energy Scale	87
6.1.2	B Jet Energy Scale	88
6.1.3	Parton Distribution Functions (PDFs)	89
6.1.4	Initial and Final State Radiations	89
6.1.5	Generators	91
6.1.6	Background fraction	91
6.1.7	Background Modeling	92
6.1.8	Background Monte Carlo statistics	94
6.1.9	Summary of Systematics	96
7	Other Checks	97
7.1	Other Checks	97
7.1.1	Sample Quality	97
7.2	Pull Width	101
7.3	Blind Test	103
8	Conclusion	105
8.1	Conclusion	105
A	Pseudo Experiments	107

List of Figures

1.1	The <i>Standard Model</i> explains the complex interplay between force carriers and building blocks.	7
1.2	$t\bar{t}$ production processes at Tevatron.	11
1.3	$t\bar{t}$ production cross section measured at CDF in Run I ($\sqrt{s} = 1.8$ TeV) and Run II ($\sqrt{s} = 1.96$ TeV).	11
1.4	The preliminary Run II CDF result of top mass dependence for top cross section. The mean of the top mass is set by 2005 CDF+D0 combined top quark mass 172.7 ± 2.9 GeV/ c^2	12
1.5	The preliminary production cross section measurement at CDF Run II	13
1.6	A diagram for $t\bar{t}$ production by $q\bar{q}$ annihilation and its decay into lepton + jets channel.	14
1.7	Virtual top quark loops contributing to W and Z masses.	14
1.8	Virtual Higgs boson loops contributing to W and Z masses.	14
1.9	The 68% confidence level contour for m_W and m_{top} . Contours for indirect and direct measurements are plotted as well as the aimed for contour of Tevatron Run II.	16
1.10	$\Delta\chi^2 = \chi^2 - \chi_{min}^2$ vs Higgs boson mass M_H . The line shows the best fit. The blue band represents an estimate of the theoretical error due to missing higher order corrections. The vertical band shows the 95% confidence level exclusion limit on M_H from the direct search. The dashed curve is the result obtained using the evaluation of $\Delta\alpha_{had}^{(5)}(M_Z^2)$ from [3]	16
2.1	Elevation view of one half of the CDF II detector	23
2.2	Cross section of the CDF II plug calorimeter	28
2.3	η and ϕ coverage of the Run II muon systems	31
2.4	Block diagram of the CDF II Trigger	33
2.5	Design of the CDF online consumer framework.	36
3.1	The acceptance curve as the function of top quark mass for top dilepton events.	48

4.1	The difference of neutrino energies between reconstructed (solved) and generator input. The x component of neutrino energy can be solved well.	55
4.2	The difference of anti neutrino energies between reconstructed (solved) and generator input. The y component of neutrino energy can be solved well.	55
4.3	100 event joint likelihood distribution with performance (1). If we know $t\bar{t}$ full kinematics, we can reconstruct top quark mass by using DLM likelihood. Sample is generated by HERWIG MC, $M_t = 178 \text{ GeV}/c^2$	56
4.4	200 event joint likelihood distribution with performance (2). The width of reconstructed top quark mass imply the ambiguity of neutrino kinematics. Reconstructed top mass is too high against input top quark mass. Sample is generated by HERWIG MC, $M_t = 178 \text{ GeV}/c^2$	57
4.5	The probability density as a function of U variable. U_x and U_y have the same shape.	57
4.6	The probability density as a function of P_z variable. P_z and \bar{P}_z have the same shape.	57
4.7	The parameter of k for P_z depends on top quark mass. We fit them with a linear function.	58
4.8	The parameter of σ for P_z depends on top quark mass. We fit them with a linear function.	58
4.9	The parameter of k for U depends on top quark mass. We fit them with a linear function.	58
4.10	The parameter of σ for U depends on top quark mass. We fit them with a linear function.	58
4.11	Fraction of event as a function of log likelihood of an event. Red lines show the results of the calculation for only false neutrino kinematics topology. Black lines show the results of the calculation for only true neutrino kinematics topology. These figures show the separation of good/bad solutions. By adopting neutrino kinematics weight, the likelihood ratio of good/bad solutions could be enhanced by 10 times. Here the true solution means true neutrino kinematics of an event, on the contrary the false solution means other neutrino kinematics than the truth, when we solve the neutrino momenta with the use of correct resonance invariant masses.	59
4.12	2000 event joint likelihood distribution with performance (2). The likelihood we used is convoluted neutrino kinematics weight. Reconstructed top mass peak is better than Fig. 4.4 due to the effect of enhancing good solution.	60
4.13	The demonstration of jet transfer function performance. Reconstructed top invariant mass: b parton momenta are inferred by using jet transfer function, momenta of lepton and neutrino are the values at generator level.	64

4.14 Comparisons of each jet energy transfer function. The function highly depends on jet energy. 66

4.15 Comparisons of each jet eta transfer function. The function highly depends on jet energy. 67

4.16 Comparisons of each jet phi transfer function. The function highly depends on jet energy. 67

4.17 Comparisons of each MET transfer function. The function highly depends on \cancel{E}_T . 67

4.18 Comparisons of each MET phi transfer function. The function highly depends on \cancel{E}_T 67

4.19 Examples of event likelihood distribution for top signal events. 69

4.20 Reconstructed vs. input top mass for the pure sample. The straight line is the mapping function defined by Eq. (4.48). 70

4.21 Reconstructed vs. input top masses after applying the mapping function. This result shows that the masses of pure samples are well reconstructed and corrected. 71

4.22 Top histograms show examples of event likelihood distributions. Bottom histogram indicate the relative uncertainty at the event corresponding to the top histograms. 73

4.23 The typical pathological event. This event has big number of likelihood at high mass region and, on the contrary, has very small number or 0 likelihood at low mass region. Left plot shows the linear scale distribution, Right plot shows the log scale distribution. The line corresponds to $10^{-3} \times L_{max}$ 75

4.24 The typical pull distribution in which we could find unreasonable bump. 76

4.25 Additional cut efficiency as a function of input top mass. 77

4.26 The reconstructed top mass as a function of its input mass with various background fractions. The background fraction is changed from 0% to 50% with the use of sample composition for 32 events in data. 78

4.27 The fraction dependence of slopes and constant value of mapping linear fits. . . . 79

4.28 The sanity check, residual check, pull mean and pull width after applying mapping function. The sample composition is case of assumption of 6.1pb top cross section. 79

4.29 The sanity check, residual check, pull mean and pull width after applying mapping function. The sample composition is case of data. 80

4.30 The left plot shows the pull width for input top mass after the calibration in case of the assumption of 6.1pb top cross section. The right plot shows the pull width for input top mass after the calibration in case of data. 80

4.31 These are the results of pseudo experiment in case of 6.1pb top cross section assumption after mapping and calibration. Top left shows the top mass histogram, Top right shows the pull distribution in performing 500 pseudo experiment test, bottom two plots show the expected statistical uncertainties. 81

5.1	Background and signal composition of the dilepton events vs jet multiplicity after dilepton event selection except for H_T and opposite charged cut have been applied.	84
5.2	The joint natural negative log likelihood distributions of 32 events. Asymmetric quadratic fit gives $M_t = 169.95_{-3.12}^{+3.37}(stat.)\text{GeV}/c^2$	85
5.3	Maximum likelihood mass distribution for MC expectation and data. Normalization of MC expectation histogram is consistent with 32 data candidates.	86
5.4	The expected statistical uncertainty in case of data cross section assumption. Red line indicates statistical errors from data.	86
6.1	The difference of extracted top mass between the positive and negative eigenvectors set. The quadrature sum to all of the difference is $0.3 \text{ GeV}/c^2$.	90
6.2	Pull width as a function of background fraction. Red arrows indicate $\pm 5\%$ background fraction error. The fitted parameter value of p1 gives ± 0.025 fluctuation of pull width calibration.	92
6.3	The difference of Top mass, when we perform pseudo experiment at 40 times with splitting WW background sample into 2 samples.	95
6.4	The difference of Top mass, when we perform pseudo experiment at 40 times with splitting WZ background sample into 2 samples.	95
6.5	The difference of Top mass, when we perform pseudo experiment at 40 times with splitting Drell Yan background sample into 2 samples.	95
6.6	The difference of Top mass, when we perform pseudo experiment at 40 times with splitting $Z \rightarrow \tau\tau$ background sample into 2 samples.	95
6.7	The difference of Top mass, when we perform pseudo experiment at 40 times with splitting Fake background sample into 2 samples.	95
7.1	The relative fraction of each jet bin as a function of top quark masses in dilepton candidate events.	99
7.2	The marching efficiency of each number of jet as a function of top quark masses.	100
7.3	The matching efficiency and purity in the dilepton candidates as a function of top quark masses.	100
7.4	Residuals of blind samples.	104
8.1	The Tevatron Run II top mass measurements in dilepton channel. All results are consistent within the uncertainties.	106

List of Tables

1.1	Introduction and the history of six quarks. The numbers of each mass are in Particle Data Group [4].	3
1.2	Introduction and the history of six leptons. The numbers of each mass are in Particle Data Group [4].	4
1.3	Introduction and the history of four forces. The numbers of each mass are in Particle Data Group [4].	5
1.4	The relative magnitudes of the four types of interaction	6
1.5	A typical mean lifetime τ	6
1.6	Branching Ratios for $t\bar{t}$ decay modes in the Standard Model coupling. q stands for a u, d, c or s quark. Decay modes are categorized into four channels: All-jets, Lepton+jets, Di-lepton and τ channels.	15
2.1	Evolution of Tevatron parameters	18
2.2	Evolution of Tevatron parameters	19
2.3	Calorimeter segmentation. “had” means Hadoron Calorimeter.	26
2.4	Characteristics of the CDF II calorimeter. X_0 means one radiation length.	26
2.5	Parameters of muon detection at CDF.	30
3.1	Central Electron selection cuts baseline.	40
3.2	Plug Electron selection cuts baseline.	40
3.3	Muon selection cuts baseline.	42
3.4	The numbers of expected background composition with “DIL” selection in $\int Ldt = 340.5\text{pb}^{-1}$. The number of expected $t\bar{t}$ events assumes $\sigma_{t\bar{t}} = 6.7 \text{ pb}$ and $M_t = 175 \text{ GeV}/c^2$. If we assumed 6.1pb of top production cross section, the number of expectation for signal $t\bar{t}$ is decreasing to 15.66. This assumption is needed to compare analysis sensitivity with other CDF measurement.	47

4.1	Numbers for expected sample compositions after the event selection and the additional cuts. The number of expected $t\bar{t}$ events in the $t\bar{t}$ row is obtained by assuming $\sigma_{t\bar{t}} = 6.1\text{pb}$ and $M_t = 175 \text{ GeV}/c^2$. The $t\bar{t}$ total cross section of 8.8pb corresponds to the latest cross section measurement with CDF Run II 33 top dilepton candidates. The last column indicates our additional cut efficiency for likelihood calculation fails and undesirable event cuts. First column shows the numbers of event pre cut, i.e. the number after dilepton event selection.	76
6.1	The jet systematic uncertainty at each individual level of the generic jet energy corrections. Total means the output of “TotalSys” function in CDF jet correction offline tool. The value of systematics is to take a half of difference between mass values of $+\sigma$ and $-\sigma$	88
6.2	The PDF systematic uncertainty.	90
6.3	The systematic uncertainty of the initial and final state radiation.	91
6.4	The systematic uncertainty of Monte Carlo generators.	91
6.5	The results of reconstruction for enhanced Drell-Yan events.	93
6.6	The definition of weights for fake candidate event	94
6.7	The results of reconstruction for enhanced Fake candidate events.	94
6.8	The summary of systematic uncertainty of MC Background statistics.	94
6.9	The summary of systematic uncertainty.	96
7.1	The fraction of tau dilepton contamination in dilepton candidate events. Top dilepton means for two Ws decay to e/e , μ/μ or e/μ . Here tau dilepton means for two Ws decay to τ/τ , τ/e or τ/μ	98
7.2	The ratio of multiplicity in dilepton candidate events.	98
7.3	The matching efficiency and purity in the dilepton candidates. In denominator column, dilepton events means for two Ws decay to e/e , μ/μ or e/μ at generator level. Whereas dilepton candidates means including that two Ws decay to τ/τ , τ/e or τ/μ additionally. ϵ_{dil} corresponds to the fraction of top dilepton in Table 7.1.	99
7.4	The comparison of with/without neutrino kinematics weight. The sample is pure sample which is perfectly matched (jet to parton) events.	102
7.5	The comparison of jet multiplicity. The sample is pure sample which is perfectly matched (jet to parton) events.	102
7.6	The comparison of various lepton pairs. The sample is pure sample which is perfectly matched (jet to parton) events.	102
7.7	The comparison of with/without direction transfer function. The sample is pure sample which is perfectly matched (jet to parton) events.	103
7.8	The comparison between using pure sample and full sample of dilepton event. . .	103

Chapter 1

Introduction

The *nature*. It is the charming mystery to human beings all the time, because so many things inspire our sense of wonder... lots of blooming golden flowers in the field, a dense green forest, the deep blue ocean lying between the vast continents, and the ashen clear sky. More, the light of dazzling of fire, a drop of the golden sun, torrents of water, and the existence of little insects and wild mighty animals also stir our curiosity. On the past centuries, most of them of what lies beneath have been answered by so many scientists but then new questions arise again. The questions were “what is the matter?”, “what is the forces?”, the next human race has attempted to comprehend the particle physics. A significant milestone was established at the end of 19th century (1887), Thomson [5] stepped into an era to the elementary particle physics with the discovery of the electron together. Since that time, the particle physicists have tried to understand the nature at the smallest scales possible and have blossomed very successfully throughout last century. Over the past century, particle physicists have used tools of ever-increasing power to look into the matter in the continuing quest to find nature’s basic building blocks and to discover the simple physical laws that make the *nature* more understandable.

The developed high energy accelerators, providing intense and controlled beams of known energy that were finally to reveal the quark substructure of matter and put the subject on a sound quantitative basis. One of largest tools searching elementary particle today is the Tevatron collider which is located at Fermi National Accelerator Laboratory (Fermilab) in Batavia, IL in U.S.A.¹. The studies of the top quark have only been possible in the data taken in Tevatron collisions. Tevatron accelerator is designed so that the beams collide at two points along its circular length. At each point detector complexes are placed to accumulate data from these high energy particle collisions - CDF and D0 detectors. Tevatron accelerator operated during the periods 1987 - 1991 (Run 0) and 1992 - 1996 (Run I). After eight years of upgrading, it

¹Fermilab is the largest U.S. laboratory for research in high-energy physics and is second only to CERN, the European Laboratory for particle physics, in the world. About 2500 scientific users, scientists from universities and laboratories throughout the U.S. and around the world, use Fermilab for their research.

started the operation again, called Run II (2002 -).

Particle physics deals with the study of the elementary constituents of matter. The word “elementary” is used in the sense that such particles have no known structure, i.e. they are pointlike. The subject is also known as high energy physics or elementary particle physics. Experiments after 1950 have revealed whole families of short-lived particles that can be created from the energy released in the high energy collisions of ordinary particles, such as electrons or protons. The classification of these particles and the detailed understanding of the matter in which their interactions leads to the observable world have been one of the major scientific achievements of the 20th century. In 1964, almost simultaneously, Gell-Man and George Zweig independently proposed an unified scheme of baryons and mesons, the quark model [6]. Tables 1.1,1.2,1.3 show the brief introduction and the story of each elementary particle.

1.1 The Standard Model

1.1.1 The fundamental particles

Practically, all experimental phenomena from high energy experiments can be explained by the so-called *Standard Model* of particles and their interactions, formulated in the 1970s. High-precision experiments have repeatedly verified subtle effects predicted by the *Standard Model*. This theory, which is based on an $SU(3)_C \times SU(2)_L \times U(1)_Y$ gauge group, has proven extraordinarily robust. The first gauge group $SU(3)_C$ corresponds to the strong force described by Quantum Chromodynamics (QCD), and the second and third gauge groups, $SU(2)_L \times U(1)_Y$, correspond to the symmetry of the electroweak interactions. $SU(2)_L$ corresponds to the left-handed weak doublets and $U(1)_Y$ is a diagonal phase symmetry. $SU(2)_L \times U(1)_Y$ symmetry breaks into the usual V-A weak interaction and the electromagnetic force of Quantum Electrodynamics (QED) [7]. There is another known force in the nature, gravitation, but its interaction is too weak to be detected in the subatomic experiments. Therefore gravitation is not understood in terms of particle physics, and has not been included in the *Standard Model*.

The fundamental particles are categorized into three categories - leptons, quarks and gauge bosons such like box of Fig 1.1. The leptons carry integral electric charge. The electron e with unit negative charge is familiar to everyone, and the other charged leptons are the muon μ and the tau τ . These are heavy versions of the electron. The neutral leptons are called neutrinos. denoted by the generic symbol ν . A different flavor of neutrino is paired with each flavor of charged lepton, as indicated by the subscript. Neutrinos were postulated by Pauli in 1930 in order to account for the energy and momentum missing in the process of nuclear β -decay. The actual existence of neutrinos as independent particles, detected by their interactions, was first demonstrated in 1956.

The quarks carry fractional charge, of $+2/3|e|$ or $-1/3|e|$. The quark type or flavor is denoted by a symbol: u for 'up', d for 'down', c for 'charm', s for 'strange', t for 'top', b for 'bottom'.

Quark	charge	Mass (MeV/c ²)	discovery (year)	short description
1st generation				
up (<i>u</i>)	+2/3	1.5-4	1968	Physicists at the Stanford linear Accelerator Center (SLAC) observe the first evidence for quarks inside the proton. Friedman, Kendall and Taylor receive the 1990 Nobel Prize.
down (<i>d</i>)	-1/3	4-8		
2nd generation				
strange (<i>s</i>)	-1/3	80-130	1951	First observation of kaons in cosmic-ray experiments.
			1956	Nishijima of Osaka City University and Gell-Mann of Caltech explains the relative longevity of kaons with the concept of strangeness and Gell-Mann receives Nobel Prize in 1969 for the invention of the quark model.
			1964	At Brookhaven National Laboratory (BNL) Cronin and Fitch find that kaons violate the matter-antimatter (CP) symmetry. They receive the 1980 Nobel Prize.
charm (<i>c</i>)	+2/3	1.15-1.35×10 ³	1974	Physicists at SLAC and BNL discover independently a new particle that contains a new kind of quark, called the charm quark. Richter (SLAC) and Ting (BNL) receive the 1976 Nobel Prize.
3rd generation				
bottom (<i>b</i>)	-1/3	4.1-4.9×10 ³	1977	Led by Lederman, a group of scientists at Fermilab discover the upsilon, a particle containing a bottom quark and an anti-bottom quark.
top (<i>t</i>)	+2/3	1.743±0.051 × 10 ⁵	1995	The CDF and DZero collaborations at Fermilab announce the discovery of the top quark, an elementary particles as heavy as a gold atom.

Table 1.1: Introduction and the history of six quarks. The numbers of each mass are in Particle Data Group [4].

Leptons	charge	Mass (MeV/ c^2)	discovery (year)	short description
1st generation				
electron (e)	-1	0.51	1897	Using cathode tube, Thomson discovers the electron at the Cavendish laboratory in England. He receives the Nobel Prize in 1906.
electron neutrino (ν_e)	0	$< 3 \times 10^{-6}$	1956	Experimenters led by Cowan and Reines at the Savannah River plant detect the first neutrino. Reines shares the 1995 Nobel Prize.
2nd generation				
muon (μ)	-1	105.66	1937	Neddermeyer and Anderson discover the muon in a cosmic-ray experiment.
muon neutrino (ν_μ)	0	< 0.19	1962	Scientists at BNL discover the muon neutrino. Lederman, Schwartz and Steinberger receive the 1988 Nobel Prize.
3rd generation				
tau (τ)	-1	$1776.99^{+0.29}_{-0.26}$	1976	Experimenters at SLAC discover the tau lepton, the first observation of a third-generation particle. Perl shares the 1995 Nobel Prize.
tau neutrino (ν_τ)	0	< 18.2	2000	Fermilab announces first direct evidence for the interaction of a tau neutrino in a detector. Indirect indications for the existence of this particle existed since more than two decades.

Table 1.2: Introduction and the history of six leptons. The numbers of each mass are in Particle Data Group [4].

Forces	charge	Mass (MeV/c ²)	discovery (year)	short description
photon (γ)	0	$< 6 \times 10^{-17}$	1905	Based on Planck's introduction of quanta of energy, Einstein describes the photoelectric effect using light particles called photons. They are carriers of the electromagnetic force. Planck receives the 1918 Nobel Prize, and Einstein is honored in 1921.
gluon (g)	0	0	1979	At the Deutsches Elektronen-Synchrotron (DESY) in Germany, scientists report evidence for the gluon, the carrier of the strong force.
electroweak bosons				
(W)	± 1	80.43 ± 0.038	1983	Physicists at the European research CERN observe the W and Z bosons, the only force carriers with mass. Rubbia and van der Meer receive the 1984 Nobel Prize.
(Z)	0	91.19 ± 0.0021		

Table 1.3: Introduction and the history of four forces. The numbers of each mass are in Particle Data Group [4].

While leptons exist as free particles, quarks do not so. It is a peculiarity of the strong forces between the quarks that they can be found only in combinations such as uud , not singly. This phenomenon of quark confinement is even today, not properly understood.

Protons and neutrons consist of the lightest u and d quarks, three at a time: a proton consists of uud , a neutron consists of ddu . The common material of the present universe is the stable particles, i.e. the electrons e and the u and d quarks. The heavier quarks s, c, b, t also combine to form particles akin to, but much heavier than, the proton and neutron, these are unstable and decay rapidly (in typically 10^{-13} s) to u, d combinations just as the heavy leptons decay to electrons.

At the present, the *Standard Model* characterizes the interaction between the leptons and quarks as mediated by another category of particles. These mediator particles are bosons with internal spin of 1, Bose-Einstein statistics and are called gauge bosons. The four types of bosons are sufficient to explain all phenomena in physics.

1. **The strong force** is responsible for quarks “sticking” together to form protons, neutrons and related particles. The gluon mediates the strong force; it glues quarks together.
2. **The electromagnetic force** binds electrons to atomic nuclei (clusters of protons and neutrons) to form atoms. The photon carries the electromagnetic force; it is a quantized particle of light wave.

3. **The weak force** facilitates the decay of heavy particles into smaller siblings. The W and Z bosons mediate the weak force; they introduce different types of decays.
4. **The gravitational force** acts between massive objects. Although it plays no role at the microscopic level, it is the dominant force in our everyday life and throughout the universe. It has been expected that the gravitational force may also be associated with a boson particle named as the graviton.

To indicate the relative magnitudes of the four types of interaction, relative strengths of the force between two protons when just in contact are very roughly showing in Table 1.4

strong	electromagnetic	weak	gravity
1	10^{-2}	10^{-7}	10^{-39}

Table 1.4: The relative magnitudes of the four types of interaction

The timescale for the decay of unstable particles via one or other of the fundamental interactions are also very different. As detailed in Table 1.5, a typical mean lifetime τ for decay through a weak interaction is 10^{-10} s, which is easily measurable, while that for a strong interaction will be about 10^{-23} s, which cannot be measured directly. An unstable particle does not have a unique mass, but a distribution with 'width' $\Gamma = \hbar/\tau$. So, when τ is very short, its value can be inferred from the measured width Γ .

	strong	electromagnetic	weak	gravity
Typical Lifetime (seconds)	10^{-23}	10^{-20}	10^{-10}	-

Table 1.5: A typical mean lifetime τ

1.1.2 Higgs mechanism

From the very beginning of the *Standard Model* history, scientists tried to find mechanisms, that would break the $SU(2)_L \times U(1)_Y$ symmetry, allowing the mass terms of leptons and gauge bosons to be present in the Lagrangian.

We introduce a field ϕ called the Higgs field [8],

$$\phi = \begin{pmatrix} \phi^+ \\ \phi^0 \end{pmatrix} \quad (1.1)$$

which behaves as a complex scalar under Lorentz transformations and as a doublet under $SU(2)_L$ isospin transformation with isospin $T_\phi = \frac{1}{2}$ and hypercharge $Y_\phi = \frac{1}{2}$. Its kinetic, mass and interaction terms are described by the standard renormalizable Lagrangian of scalar particles:

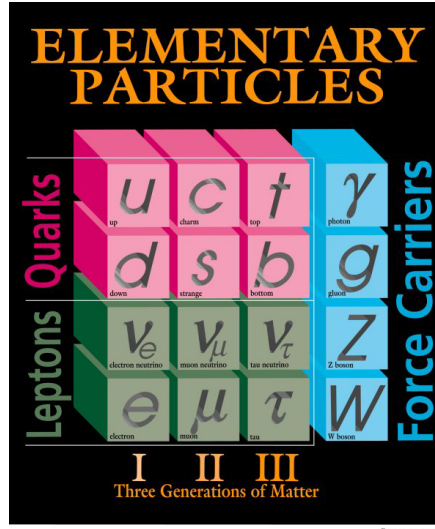


Figure 1.1: The *Standard Model* explains the complex interplay between force carriers and building blocks.

$$\mathcal{L}_{scalar} = (D_\mu \phi)^\dagger D^\mu \phi - V(\phi) \quad (1.2)$$

where the covariant derivative D_μ and the potential $V(\phi)$ are :

$$D_\mu = \partial_\mu + ig' A_\mu Y + \frac{ig}{2} \vec{\tau} \cdot \vec{b}_\mu \quad (1.3)$$

$$V(\phi) = \mu^2 \phi^\dagger \phi + \lambda (\phi^\dagger \phi)^2 \quad (1.4)$$

Notice, that μ^2 is the parameter with dimension 2. The dimensionless λ parameter is chosen to be positive in order to have the scalar potential bounded from below. The Lagrangian of Eq. (1.2) is invariant under $SU(2)_L \times U(1)_Y$ symmetry, therefore we can add it to the electroweak Lagrangian

$$\mathcal{L}_{EWK} = \mathcal{L}_{gauge} + \mathcal{L}_{lepton} + \mathcal{L}_{quark} \quad (1.5)$$

where,

$$\mathcal{L}_{lepton} = \sum_{l=e,\mu,\tau} \bar{R}_l i \gamma^\mu (\partial_\mu + ig' A_\mu Y) R_l \quad (1.6)$$

$$+ \sum_{l=e,\mu,\tau} \bar{L}_l i \gamma^\mu (\partial_\mu + ig' A_\mu Y + \frac{ig}{2} \vec{\tau} \cdot \vec{b}_\mu) L_l \quad (1.7)$$

where,

$$R_l = e_R, \mu_R, \tau_R \quad (1.8)$$

$$L_e = \begin{pmatrix} \nu_e \\ e^- \end{pmatrix}, \begin{pmatrix} \nu_\mu \\ \mu^- \end{pmatrix}, \begin{pmatrix} \nu_\tau \\ \tau^- \end{pmatrix} \quad (1.9)$$

$$\mathcal{L}_{quark} = \sum_{q=u,d,c,s,t,b} \bar{R}_q i\gamma^\mu (\partial_\mu + ig' A_\mu Y) R_q \quad (1.10)$$

$$+ \sum_{q=1,2,3} \bar{L}_q i\gamma^\mu (\partial_\mu + ig' A_\mu Y + \frac{ig}{2} \vec{\tau} \cdot \vec{b}_\mu) L_q \quad (1.11)$$

where,

$$R_q = u_R, d_R, c_R, s_R, t_R, b_R \quad (1.12)$$

$$L_e = \begin{pmatrix} u_L \\ d_L \end{pmatrix}, \begin{pmatrix} c_L \\ s_L \end{pmatrix}, \begin{pmatrix} t_L \\ b_L \end{pmatrix} \quad (1.13)$$

$$\mathcal{L}_{gauge} = -\frac{1}{4} F_{\mu\nu}^a F_a^{\mu\nu} - \frac{1}{4} f_{\mu\nu} f^{\mu\nu} \quad (1.14)$$

with

$$f_{\mu\nu} = \partial_\nu A_\mu - \partial_\mu A_\nu, \quad F_{\mu\nu}^a = \partial_\nu b_\mu^a - \partial_\mu b_\nu^a + g\epsilon_{jk}^a b_\mu^j b_\nu^k \quad (1.15)$$

if $\mu^2 > 0$, then the Lagrangian \mathcal{L}_{scalar} describes a QED theory with a massless photon A_μ and two real scalar particles ϕ and ϕ^* with the same mass $\sqrt{\mu^2}$. Interesting thing happens, if we consider the other case, namely $\mu^2 < 0$. Then the scalar potential $V(\phi)$ has a non-vanishing minimum and the Higgs field gets a non-zero vacuum expectation value $\langle \phi^\dagger \phi \rangle = -\frac{1}{2}\mu^2/\lambda$. By choosing the vacuum expectation value (VEV) of the Higgs to be

$$\langle \phi \rangle = \begin{pmatrix} 0 \\ v/\sqrt{2} \end{pmatrix} \quad (1.16)$$

where $v/\sqrt{2} \equiv \sqrt{(-\frac{1}{2}\mu^2)/\lambda}$, we can redefine the field ϕ of Eq. (1.1) by introducing four new real scalar fields $\vec{\xi}(x), H(x)$ by the expression :

$$\phi(x) \equiv \exp\left(\frac{i\vec{\xi}(x) \cdot \vec{\tau}}{2v}\right) \begin{pmatrix} 0 \\ (v + H(x))/\sqrt{2} \end{pmatrix} \quad (1.17)$$

by choosing $\vec{\beta} = \frac{\vec{\xi}}{gv}$ in the $SU(2)$ gauge transformations, we can eliminate the $\vec{\xi}$ field such a way that we obtain for the Higgs field the following form:

$$\phi(x) \rightarrow \phi'(x) = \frac{1}{\sqrt{2}} \begin{pmatrix} 0 \\ (v + H(x)) \end{pmatrix} \quad (1.18)$$

Substituting 1.18 into \mathcal{L}_{scalar} in Eq. (1.2) we obtain

$$\mathcal{L}_{scalar} = \frac{1}{2}(\partial_\mu H(x))^2 + \frac{1}{4}g^2 W_\mu^+ W^{-\mu}(v + H(x))^2 \quad (1.19)$$

$$+ \frac{1}{8} \frac{e^2}{\sin^2 \theta_W \cos^2 \theta_W} Z_\mu^0 Z^{0\mu} (v + H(x))^2 \quad (1.20)$$

$$+ (\mu^2 (\frac{1}{2}(v + H(x))^2)) + \lambda (\frac{1}{4}(v + H(x))^4) \dots \quad (1.21)$$

where $\gamma_\mu = A_\mu \cos \theta_W + b_\mu^3 \sin \theta_W$, $Z_\mu^0 = -A_\mu \sin \theta_W + b_\mu^3 \cos \theta_W$, $W_\mu^\pm = \frac{b_\mu^1 \mp i b_\mu^2}{\sqrt{2}}$ are the physical states, of the photon γ , Z_μ^0 , and W^\pm vector bosons. Note that the neutral Higgs field does not couple to the photon. After regrouping Eq. (1.21) we can read out the Higgs and gauge bosons masses.

$$m_H^2 = -2\mu^2 = 2\lambda v^2 \quad (1.22)$$

$$m_W = g \frac{v}{2} \quad (1.23)$$

$$m_Z = \frac{m_W}{\cos^2 \theta_W} \quad (1.24)$$

$$m_\gamma = 0 \quad (1.25)$$

By introducing the Higgs field, so far we were able to give masses to the vector bosons, but the scalar field is still decoupled from the fermionic sector and the fermions are still massless. The solution to this problem is hidden in the Yukawa coupling terms, which for the first family read:

$$\mathcal{L}_{Yukawa} = -(\lambda_u \bar{R}_u \bar{\phi}^\dagger \cdot L_u + \lambda_d \bar{R}_d \phi^\dagger \cdot L_d + \lambda_e \bar{R}_e \phi^\dagger \cdot L_e + h.c.) \quad (1.26)$$

where λ_u , λ_d and λ_e are the Yukawa coupling constants. This Lagrangian is also invariant under electroweak symmetry and can be added to Eq. (1.5). We demonstrate how fermions acquire mass by using the first family leptons only. By plugging the Higgs field from 1.18 into \mathcal{L}_{Yukawa} we obtain the electron mass term as well as a term describing the coupling of the Higgs to electrons,

$$\mathcal{L}_{Yukawa}^{electron} = -\lambda_e \frac{v + H(x)}{\sqrt{2}} (\bar{e}_R e_L + \bar{e}_L e_R) = -m_e \bar{\psi}_e \psi_e - \frac{\lambda_e}{\sqrt{2}} H \bar{\psi}_e \psi_e \quad (1.27)$$

where the electron mass is

$$m_e = \frac{v\lambda_e}{\sqrt{2}} \quad (1.28)$$

Similar procedure applies to the leptonic members of other families and to quarks.

The *Standard Model* has successfully explained many phenomena observed in particles physics experiments over several decades, and no clear sign of its contradiction with nature has been reported yet. On the other hand, it is fundamental to feed the correct input parameters in order for this theory to work. The mass of the top quark is one of such input parameters which the Standard Model is incapable of predicting. Especially, the interesting thing is the fact that the mass of the top quark is by far the heaviest among the elementary particles discovered so far. At the same time, it is an exciting coincidence that the mass of the top quark is very close to the vacuum expectation value of the *Standard Model*. The precision measurement of the top quark mass will play an important role in revealing the mechanism of the Electroweak Symmetry Breaking, and at the same time, closely related to the properties of the Higgs particle, the only particle yet to be discovered in the *Standard Model*.

1.2 Top Quark Physics

The discovery of the top quark in 1995 provided dramatic confirmation of the essential validity of the *Standard Model* of particle physics, since the top quark is the last of the known or needed constituents of matter. Fermilab scientists have been searching top quark physics for past 10 years since its discovery by using Fermilab Tevatron. Several properties of the top quark have already been examined at the CDF Run II experiment, one of experiments for Fermilab Tevatron. These include studies of the top production cross-sections [9, 10, 11, 12, 13], of the measurements of the top mass [14, 15, 16], of the search for single top quark production [17], of the search for anomalous kinematics [18], of the measurement for top branching ratio to W decay [19], of the τ decays for top quark [20] and of search for charged Higgs Bosons [21].

The top quark is, according to the *Standard Model*, a spin-1/2 and charge-2/3 fermion, transforming as a color triplet under the group $SU(3)_C$ of the strong interactions and as the weak-isospin partner of the bottom quark. None of these quantum numbers has been directly measured so far, although a large amount of indirect evidence supports these assignments.

The top quark is produced predominantly in top-antitop pairs at the Tevatron via the strong interaction. At a center of mass energy \sqrt{s} of 1.96 TeV, the processes $q\bar{q} \rightarrow t\bar{t}$ and $gg \rightarrow t\bar{t}$ occur approximately 85% and 15% of the time, respectively. The leading order diagrams for the two processes are shown in Fig. 1.2. The total cross section for the pair production of top quark is theoretically calculated to be $6.7^{+0.7}_{-0.9}$ pb [22]. Figure 1.3 summarizes the total cross section

measured at CDF experiment in Run I and Run II compared to the prediction of the *Standard Model*. And also, the latest CDF Run II result is presented as can be seen Figs. 1.4 and 1.5

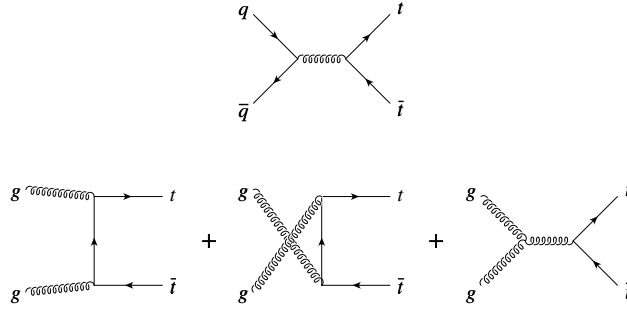


Figure 1.2: $t\bar{t}$ production processes at Tevatron.

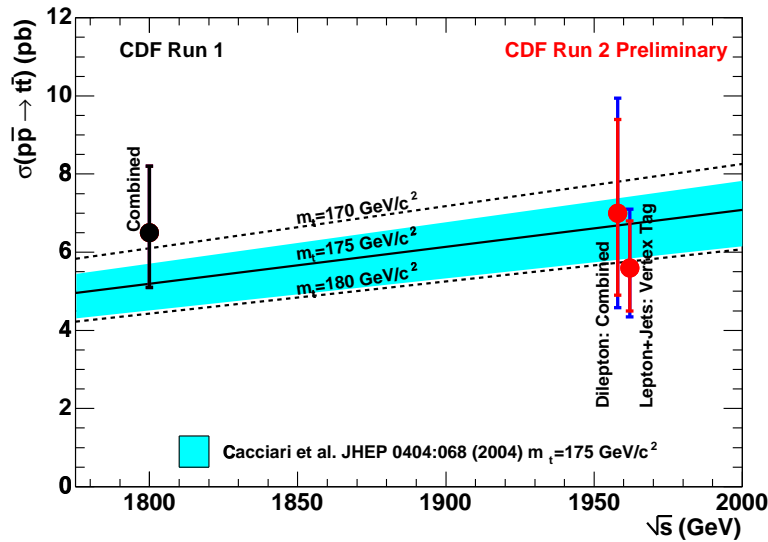


Figure 1.3: $t\bar{t}$ production cross section measured at CDF in Run I ($\sqrt{s} = 1.8$ TeV) and Run II ($\sqrt{s} = 1.96$ TeV).

The top quark decay is mediated by the electroweak interaction. Flavor changing neutral currents are forbidden in the *Standard Model* due to the GIM mechanism [23]. According to the *Standard Model*, top quark decays 100% of the time into a W boson and a b quark. The decays are rapid without forming hadrons, and occur almost exclusively through the single mode $t \rightarrow Wb$. The final signatures of the $t\bar{t}$ production are categorized into four categories, di-lepton, lepton+jets, all-hadronic and τ channels, due to the decay modes of the two W bosons produced in the decays of top and anti-top quarks. Although the τ particle is a lepton, its identification requires a complicated analysis technique [24] due to its short lifetime and decay modes involving

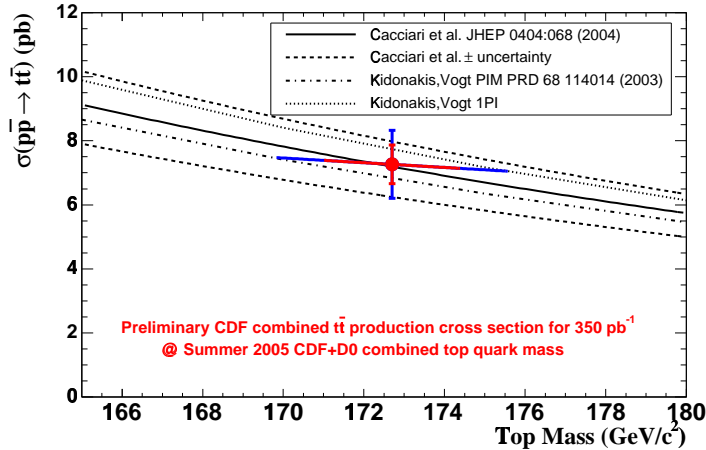


Figure 1.4: The preliminary Run II CDF result of top mass dependence for top cross section. The mean of the top mass is set by 2005 CDF+D0 combined top quark mass $172.7 \pm 2.9 \text{ GeV}/c^2$.

τ particles are categorized into an independent channel.

Figure 1.6 is a diagram showing the lepton + jets decay of $t\bar{t}$ pair. Table 1.6 summarizes the categorization of the decay modes, with the branching ratio at the tree-level.

1.2.1 The Top Quark Mass

In addition to its quantum numbers, the top quark mass is one of most fundamental properties of the top quark. Therefore, CDF Run II Top group also has taken a lot of effort to determine its mass precisely. Thereby, the main purpose of this thesis is to measure this top quark mass as well.

The mass of the top quark is related to the mass of the Higgs boson. Properties of the Higgs field associated with this particle would help to explain why matter is, not to put too fine a point on it, 'massive.' In principle, the top quark is point-like and should have no mass; yet, through its interactions with the Higgs field, the physical mass of the top quark appears to be about that of a gold nucleus. Because it is so heavy, the top quark provides an unusually sensitive tool for investigating the Higgs field. Well-constrained values for the top-quark mass will enable researchers to predict the mass of the Higgs particle, eliminating untenable various theoretical fixes for deficiencies in the *Standard Model*, while supporting others.

Furthermore, as illustrated below, a precise measurement of the mass of the top quark, along with that of the W boson, provides a constraint on the mass of the Higgs boson. Such a constraint can bring us a hint in the search for the Higgs boson. At the tree level calculation of the *Standard Model*, there is an equation,

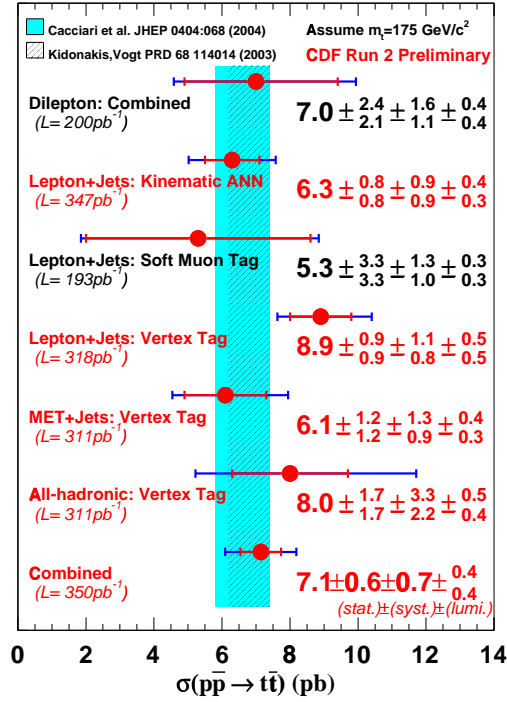


Figure 1.5: The preliminary production cross section measurement at CDF Run II

$$M_W^2 = \frac{\frac{\pi\alpha}{\sqrt{2}G_F}}{\sin^2 \theta_W} \quad (1.29)$$

where M_W , α , G_F and θ_W are the mass of W boson, the fine structure constant, the Fermi coupling constant and the electroweak mixing angle, respectively. At one loop calculation, this expression is modified :

$$M_W^2 = \frac{\frac{\pi\alpha}{\sqrt{2}G_F}}{\sin^2 \theta_W (1 + \Delta r)} \quad (1.30)$$

where Δr contains the one-loop corrections [25]. The top quark makes a contribution to Δr via the one loop diagrams shown in Figure 1.7, which contribute to the W and Z masses :

$$(\Delta r)_{top} \approx -\frac{3G_F m_t^2}{8\sqrt{2}\pi^2} \frac{1}{\tan^2 \theta_W} \quad (1.31)$$

The Higgs boson also contributes to Δr via diagrams shown in Figure 1.8 :

$$(\Delta r)_{Higgs} \approx \frac{11G_F M_Z^2 \cos^2 \theta_W}{24\sqrt{2}\pi^2} \ln \frac{m_h^2}{M_Z^2} \quad (1.32)$$

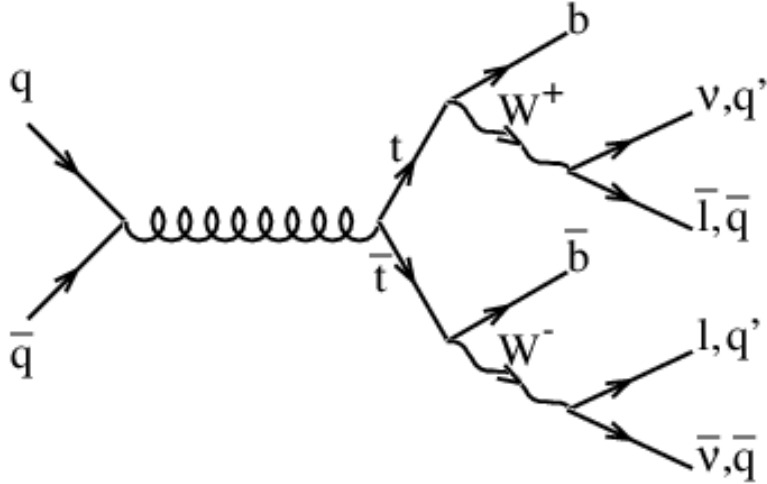


Figure 1.6: A diagram for $t\bar{t}$ production by $q\bar{q}$ annihilation and its decay into lepton + jets channel.

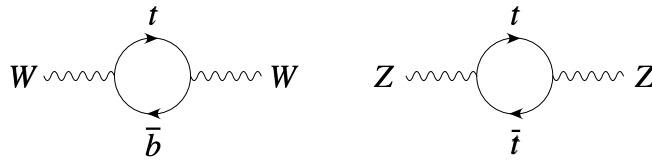


Figure 1.7: Virtual top quark loops contributing to W and Z masses.

Figure 1.9 shows the current Run II 68% confidence level contour for M_W and m_{top} for both indirect and direct measurements [26].

The indirect measurement was obtained using results from SLD and LEP collaborations. The direct measurement of M_W is the average of LEP and Tevatron Run I, and the m_{top} is the average of Tevatron Run I. The aim for size of the uncertainty at 2 fb^{-1} in Tevatron Run II is also shown. The Standard Model relationship for the masses as a function of the Higgs mass due to the one-loop corrections is also shown in the figure.

Figure 1.10 further shows the χ^2 as a function of the Higgs mass obtained in a fit of the *Standard Model* to the electroweak measurements of LEP, SLD and Tevatron Run I collaborations,



Figure 1.8: Virtual Higgs boson loops contributing to W and Z masses.

Decay mode	Branching Ratio	Channel Category
$t\bar{t} \rightarrow (q\bar{q}'b)(q\bar{q}'\bar{b})$	36/81	All-hadronic
$t\bar{t} \rightarrow (q\bar{q}'b)(e\nu\bar{b})$	12/81	Lepton+jets
$t\bar{t} \rightarrow (q\bar{q}'b)(\mu\nu\bar{b})$	12/81	Lepton+jets
$t\bar{t} \rightarrow (q\bar{q}'b)(\tau\nu\bar{b})$	12/81	τ channel
$t\bar{t} \rightarrow (e\nu b)(\mu\nu\bar{b})$	2/81	Di-lepton
$t\bar{t} \rightarrow (e\nu b)(\tau\nu\bar{b})$	2/81	τ channel
$t\bar{t} \rightarrow (\mu\nu b)(\tau\nu\bar{b})$	2/81	τ channel
$t\bar{t} \rightarrow (e\nu b)(e\nu\bar{b})$	1/81	Di-lepton
$t\bar{t} \rightarrow (\mu\nu b)(\mu\nu\bar{b})$	1/81	Di-lepton
$t\bar{t} \rightarrow (\tau\nu b)(\tau\nu\bar{b})$	1/81	τ channel

Table 1.6: Branching Ratios for $t\bar{t}$ decay modes in the Standard Model coupling. q stands for a u, d, c or s quark. Decay modes are categorized into four channels: All-jets, Lepton+jets, Di-lepton and τ channels.

including the measurements of the top quark mass [26].

Direct searches for Higgs production at LEP have excluded $M_H < 114.4\text{GeV}/c^2$ [27] at 95 % confidence level. While waiting for the discovery of the Higgs, information on the upper limit of M_H is the best possible progress in determining this basic parameter of the SM. The 95% confidence level upper limit for the Higgs boson mass due to the χ^2 curve is $260\text{ GeV}/c^2$ [26].

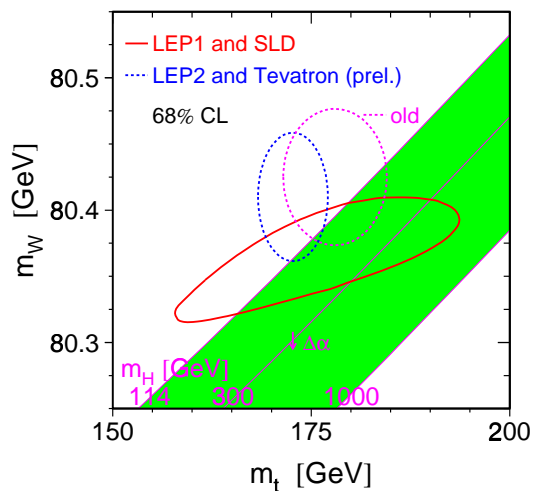


Figure 1.9: The 68% confidence level contour for m_W and m_{top} . Contours for indirect and direct measurements are plotted as well as the aimed for contour of Tevatron Run II.

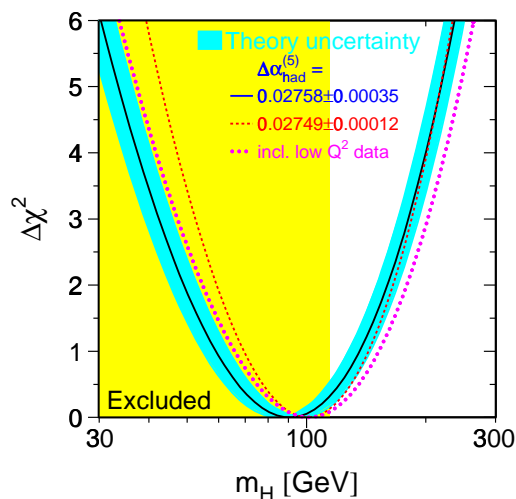


Figure 1.10: $\Delta\chi^2 = \chi^2 - \chi_{min}^2$ vs Higgs boson mass M_H . The line shows the best fit. The blue band represents an estimate of the theoretical error due to missing higher order corrections. The vertical band shows the 95% confidence level exclusion limit on M_H from the direct search. The dashed curve is the result obtained using the evaluation of $\Delta\alpha_{had}^{(5)}(M_Z^2)$ from [3]

Chapter 2

Experimental Apparatus

Particle accelerators are mainly known for their application as research tools in nuclear and high energy particle physics requiring the biggest and most energetic facilities. The Fermilab Tevatron Collider is currently the world's highest energy accelerator, colliding anti-protons with protons at a center of mass energy of 1.96 TeV. The CDF (Collider Detector experiment at Fermilab) is an international collaboration of about 500 Physicists (from about 30 American universities and National laboratories, etc, plus also from about 30 groups from universities and national laboratories from Italy, Japan, UK, Canada, Germany, Spain, Russia, Finland, France, Taiwan, Korea, Switzerland, etc.). We have built the 100-ton CDF detector (about 40' high by 40' x 40' base) at the Fermilab Tevatron collider. The CDF Detector is a complex detector which measures most of the interesting particles that come out of the P-bar P collision. 2 Intense beams (about 10^{14} to 10^{15} particles each) of protons and anti-protons meet head-on in the middle of the CDF detector, and a few collisions occur every time 2 bunches collide (this happens every 120 nsec—or about 1/8-million seconds).

2.1 The Accelerator Complex

In the past decade, CDF planed to carry out precise analysis of several rare physical processes whose cross section is several orders of magnitude smaller than the inelastic $p\bar{p}$ cross section. In order to obtain sufficiently large samples, several steps have been taken:

- Increase the center-of-mass energy
- Increase the luminosity
- Increase the detector's acceptance

The first two steps, and the partial reconstruction of the Tevatron, are the topic of this section.

As was stated above, the Run II proton-antiproton center of mass energy has increased to 1.96 TeV from the Run I value of 1.8 TeV. This change provides a major increase in the reconstructed sample size; for example, the cross section for associated $t\bar{t}$ production grows by 40% with respect to Run I.

Another way to obtain a larger sample is to increase the accelerator's luminosity. In the ideal case, where the proton and antiproton beams collide head-on without a crossing angle and with optimal alignment, the Tevatron's luminosity is given by the formula

$$\mathcal{L} = \frac{fBN_pN_{\bar{p}}}{2\pi(\sigma_p^2 + \sigma_{\bar{p}}^2)} F\left(\frac{\sigma_l}{\beta^*}\right) \quad (2.1)$$

where f is the revolution frequency, B the number of bunches in each beam, N_p and $N_{\bar{p}}$ the number of protons and anti-protons per bunch, σ_p and $\sigma_{\bar{p}}$ the transverse beam sizes (RMS) at the interaction point, and F a form factor that depends on the ratio between the bunch longitudinal RMS size, σ_l , and the beta function¹ at the interaction point, β^* .

Run	1989	IA (1992-93)	IB (1993-95)
p /bunch	7.00E+10	1.20E+11	2.32E+11
\bar{p} /bunch	2.90E+10	3.10E+10	5.50E+10
p emittance (mm mrad)	25	20	23
\bar{p} emittance (mm mrad)	18	12	13
Beta @@ IP (m)	0.55	0.35	0.35
Energy (GeV/particle)	900	900	900
Bunches	6	6	6
Bunch length (rms, m)	0.65	0.55	0.6
Form Factor	0.71	0.62	0.59
Typical \mathcal{L} (cm ⁻² s ⁻¹)	1.60E+30	5.42E+30	1.58E+31
Best \mathcal{L} (cm ⁻² s ⁻¹)	2.05E+30	9.22E+30	2.50E+31
$\int \mathcal{L} dt$ (pb ⁻¹ /week)	0.32	1.09	3.18
Bunch Spacing (nsec)	3500	3500	3500
Interactions/crossing	0.25	0.85	2.48
What's New?		Separators \bar{p} improvements	Linac Upgrade

Table 2.1: Evolution of Tevatron parameters.

As shown in Table 2.1 and Table 2.2, the most significant improvements in luminosity are obtained by increasing the number of bunches per beam from 6 to 36, while keeping the number of particles per bunch similar to or higher than the Run I figure.

¹Supposing the profile of the beam in the phase space (x, x') is an ellipse of semi-axes σ and σ' , the *amplitude function* β is defined as the ratio σ/σ' , while the beam *emittance* is the phase volume $\epsilon = \pi\sigma\sigma'$.

Run	II (2001-)
p /bunch	3.30E+11
\bar{p} /bunch	3.60E+10
p emittance (mm mrad)	30
\bar{p} emittance (mm mrad)	20
Beta @@ IP (m)	0.35
Energy (GeV/particle)	980
Bunches	36
Bunch length (rms, m)	0.43
Form factor	0.70
Typical \mathcal{L} ($\text{cm}^{-2}\text{s}^{-1}$)	4-10E+31
$\int \mathcal{L} dt$ ($\text{pb}^{-1}/\text{week}$)	8
Bunch Spacing (nsec)	396
Interactions/crossing	2.17
What's New?	Main Injector \bar{p} improvements

Table 2.2: Evolution of Tevatron parameters.

A limiting factor in the choice of accelerator parameters is the superposition of multiple elementary proton-antiproton interactions within the same bunch crossing. At high luminosities, this superposition increases the complexity of the event, making its reconstruction more difficult.

Production and acceleration of protons and anti-protons at Fermilab require a chain of accelerators, each boosting particles to higher energies. Each step will be described in the following.

2.1.1 Proton Production and Boosting

The process begins with a **Cockcroft-Walton** accelerator, which feeds negative hydrogen ions to a 150 m linear accelerator. The Linac itself was upgraded in 1993, increasing its energy from 200 MeV to 400 MeV; this made it possible, during Run Ib, to double the number of protons per bunch, and to increase by about 50% the production rate of antiprotons.

After being stripped of electrons, the protons enter the **Booster**, a synchrotron whose diameter is about 150 m, where they reach a kinetic energy of 8 GeV. Together, Linac and Booster are able to provide pulses of $5 \cdot 10^{12}$ protons for antiproton production every 1.5 s, or $6 \cdot 10^{10}$ protons per bunch in series of 5 to 7 bunches, repeated 36 times every four seconds.

After leaving the Booster, protons are transferred to the Main Injector, a newly built circular accelerator that replaced the older Main Ring.

2.1.2 Main Injector

The Main Ring was originally built to provide 400 GeV protons to Fermilab's fixed target experiments; later on, it was converted to act as an injector to the Tevatron. The new operational requirements for the Main Ring did not match its original design; therefore, during Run I, the Main Ring was a performance bottleneck. To quote an example, the Main Ring's aperture (12π mm mrad)² is only 60% of the Booster's aperture (20π mm mrad). The situation would be even worse in Run II, with the Booster's aperture at injection increasing to 30π mm-mrad.

The **Main Injector** was designed to solve this problem, while providing further benefits. It is a 3-km circular accelerator, which brings protons and anti-protons from a kinetic energy of 8 GeV to a total energy of up to 150 GeV. Its transverse admittance is larger than 40π mm mrad, more than enough to accommodate particle bunches from the Booster; its emittance is about 12π mm mrad. The maximum beam size is $3 \cdot 10^{13}$ particles, divided into up to 504 bunches of $6 \cdot 10^{10}$ (anti)protons.

Being more flexible than the Main Ring, the Main Injector can be used in several operation modes:

- Antiproton production;
- Proton and antiproton boosting, before injection into the Tevatron in collider mode;
- Antiproton deceleration, in order to recover unused anti-protons after a Tevatron collision run;
- Proton and antiproton acceleration for fixed target experiments, either directly or as a booster for the Tevatron.

2.1.3 Antiproton Production

In order to produce anti-protons, a pulse of $5 \cdot 10^{12}$ protons at 120 GeV is extracted from the Main Injector and focused on a nickel target. A lithium lens collects the anti-protons produced by the collision, with a wide acceptance around the forward direction, at energies close to 8 GeV. The antiproton bunches are then moved to a **Debuncher Ring**, where they are transformed into a continuous beam and stochastically cooled, and then to the **Accumulator**, where they are further cooled. The antiproton stacking rate during Run I was about $7 \cdot 10^{10}$ \bar{p} /hour; Run II upgrades, ranging from antiproton cooling to improving the lithium lens, increases this rate by a factor of three to four.

When a sufficient number of anti-protons (up to 10^{12}) is available, stacking is suspended; the anti-protons are further cooled, and then transferred, with an aperture of 10π mm mrad and a $\Delta p/p < 10^{-3}$, to the antiproton Recycler Ring.

²All emittance are normalized at 95% of the beam.

2.1.4 Recycler Ring

The **Recycler Ring** lies in the same enclosure as the Main Injector; contrarily to the other rings at Fermilab, it is built with permanent magnets. During Run I, the antiproton accumulation ring was found to suffer some kind of failure approximately once a week; this led to the loss of the entire store. Permanent magnets, not being prone to the most common causes of failure (such as power loss and lightning) provide a very stable repository for up to $3 \cdot 10^{12}$ anti-protons at a time.

During Run II, bunches of $2 \cdot 10^{11}$ recently produced anti-protons are transferred from the Accumulator to the Recycler Ring every about half an hour, thus keeping the total beam current in the Accumulator small (below 10 mA, compared to the 200 mA antiproton current in Run I).

Antiproton production is one of the limiting factors in the efficiency of Fermilab's colliders. At the end of a store, 75% of the antiprotons are expected to be still circulating in the Tevatron; by recycling 2/3 of these anti-protons, the average luminosity can be increased by a factor of two.

2.1.5 Tevatron

The Tevatron is about 6-km circular accelerator, where protons and anti-protons, rotating in opposite directions inside the same beam pipe, are accelerated from 150 GeV to 1 TeV. Making use of the upgrades in the rest of the accelerator chain, the Tevatron can provide an initial luminosity of $5 \cdot 10^{31} \text{ cm}^2 \text{ s}^{-1}$.

During a collider store, instant luminosity slowly decreases. In the early stages of the store, the most important cause for this decrease is intrabeam scattering; some hours later, the depletion of anti-protons during collisions becomes more relevant. Luminosity is expected to decrease to 50% in about seven hours, and to $1/e$ in twelve hours. After a typical store duration of eight hours, 75% of the antiprotons are still available; they are decelerated in the Tevatron and in the Main Injector, and then stored in the Recycler Ring and re-cooled Recycler is not used for the current $\bar{p}p$ collisions.

The Tevatron can also be used in fixed-target mode: it can accelerate up to $3 \cdot 10^{13}$ protons at a time to an energy of 800 GeV, and deliver single bunches to be used in proton, meson and neutrino experiments.

Other operational parameters of the Tevatron are listed in Table 2.1 and Table 2.2.

2.1.6 Beam Monitors

Operation of colliders at the Tevatron requires a constant monitoring of the beam position and luminosity. From a conceptual point of view, this is done in Run II as it was done in Run I.

The luminosity monitor consists in two arrays of scintillators, placed on both sides of the interaction region. A coincidence of particles moving away from the interaction point, both in

the p and \bar{p} direction, is interpreted as a contribution to luminosity; bunches of particles moving in a single direction, without a coincident bunch in the opposite direction, are flagged as beam losses.

The beam position, on the other hand, is measured by the collider detectors themselves. During Run I, the detector was able to locate the beam within $5 \mu\text{m}$ in about five minutes; other beam parameters, such as slope and transverse profile, were calculated over longer time intervals (about two hours). In Run II, the same operations are performed more quickly.

2.2 The CDF Detector

As stated above, one of the aims of Run II is to reconstruct and store a large sample of rare events. To achieve this result, the number of bunches in each beam increased first by a factor of six with respect to Run I. An immediate consequence is that the time between two successive interactions decreased by the same factor. Several parts of the detectors have been rebuilt from scratch in order to accommodate the higher collision rate.

While the detector was redesigned, efforts were also made to extend its acceptance. The geometrical coverage was increased, by adding new detector elements or enlarging the previously existing ones; the trigger system became able to detect some interesting event features at an earlier stage than in Run I, thus improving the signal to background ratio.

As shown in Fig. 2.1, the tracking system of CDF II is placed inside a superconducting solenoid, while calorimeter and muon systems are outside the magnet. The rest of this chapter will provide a short description of the detector subsystems, with an emphasis on the upgrades since Run I. A complete description of CDF can be found in [28].

In the standard CDF geometry, the \hat{z} axis is oriented along the axis of the solenoid, the \hat{x} axis points away from the center of the Tevatron, and the \hat{y} axis points up. The origin is at the interaction point. The polar angle θ is measured starting from the positive \hat{z} axis; the rapidity y is defined by

$$y = \frac{1}{2} \ln \left(\frac{E + p_z}{E - p_z} \right) \quad (2.2)$$

For the high energy particles, $E \sim p$ and $p_z = p \cos \theta$, hence the pseudo-rapidity is defined as

$$\eta = -\ln \left(\tan \frac{\theta}{2} \right) \quad (2.3)$$

In hadron-hadron collisions, a rapidity y (or pseudo-rapidity η), a transverse momentum p_T and an azimuth angle ϕ are usually used. The invariant cross section is written as

$$E \frac{d^3\sigma}{d^3p} = \frac{d^3\sigma}{d\phi dy p_T dp_T} \rightarrow \frac{d^2\sigma}{\pi dy dp_T^2} \quad (2.4)$$

The second form is obtained using the identity $dy/p_z = 1/E$, and the third form represents the average over ϕ . The total multiplicity of particles in collisions is given by $d\sigma/dy$ and this means that the multiplicity is flat in η .

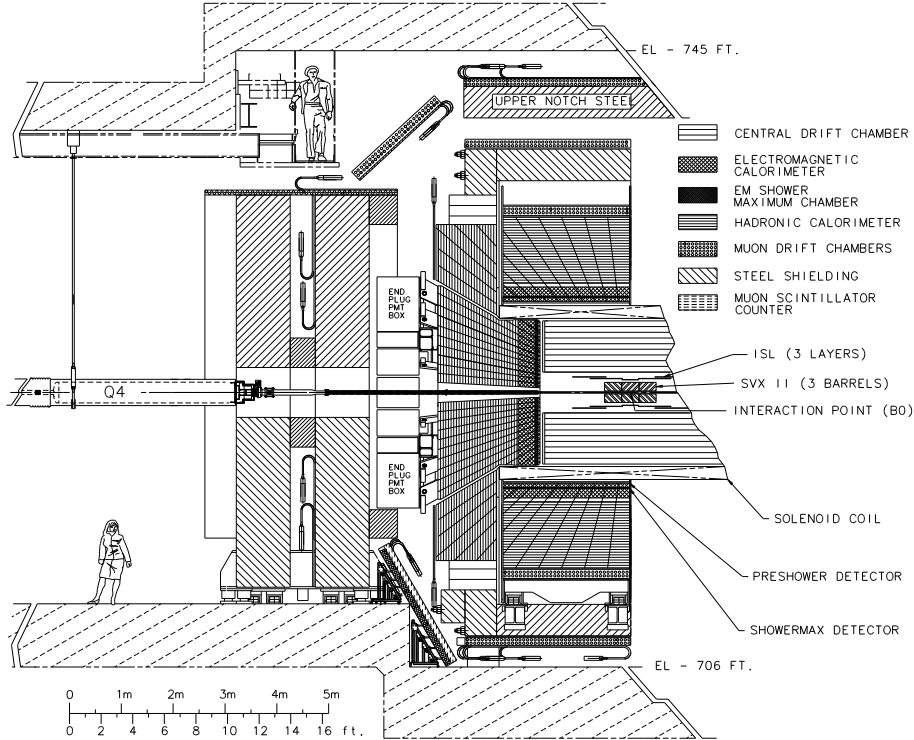


Figure 2.1: Elevation view of one half of the CDF II detector

2.3 Tracking System

The innermost parts of the CDF II detector are devoted to tracking charged particles.

2.3.1 Silicon Vertex Detector

CDF II makes use of three concentric silicon detectors: “Layer 00” (**L00**), the Silicon Vertex Detector (**SVX II**, or **SVX** in short), and the Intermediate Silicon Layers (**ISL**) [29].

SVX II is the Run II baseline detector. It consists of five layers of double-sided silicon wafers. One side of each wafer provides measurements in the transverse plane (axial strips); the other side’s strips deliver 3D information. SVX II extends radially from 2.5 to 10 cm, and along z up to 45 cm on either side of the interaction point.

The ISL consists of a double-sided silicon layer, similar to those in SVX II, placed at $r = 22$ cm in the central η region, and of two forward layers ($1 < |\eta| < 2$) respectively at 20 and

29 cm from the beam line. Together with SVX II, the ISL makes it possible to reconstruct tracks in the forward region, which lies beyond the acceptance region of the outer tracker.

Layer 00 is the most recent addition to the CDF II tracker. It is a single sided, radiation-hard silicon layer, placed immediately outside the beam pipe, at $r \simeq 1.5$ cm. Being so close to the interaction point, Layer 00 improves noticeably the impact parameter resolution. In case the innermost SVX II layer suffers from radiation damage during Run II, Layer 00 also acts as a backup.

Compared to the shorter, 4-layer, single-sided vertex detector of Run I, the new silicon tracker provides a much wider acceptance, better resolution, three-dimensional reconstruction, and can be used in stand-alone mode, without input from the Central Outer Tracker (described hereafter).

2.3.2 Central Outer Tracker

Outside the silicon detector, at a distance between 40 and 138 cm from the beam, lies the Central Outer Tracker [30]. It is a new open-cell drift chamber, able to reconstruct tracks in the $|\eta| < 1$ region. The COT replaces an older drift chamber, the CTC [31], that would have been unable to cope with the expected occupancy and event rate of Run II.

Each of the eight superlayers of cells consists of twelve layers of sense wires, alternating with field-shaping wires. Axial superlayers alternate with stereo superlayers, thus providing 48 axial and 48 stereo measurements for each track.

In the COT, the cell size is roughly four times smaller than in the CTC. Usage of a faster gas (Ar – Ethane – CF₄ instead of Ar – Ethane) reduces the maximum drift time by a further factor of two, down to 100 ns. This makes the COT immune from event pile-up, even at the highest collision rate of 1/(132 ns).

2.3.3 Time of flight

A recent addition to CDF II, the time-of-flight detector is an array of scintillator bars, placed at the outer edge of the COT, at a radial coordinate of 140 cm. An accurate measurement of a particle's time of flight in the CDF tracking volume can be used quite effectively in particle identification.

Scintillator bars are about three meters long, matching the COT active volume; their thickness (4 cm) is limited by the space which remained available between the previously designed COT and magnet. Their width was determined by occupancy³ and resolution considerations; the best choice turned out to be also of the order of 4 cm. The bars have a trapezoidal cross

³Detector occupancy depends on the average number of superimposed interactions, which increases with luminosity. TOF occupancy is estimated to be 0.1 with 2 superimposed events, and 0.4 with 10 events.

section, in order to minimize cracks in the geometry; the scintillating material is Bicron 408, which has a short rise time and a long (380 cm) attenuation length.

Photomultiplier tubes, attached to both ends of each bar, provide time and pulse height measurements. By comparing the two pairs of results, the detector determines the instant in which a particle crossed the scintillator with an accuracy of about 100 ps, and the z coordinate of the intersection. The latter measurement is compared to the results of 3D track reconstruction in the inner tracking volume, to associate a time of flight to each track.

2.3.4 Magnet

The CDF tracking systems are enclosed in a superconducting solenoid, which provides a uniform magnetic field of up to 1.5 T along the detector axis, over a cylindrical fiducial volume 3.5 m long and 2.8 m in diameter.

The solenoid is built of an Al-stabilized NbTi superconductor, able to withstand currents up to 5000 A, and operating at liquid helium temperature. During most of Run I, the magnet operated at 4650 A, corresponding to a current density of 1115 A/m and a central field of 1.41 T.

Although the design lifetime of the solenoid was only ten years, it is possible to reuse the magnet during Run II. The cool-down procedures that were used during Run I limited mechanical stress to the coil, avoiding fatigue damage.

2.4 Calorimetry

2.4.1 Overview

CDF uses scintillator sampling calorimeters, divided into separate electromagnetic and hadronic sections, and providing coverage for $|\eta| \leq 3.64$. The calorimeter was an essential tool in selection and reconstruction of events in Run I; in Run II it continues to measure the energy of photons, electrons, jets, and the missing transverse energy⁴ associated to neutrinos and possibly to neutral exotic particles.

Calorimeter calibration can be performed by matching the tracks found in the tracking system to the corresponding calorimetry towers; during Run I, this provided a 2.5% accuracy on jet energy measurements.

The entire calorimeter is segmented into projective towers, whose geometry is summarized in Table 2.3. Each tower consists of alternating layers of passive material (lead for the e.m. section, iron for the hadronic compartment) and scintillator tiles. The signal is read via wavelength shifters (WLS) embedded in the scintillator; light from the WLS is then carried to photomultiplier tubes. Table 2.4 shows the most important characteristics of each calorimeter sector. The central and end-wall calorimeters ($|\eta| < 1.1$) [32] [33] were recycled from Run I; the plug

⁴Contrarily to e^+e^- colliders, in $p\bar{p}$ colliders the longitudinal momentum of the initial state is unknown.

$ \eta $ range	$\Delta\phi$	$\Delta\eta$
0 — 1.1 (1.2 had)	15°	0.1
1.1 (1.2 had) — 1.8	7.5°	0.1
1.8 — 2.1	7.5°	0.16
2.1 — 3.64	15°	0.2 — 0.6

Table 2.3: Calorimeter segmentation. “had” means Hadoron Calorimeter.

ones ($1.1 < |\eta| < 3.64$) were built anew, to replace an older gas calorimeter that would not be able to function at the increased event rate of Run II.

	Central and End-wall	Plug
Electromagnetic:		
Thickness	19 X_0 , 1 λ	21 X_0 , 1 λ
– per sample (Pb)	0.6 X_0	0.8 X_0
– per sample (scint.)	5 mm	4.5 mm
Light yield	160 p.e./GeV	300 p.e./GeV
Sampling resolution	11.6% / \sqrt{E}	14% / \sqrt{E}
Stochastic resolution	14% / \sqrt{E}	16% / \sqrt{E}
Hadronic:		
Thickness	4.5 λ	7 λ
– per sample (Fe)	1 in (central) 2 in (end-wall)	2 in
– per sample (scint.)	6 mm	6 mm
Light yield	40 p.e./GeV	39 p.e./GeV
Resolution	75%/ $\sqrt{E} \oplus 3\%$	80%/ $\sqrt{E} \oplus 5\%$

Table 2.4: Characteristics of the CDF II calorimeter. X_0 means one radiation length.

2.4.2 Central Calorimeter

Apart from the electronics, the central calorimeter in CDF Run II is the same as used during Run I. The energy measurement response time is already fast enough to accommodate a 132 ns bunch spacing.

Central Electromagnetic Calorimeter

The central electromagnetic calorimeter consists of projective towers of alternating lead and scintillator. The signal is read via a PMMA⁵ wavelength shifter, and carried via clear fiber to photomultiplier tubes. None of these is expected to suffer much from radiation damage. The light yield loss is expected to be around 1% per year; 60% of this loss is explained by the gradual shortening of the attenuation length in the scintillator.

A two-dimensional wire chamber is embedded in the calorimeter, as a shower maximum detector (CES). Its usage in the Run I trigger decreased the fake electron trigger rate by a factor of two [34].

Another wire chamber is placed immediately in front of the calorimeter, to act as a preshower detector (CPR) which uses the tracker and the solenoid coil as radiators. The CPR has proven to be extremely useful in rejection of electron background; it also reduced systematic uncertainties for direct photon measurements by a factor of three [35].

Central Hadronic Calorimeter

The central and end-wall hadronic calorimeters use 23 iron layers as radiator. The scintillator should not suffer radiation damage from measured events.

The hadronic compartment geometry matches the projective towers of the electromagnetic calorimeter.

2.4.3 Plug Calorimeter Upgrade

The CDF II plug calorimeter, shown in Fig. 2.2, covers the η region between 1.1 and 3.64, corresponding to polar angles between 37° and 3° . It replaces an older gas calorimeter, whose response speed was too slow for usage at the CDF II 132 ns inter-bunch. Being based on the same principles as the central calorimeter, the new plug calorimeter also makes experimental data more homogeneous.

The calorimeter is divided in 12 concentric η regions, which are further segmented in 24 (for $|\eta| < 2.11$) or 12 (for $|\eta| > 2.11$) projective towers.

Plug Electromagnetic Calorimeter

The EM section of the plug calorimeter consists of 23 absorber-scintillator layers. A calcium-tin-lead alloy, enclosed between steel plates, is used as absorber.

The first layer of the EM section is used as a preshower detector. In order to distinguish γ from π^0 reliably, the light yield needs to be higher than on other layers. Therefore, the first scintillator layer is thicker (10 mm instead of 6 mm) and made of a brighter material; it

⁵PMMA = polymethylmethacrylate

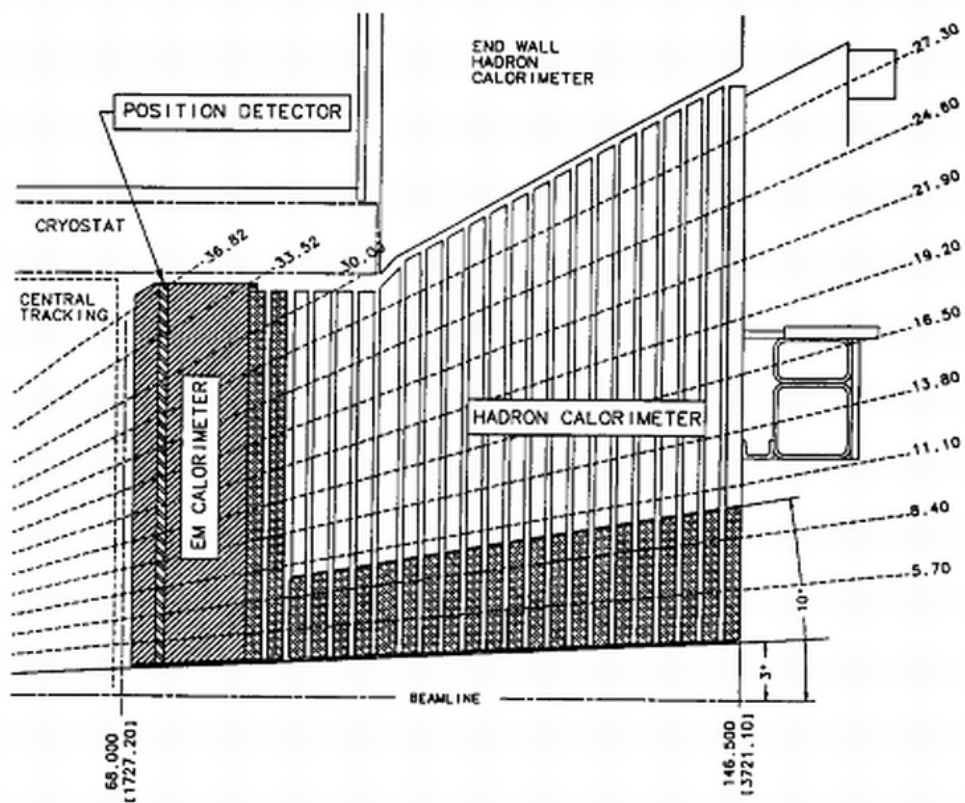


Figure 2.2: Cross section of half CDF II plug calorimeter

is read out separately from the rest of the calorimeter, via multi-anode photomultiplier tubes (MAPMT).

As in the central calorimeter, a shower maximum detector (PES) is also embedded in the plug EM calorimeter, at a depth of about six radiation lengths. The PES consists of eight 45° sectors, each covering six (or three) calorimetric towers in ϕ ; each sector is further segmented in two η regions, in order to reduce occupancy. Within each region, scintillating strips are arranged on two layers, in directions parallel to either edge of the sector; this provides a two-dimensional measurement of the shower. The strips are 5 mm wide and 6 mm thick; they are read out via WLS fibers and MAPMT.

The PES is used to measure the position of electromagnetic showers with an accuracy reaching 1 mm for high-energy electrons, and to discriminate pions from photons and electrons.

Plug Hadronic Calorimeter

The hadron plug calorimeter was designed to optimize detector performance on b , electroweak and jet physics, and to help in muon detection by analyzing their rate of energy loss. It achieves an energy resolution of about $80\%/\sqrt{E} \oplus 5\%$, which is dominated by the sampling fluctuations from the steel absorber plates. The most strict requirement is that the light yield within each tile should be uniform to 4% or better; dis-uniformity between different tiles is not as important, as the hadron shower usually affects ten or more layers.

2.5 Muon Chambers

The outermost component of CDF II is a set of scintillators, drift tubes and steel absorbers, used for the detection of muons.

During Run I, detection of muons has proven to be an important requirement, both for the analysis of several physics channels and for calibration. For example, a clean sample of W bosons is obtained by reconstructing their muon decay mode; $J/\psi \rightarrow \mu^+ \mu^-$ decays are an important part of the heavy quark physics program, as well as a tool to measure systematic effects in the detector.

The tracking improvements from Run I to Run II have a deep impact on muon detection. Before the upgrades, muons in the central region were identified by their penetrating power, and their momentum was measured in the central tracking chamber. On the contrary, the momentum of forward muons had to be measured in the muon chambers themselves, by resorting to a toroidal magnet, as the central tracker only covered the $|\eta| < 1$ region.

With the SVX II upgrade, this distinction falls: measurement of muon momentum can be performed in the central tracker, where the multiple scattering effects are smaller, and the toroidal magnets are not required any longer. Central tracks are measured in the drift chamber; forward tracks ($|\eta| > 1$) are tracked in the silicon only.

Run I central muon chambers (**CMU**) are reused without major changes; some upgrades which started under Run I (**CMP** and **CSP**, the Central Muon/Scintillator Upgrades; **CMX** and **CSX**, the Central Muon/Scintillator Extension) are completed; and a new set of chambers, the Intermediate Muon Detector **IMU**, replaces the previous Forward Muon Detectors (**FMU**)[36].

	CMU	CMP/CSP	CMX/CSX	IMU
η coverage	0 — 0.6	0 — 0.6	0.6 — 1.0	1.0 — 1.5
Drift tubes:				
thickness	2.68 cm	2.5 cm	2.5 cm	2.5 cm
width	6.35 cm	15 cm	15 cm	8.4 cm
length	226 cm	640 cm	180 cm	363 cm
max drift time	0.8 μ s	1.4 μ s	1.4 μ s	0.8 μ s
# tubes (Run Ib)	2304	864	1536	—
# tubes (Run II)	2304	1076	2208	1728
Scintillators:				
thickness	N/A	2.5 cm	1.5 cm	2.5 cm
width	N/A	30 cm	30 - 40 cm	17 cm
length	N/A	320 cm	180 cm	180 cm
# counters (Run Ib)	N/A	128	256	—
# counters (Run II)	N/A	269	324	864
π^0 int. lengths	5.5	7.8	6.2	6.2 — 20
Min P_t (GeV/c)	1.4	2.2	1.4	1.4 — 2.0
MS resol. (cm GeV)	12	15	13	13 — 25

Table 2.5: Parameters of muon detection at CDF. Pion interaction length and the limit on resolution due to multiple scattering are computed at $\theta = 90^\circ$ in the central detectors CMU, CMP and CSP; at $\theta = 55^\circ$ in CMX and CSX; and on the entire θ coverage for the IMU.

Due to their size, muon systems are unable to take data within the Run II inter-bunch interval of 400 or 132 ns; this is not a problem, since the low occupancy of the muon chambers allows integration over multiple events. Scintillators are used to associate muon stubs to the appropriate event.

Table 2.5 summarizes the information on the muon subsystems; the following sections will describe their characteristics in deeper detail.

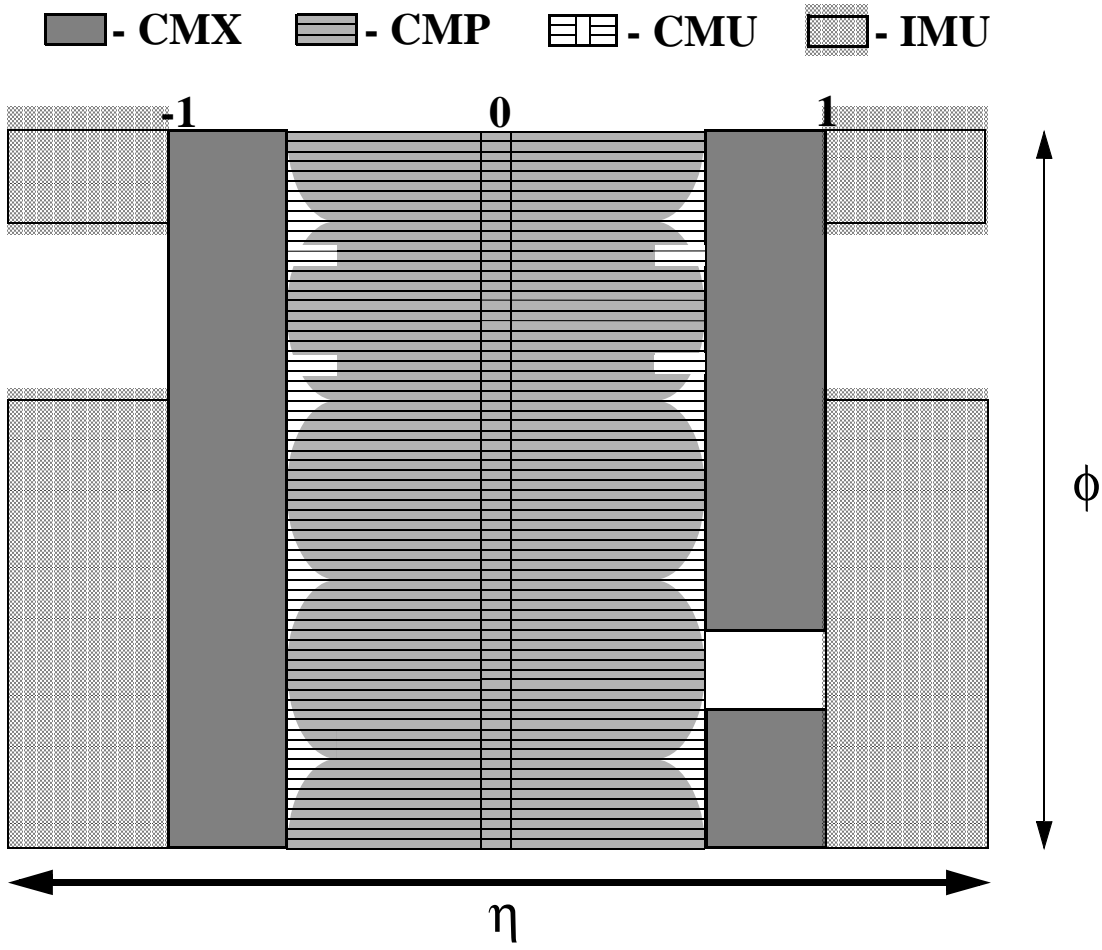


Figure 2.3: η and ϕ coverage of the Run II muon systems

2.5.1 Central Muon Detectors

The first muon system built at CDF, the **Central Muon Detector** (CMU) [37], is a set of 144 modules, each containing four layers of four rectangular cells. It is placed just outside the central hadronic calorimeter, whose 5.5 interaction lengths absorb more than 99% of the outgoing charged hadrons.

A second set of muon chambers, the **Central Muon Upgrade** (CMP) [38], forms a square box around the CMU, and is shielded by an additional layer of 60 cm of steel. Due to the detector geometry, the η coverage varies with azimuth as shown in fig. 2.3. The CMP consists of four layers of single-wire drift tubes, staggered by half cell per layer, and operated in proportional mode. On the outer surface of the CMP lies the **Central Scintillator Upgrade** (CSP), a layer of rectangular scintillator tiles.

Another upgrade which had begun in Run I is the **Central Muon Extension** (CMX) with the associated **Central Scintillator Extension** (CSX). It is a conical array of drift tubes, with scintillators on both sides; it extends the CMU/CMP θ coverage from 55° to 42° , except in a 30° ϕ gap which is used by the solenoid cryogenic system.

2.5.2 Intermediate Muon Detectors

Detection of muons in the forward region is accomplished by the **Intermediate Muon Detectors** (IMU). This detector recycles the older Forward Muon toroidal magnets, which is moved closer to the interaction point (just outside the plug calorimeter PMT arrays). The steel toroids, together with a new pair of steel rings, act as shielding for a new array of drift tubes and scintillator counters, placed on the outer radius of the toroids.

Like the CMX/CSX, the IMU has four staggered layers of drift tubes, and two layers of scintillator. Contrarily to the CSX, one of the scintillator layers is separated from the drift tubes by a thick layer of steel; this geometry strongly suppresses fake triggers due to hadrons.

2.6 Data Acquisition and Trigger

Due to the increase in collision frequency, the DAQ (Data Acquisition) and trigger systems of CDF had to be almost completely replaced. The new three-level architecture, schematized in Fig. 2.4, is fully capable of withstanding a 132 ns bunch separation, while keeping dead time as short as possible.

2.6.1 Level 1 trigger

The front-end electronics of all detectors is fitted with a synchronous pipeline, 42 events deep, where the entire data regarding each event is stored for 5544 ns. Meanwhile, part of the data is examined in a first layer of dedicated, synchronous, highly parallel hardware processors:

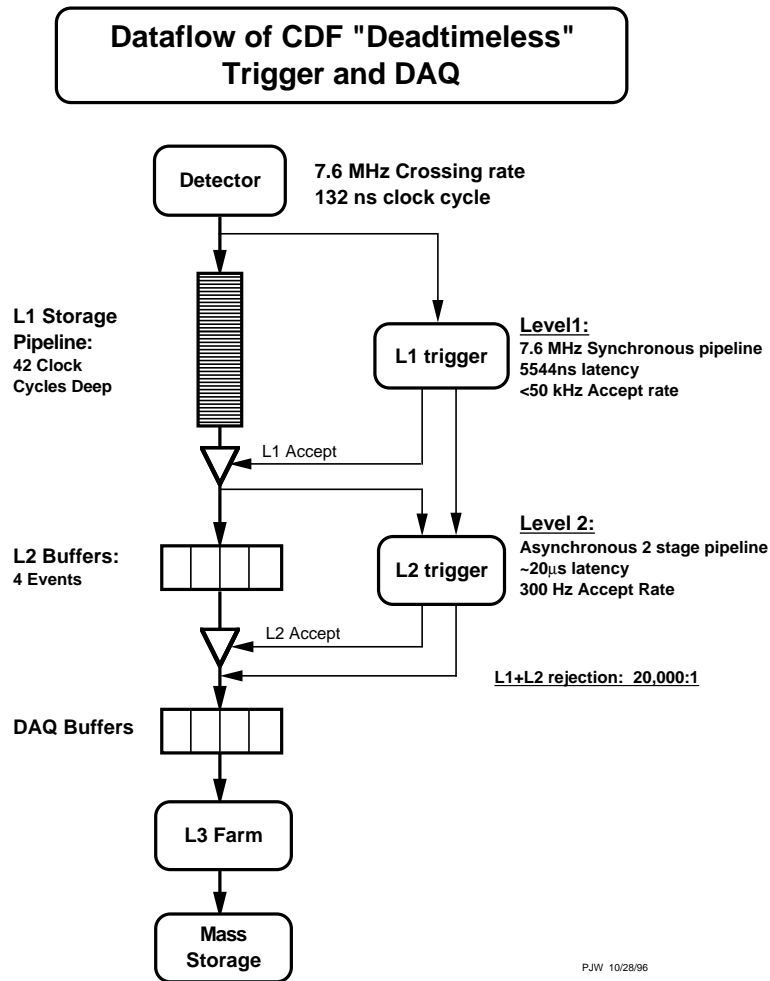


Figure 2.4: Block diagram of the CDF II Trigger

- **XFT**, the extremely Fast Tracker, which reconstructs tracks on the transverse plane of the COT (Central Outer Tracker) to propagate these tracks to the calorimeters and muon chambers;
- the Calorimeter Trigger, which detects electron and photon candidates, jets, total transverse energy, and missing transverse energy;
- the Muon Trigger, which matches XTRP tracks to stubs in the muon chambers.

“Objects” from the level one trigger subsystems are combined in a flexible decision module, which takes a decision by requiring the presence of a certain number of features in the event: for example, two muon candidates with P_t above 3 GeV. Up to 64 different sets of requirements can be checked at the same time; each of these triggers can be pre-scaled independently of the others.

The level 1 trigger takes a decision within 4 μ s, while the event’s data is still in the pipeline. This makes the first trigger level truly dead-timeless. The rejection factor is about 150 and the event rate is about 50 kHz.

2.6.2 Level 2 trigger

Events matching the requirements of level 1 are downloaded into one of four asynchronous event buffers, and further analyzed by a second set of hardware processors. Trigger level 2 is asynchronous: events remain in the buffer until they are accepted or rejected. This can cause dead time, when all four buffers are full. In order to keep dead time at 10%, with a level 1 rate of 50 kHz, level 2 has been split in two pipelined steps of 10 μ s each.

- Jets usually affect more than a single calorimetric tower. Calorimeter clustering (**L2CAL**) sums the energies collected by single towers and provides a measurement of the total jet energy.
- The calorimeter shower maximum (**XCES**) is used to reduce the rate of fake electrons and photons. It also makes it easier to match XFT tracks to their calorimetric clusters.
- The Silicon Vertex Tracker (**SVT**) reconstructs tracks in the vertex detector, measuring their impact parameter d . Triggering on d proves extremely helpful in b -quark physics.
- Data is also collected from the level 1 track and muon triggers.

During the second pipelined step, the results of the first phase are fed to a set of Alpha processors; each processor examines the event for a different set of characteristics.

The level 2 accept rate is around 300 Hz, with a rejection of about 150.

2.6.3 Level 3 trigger

After being accepted by the level 2 trigger, the entire event data is read out and loaded into a Linux PC farm, where the event is fully reconstructed in software. The level 3 reconstruction program is almost fully written in C++, using object-oriented techniques.

After an event is reconstructed, it is sent to an event counter, where its characteristics are histogrammed; if the event passes the level 3 cuts, it is also permanently stored to tape.

Assuming a level 3 input rate of 300 Hz, a level 3 rejection of 10, and an average event size of 250 kB.

2.6.4 Online Monitoring

The CDF detector consists of many detector subsystems and runs in a high rate large bandwidth data transfer environment. To take data with high efficiency and high quality, it is necessary to quickly spot problems with one of these sub-detectors in real time. Multiple event monitor programs are attached to the DAQ system [39][40][41]. The online monitoring programs are called Consumers, where a consumer is defined as a process which receives events from Consumer Server Logger (CSL) in real time. CSL sends the data to the computer center where they are written to tape and forwards copies of a subset of the data to the online monitoring programs. Figure 2.5 shows a schematic view of the CDF online monitoring system (Consumer Framework). The task of Consumers is to analyze and monitor the event data and to make histograms and tables. These results could be viewed by the display browser via a server in real time. Results of the monitor are also stored as data files periodically during a run, and also archived systematically. The display browser provides a GUI (Graphical User Interface) to view the online monitored results, while also providing some basic utilities to do comparisons with previously stored results. By separating the two tasks of monitoring and displaying, we remove CPU bound associated with displaying graphics from the machine which runs the consumers. During the data taking, multiple consumer processes run in parallel, receiving event data with the desired trigger types from the CSL. Communication between a consumer and run control which control overall CDF DAQ system is handled by the Error Receiver. Severe errors detected by a consumer monitor program are forwarded to run control to take necessary actions. The state manager watches the state of consumers.

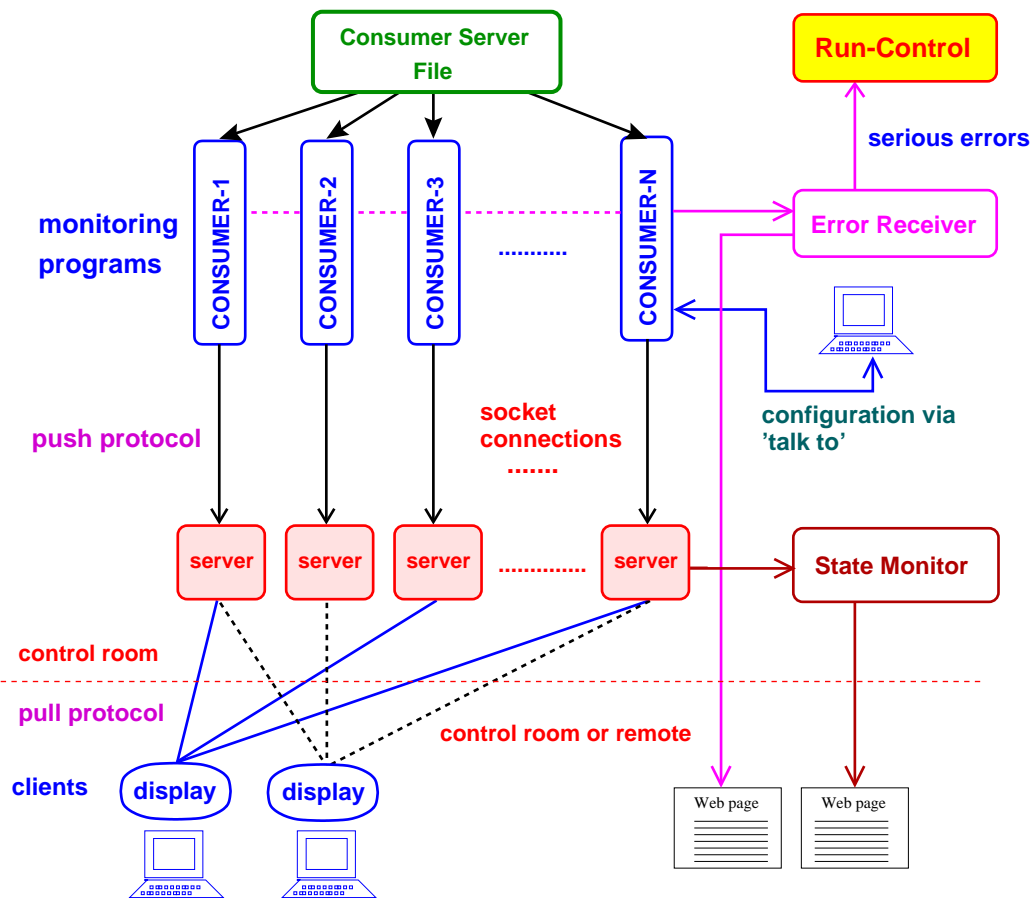


Figure 2.5: Design of the CDF online consumer framework.

Chapter 3

Event selection

To extract dilepton $t\bar{t}$ candidate events in Run II data, we apply the standard kinematical cuts defined by the CDF collaboration. These kinematical cuts reduce events from several non- $t\bar{t}$ processes that have similar signatures and remain in the candidate events. In this chapter we summarize the necessary particle identifications and thus discuss dilepton kinematical event selection to be required for our main analysis.

3.1 Particle Identification

The Standard Model (SM) top quark decays into a W boson and a b quark, immediately and essentially 100% of the time. The $t\bar{t}$ event signature is therefore classified by the decay products of the two W 's, each of which can produce two quarks or two leptons. The signatures of the $t\bar{t}$ dilepton channel are (a) two charged leptons, (b) two jets from b quarks and (c) large missing energy from two neutrinos. In this section, we discuss the particle identifications for the reconstruction of top quark events; i.e. electrons, muons, quark jets and the missing energy.

3.1.1 Electron Identification

When high energy electrons enter the electromagnetic calorimeter, they interact with the electromagnetic (EM) field around atomic nuclei and create e^+e^- pairs or photons. These secondary EM particles are also very energetic and thus each can produce e^+e^- pair, Compton electrons, and photons. The first step to identify electrons is to find electron showeres in the EM calorimeter (electron showeres are largely complete before the Had calorimeters). This is done by identifying clusters (in $\eta - \phi$ plane) of the electromagnetic energy. An EM cluster is defined by a seed tower (any tower that has more than 3 GeV of transverse energy) and shoulder towers (the towers nearby the seed tower which have at least 0.1 GeV of the transverse energy).

As a next step to identify electrons is to define the specific variables to determine electrons in

terms of measurable quantities at CDF detector. The variables of central electrons are defined and required as follows:

- E_T :
The transverse electromagnetic energy deposited by the electron in the CEM is calculated as the electromagnetic cluster energy multiplied by $\sin\theta$, where θ is the polar angle provided by the best COT track pointing to the EM cluster.
- P_T :
The transverse momentum of the COT beam constrained track as measured using the track curvature in the COT in the magnetic field.
- Isolation :
The energy in a cone of radius $\Delta R = \sqrt{\Delta\eta^2 + \Delta\phi^2} \leq 0.4$ around the electron cluster excluding the electron cluster divided by the energy in the electron cluster.
- E_{had}/E_{em} :
The ratio of the hadronic calorimeter energy to the electromagnetic calorimeter energy for a cluster.
- E/P :
The ratio of the EM cluster transverse energy to the COT track transverse momentum.
- L_{shr} :
The lateral shower profile for electrons. This variable compares the energy in CEM towers adjacent to the seed tower for data and test beam electrons.
- $Q^*\Delta x$:
The distance in the $r - \phi$ plane between the extrapolated, beam constrained, COT track and the best matching CES cluster, times the charge of the track.
- Δz :
The distance in the $r - z$ plane between the extrapolated, beam constrained, COT track and the best matching CES cluster.

- χ_{strip}^2 :
The χ^2 comparison of the CES shower profile in the $r - z$ view with the same profile extracted from test beam electrons.
- z_0 :
The z intersection of the track with the beam axis in the $r - z$ plane.
- Track quality cuts :
The electron associated track must have passed through 3 axial and 2 stereo superlayers (SL), with at least 5 hits out of 12 in each SL.

Furthermore, the specific variables of plug electrons are defined and required as follows:

- PEM3 \times 3FitTower :
The numbers of towers used by the 3 towers in $\eta \times 3$ towers in ϕ PEM cluster fit.
- PEM3 \times 3Fit χ^2 :
A χ^2 obtained by comparing observed lateral shower shape with the predicted shape from test beam electrons.
- PES5by9u :
A simple ratio (Sum of the energies of the central 5 u-strips of a PES cluster)/(Sum of the energies of all 9 u-strips of a PES cluster)
- PES5by9v :
A simple ratio (Sum of the energies of the central 5 v-strips of a PES cluster)/(Sum of the energies of all 9 v-strips of a PES cluster)
- Fiducial volume :
The determination of fiducial region in the plug calorimeter is made in the PES detector η .
- ΔR :
The matching distance between the PEM3 \times 3Fit coordinates and the PES coordinates of

a given PES cluster.

Thus, the requirements on the central and plug electrons are shown in Table 3.1, 3.2 respectively.

Variable	Central Electron
Region	Central
E_T	≥ 20 GeV
P_T	≥ 10 GeV
z_0	≤ 60 cm
Conversion	Veto
E_{had}/E_{em}	$\leq (0.055 + (0.00045 \times E))$
Isolation	≤ 0.1
L_{shr}	≤ 0.2
E/P	≤ 2.0 unless $P_T \geq 50$ GeV/c
Δz	≤ 3 cm
Δx	$-3.0 \leq q \times \Delta X \leq 1.5$
χ^2	≤ 10.0

Table 3.1: Central Electron selection cuts baseline.

Variable	Plug Electron
η	$1.2 \leq 2.0$
E_T	≥ 20 GeV
E_{had}/E_{em}	≤ 0.055
PEM3 \times 3FitTow	$\neq 0$
PEM3 \times 3 χ^2	≤ 10
Pes5by9U	≥ 0.65
Pes5by9V	≥ 0.65
Isolation	≤ 0.1
Δz	≤ 3 cm

Table 3.2: Plug Electron selection cuts baseline.

3.1.2 Muon Identification

Muons being heavy copies of electrons penetrate matter very easily. They are able to pass through the EM and Hadron calorimeters and leave tracks in the muon drift chambers CMU (Central MUon Detector), CMP (Central Muon UPgrade) and CMX (Central Muon EXtention). The location of the muon in the chamber is determined by the drift chamber time-distance relation the ϕ direction and by charge division in the z direction. An object considered as a muon must have aligned hits in both $r - \phi$ and $r - z$ planes on at least 3 separate layers. These hits form a so called “muon stub” which is then matched to the COT tracks extrapolated to the muon chambers.

The following variables are used to define muons in terms of measurable quantities at the CDF detector.

- P_T :
The transverse momentum of the COT beam constrained track as measured using the COT track curvature in the magnetic field.
- E_{HAD}, E_{EM} :
The energies that muon candidate deposits in the hadronic, electro-magnetic part of calorimeter respectively .
- $|\Delta x|$:
The distance in the $r - \phi$ plane between the extrapolated track and the muon stub at the chamber radius.
- d_0 :
The muon track impact parameter. If the track has silicon hits or not, the cuts are looser, or tighter.
- Track quality cuts :
The electron associated track must have passed through 3 axial and 2 stereo superlayers (SL), with at least 5 hits out of 12 in each SL.

Thus, the requirements on the muons are shown in Table 3.3.

3.1.3 Jet Reconstruction

The jet finding algorithm at CDF is based on the tower nature of the calorimeters. At CDF, the *fixed cone* algorithm is applied to reconstruct jet quantities.

The jet clustering algorithm groups calorimeter towers with $E_{Ti} > 1$ GeV into jets. $E_{Ti} = E_i \sin \theta_i$ is the transverse energy of a tower with respect to the z -position of the primary vertex of

Variable	Muon
P_T	≥ 20 GeV
z_0	≤ 60 cm
Cosmic	Veto
Isolation	≤ 0.1
E_{had}	$\leq 6 + \max(0, 0.028 \times (P - 100)) GeV$
E_{em}	$\leq 2 + \max(0, 0.0115 \times (P - 100)) GeV$
$ d_0 $	≤ 0.02 cm (if track has Silicon hits) OR ≤ 0.2 cm (if not)
$ \Delta x_{CMU} $	≤ 3.0 cm
$ \Delta x_{CMP} $	≤ 5.0 cm
$ \Delta x_{CMX} $	≤ 6.0 cm

Table 3.3: Muon selection cuts baseline.

the $p\bar{p}$ interaction, and the energy E_i is the sum of the energies measured in the electromagnetic and hadronic compartments of that tower.

In the jet reconstruction, “seed towers” are first defined in the decreasing order of E_{Ti} . For each seed tower the towers within a radius of R with respect to its position are used to build “clusters”. Once we have an initial list of clusters, the cluster transverse energy and the location of the cluster is calculated using the definitions:

$$E_T^{jet} = \sum_{i=0}^{N_{tow}} E_{Ti} \quad (3.1)$$

$$\phi^{jet} = \sum_{i=0}^{N_{tow}} \frac{E_{Ti}\phi_i}{E_T^{jet}} \quad (3.2)$$

$$\eta^{jet} = \sum_{i=0}^{N_{tow}} \frac{E_{Ti}\eta_i}{E_T^{jet}} \quad (3.3)$$

where N_{tow} is the number of towers inside the radius R with $E_T > 1$ GeV.

This procedure is repeated iteratively and a new list of towers around the new center is determined. The jet E_T and direction are recalculated until the list of towers assigned to the clusters is stable, that is, when the geometrical center of the tower corresponds to the cluster centroid. Overlapping jets are merged if they overlap by more than 50%. If the overlap is smaller than 50%, each tower in the overlap region is assigned to the nearest jet.

The final energy and momentum of a jet are computed from the final list of towers:

$$E_{jet} = \sum_{i=0}^{N_{tow}} E_i, \quad (3.4)$$

$$p_x^{jet} = \sum_{i=0}^{N_{tow}} E_i \sin(\theta_i) \cos(\phi_i), \quad (3.5)$$

$$p_y^{jet} = \sum_{i=0}^{N_{tow}} E_i \sin(\theta_i) \sin(\phi_i), \quad (3.6)$$

$$p_z^{jet} = \sum_{i=0}^{N_{tow}} E_i \cos(\theta_i) \quad (3.7)$$

$$p_T^{jet} = \sqrt{(p_x^{jet})^2 + (p_y^{jet})^2} \quad (3.8)$$

$$\phi_{jet} = \tan \frac{p_y^{jet}}{p_x^{jet}} \quad (3.9)$$

$$\sin \theta_{jet} = \frac{p_T^{jet}}{\sqrt{(p_x^{jet})^2 + (p_y^{jet})^2 + (p_z^{jet})^2}} \quad (3.10)$$

$$E_{T,jet} = E_{jet} \sin \theta_{jet} \quad (3.11)$$

In general, jets with $E_T < 3$ GeV are not used in physics analysis at CDF.

However, the jet energy defined with the jet clustering algorithm is not the energy of the original parton which we would like to know. By comparing parton level and observed energies in the Monte Carlo events, we know that the measured E of the jet is different from the energy of the parent quark or gluon. Whereby we need to rely on the jet energy correction at CDF which is based on QCD jets. The precision to which this can be achieved determines the precisions of jet-associated measurements, e.g. a 1% uncertainty on the energy scale of jets results in an uncertainty of 10 % on the cross section for jet production at transverse momentum of 500 GeV/c [42] and a 1 GeV/c² uncertainty on the top quark mass [43].

We review the CDF jet energy correction below. The original parton transverse energy can be estimated by correcting the jet for instrumental effects and for radiation and fragmentation effects:

$$p_T^{parton} = (p_T^{jet} \times C_\eta - C_{MI}) \times C_{Abs} - C_{UE} + C_{OOC} = p_T^{particle} - C_{UE} + C_{OOC}, \quad (3.12)$$

where p_T^{parton} is the transverse momentum of the parent parton the procedure is aimed at, p_T^{jet} is the transverse momentum measured in the calorimeter jet, $p_T^{particle}$ is the transverse momentum of the particle jet, that is, a jet corrected by all instrumental effects which corresponds to the sum of the momenta of the hadrons, leptons, and photons within the jet cone, and

- C_η , “ η -dependent” correction, ensures homogeneous response over the entire angular range;
- C_{MI} , “Multiple Interaction” correction, is the energy to subtract from the jet due to pile-up of multiple $p\bar{p}$ interactions in the same bunch crossing;
- C_{Abs} , “Absolute” correction, is the correction of the calorimeter response to the momentum of the particle jet. Particle jets can be compared directly to data from other experiments or theoretical predictions which include parton radiation and hadronization.
- C_{UE} and C_{OOC} , the “Underlying Event” and “Out-Of-Cone” corrections, correct for parton radiation and hadronization effects due to the finite size of the jet cone algorithm that is used. Note that these corrections are independent of the experimental setup, i.e. the CDF detector environment.

All the correction factors are determined as functions of the jet transverse momentum but they apply to all components of the four-momentum of the jet.

The C_{Abs} correction is derived using a detailed Monte Carlo (MC) simulation of the physics processes and the detector response. The corrections C_{UE} and C_{OOC} are determined using the PYTHIA MC generator. Thus the major task is the tuning and validation of the detector simulation as well as of the physics modeling used in the simulation. The other corrections are mostly derived directly from data but are also compared to the simulation.

The correction factors to jets described above is called “CDF generic correction”. On the contrary, reconstructing top quark by correcting b jet energy is called “top specific correction”. In our analysis, we employ the generic correction to describe CDF detector responses (C_η, C_{MI}, C_{Abs}), and adopt the top specific correction to take into account hadronization effect specific to the top quark decay. The uncertainty of the jet energy scale remains after these corrections, and constitutes the main systematic uncertainty in the top mass measurement. Therefore, the precise calibration of the jet energy scale would be required in the future measurement.

3.1.4 Missing Transverse Energy Reconstruction

The experimental signature of neutrinos is the missing transverse energy \cancel{E}_T , i.e. the imbalance of the energy flow in the plane perpendicular to the beam axis.

In the CDF detector, the z -coordinate is defined along the proton beam direction, and x and y axes in the horizontal and the vertical directions, respectively. The x - and the y -components of the missing energy are defined by:

$$\cancel{E}_x \equiv - \sum_{i=1}^{N_{towers}} E_x^i, \quad (3.13)$$

$$\cancel{E}_y \equiv - \sum_{i=1}^{N_{towers}} E_y^i, \quad (3.14)$$

where the sum runs over all calorimeter towers above threshold, where the tower energy threshold depends on the region of the detector where the tower is located. Having defined \cancel{E}_x and \cancel{E}_y we can define the transverse missing energy variable \cancel{E}_T and its azimuthal angle $\phi_{\cancel{E}_T}$ by

$$\cancel{E}_T \equiv \sqrt{\cancel{E}_x^2 + \cancel{E}_y^2}, \quad (3.15)$$

$$\phi_{\cancel{E}_T} \equiv \arctan \frac{\cancel{E}_y}{\cancel{E}_x}. \quad (3.16)$$

The missing transverse energy discussed in this section is called the “raw” missing transverse energy. The raw missing transverse energy, however, does not precisely correspond to the total transverse momenta of neutrinos. In application for the top quark mass measurement, we need additional correction factor for MET and cancellation of the jet correction effect.

3.2 Event selection

The $t\bar{t}$ dilepton events are characterized with two high P_T charged leptons, missing transverse energy from the undetected neutrinos, and two jets from the hadronization of the b quarks. Additional jets are often produced by initial state and final state radiation. A trigger system first identifies candidate events by finding either a central electron or muon candidate with $E_T \geq 18$ GeV, or an end plug electron candidate with $E_T \geq 20$ GeV in an event with $\cancel{E}_T \geq 15$ GeV. After full event reconstruction, the candidate event sample is further refined by selection criteria, which are *a priori* determined to minimize the expected statistical and systematic uncertainties of the cross section measurement. Our top quark mass measurement is based on this cross section measurement study. Namely, we use the estimated numbers of signal and background events for our top mass measurement, as we further describe in section 4 of Top Quark Mass measurement.

3.2.1 Selection criterion

This event selection requires two oppositely charged leptons with $E_T \geq 20$ GeV. One lepton, the “tight” lepton as described in previous sub-sections 3.1.1, 3.1.2, must pass strict lepton identification requirements and be isolated. A lepton is isolated if the total E_T within a cone $\Delta R \equiv \sqrt{\Delta\eta^2 + \Delta\phi^2} \leq 0.4$, minus the lepton E_T , is ≤ 10 % of the lepton E_T . Tight electrons have a well measured track pointing at an energy deposition in the calorimeter. Tight muons must have a well measured track linked to hits in the muon chambers and energy deposition in the calorimeters consistent with that expected for muons.

The other lepton, the “loose” lepton, is selected to remove or relax some criteria. One is to remove lepton isolation requirement, another is to relax muon fiduciality coming from CDF detector or signal on CDF muon detector. The first step in the event selection is to require two kinds of leptons. After we determine tight - tight or tight - loose lepton pair, the top dilepton event selection is implemented according to the following prescription.

1. Calculate the invariant mass of the lepton pair. If it is inside Z mass window ($76 < M_{ee,\mu\mu} < 106$), require additionally $jetsig^1 > 8$ and $\Delta\phi > 10^\circ$ (\cancel{E}_T , nearest jet).
2. Loop over jets in the event and apply L5 jet energy correction, and require $E_T \geq 15$ GeV, $|\eta_{jet}| < 2.5$
3. Re-calculate the magnitude and phi angle of \cancel{E}_T , and require $\cancel{E}_T > 25$ GeV. If $\cancel{E}_T < 50$ GeV, additionally require $\Delta\phi > 20^\circ$ (\cancel{E}_T , nearest lepton or jet).
4. Require $H_T^2 > 200$ GeV. In case of this, all of quantities, i.e. the energy of jets and \cancel{E}_T should be corrected.
5. Require oppositely charged leptons.
6. Veto conversions and cosmic rays.

In the current CDF dilepton study, there are 2 types of the event selection and the cross section measurement, which are called “DIL” and “LTRK” analysis, respectively. In principle, “LTRK” selection is looser than “DIL” selection, but DIL is not a subset of LTRK. In this section, we simply review “DIL” selection which our top quark mass measurement employs. When we adopt DIL selection, at the end, we obtain the expected background numbers and significant top signal events. Table 3.4 shows the background composition, the expected numbers and the number of dilepton candidate events. These numbers play significant roles in the following sections, so we look back on the numbers again.

¹jetsig means one of the parameter for dilepton event selection. jetsig is defined by $\frac{E_T}{\sum_{|\Delta\phi(\cancel{E}_T, jet)| < 90^\circ} (E_T^{jet} \frac{E_T}{E_T})}$

²This is the sum E_T of the observable objects.

Source	# of after all event selection
WW	1.21 ± 0.24
WZ	0.42 ± 0.08
$DY \rightarrow ll$	4.66 ± 1.20
$DY \rightarrow \tau\tau$	0.80 ± 0.19
Fake	3.45 ± 1.38
Total background	10.5 ± 1.86
$t\bar{t}$	17.2 ± 1.39
Total SM expectation	27.8 ± 2.32
Run II DATA	33 ± 5.2

Table 3.4: The numbers of expected background composition with “DIL” selection in $\int Ldt = 340.5\text{pb}^{-1}$. The number of expected $t\bar{t}$ events assumes $\sigma_{t\bar{t}} = 6.7$ pb and $M_t = 175$ GeV/ c^2 . If we assumed 6.1pb of top production cross section, the number of expectation for signal $t\bar{t}$ is decreasing to 15.66. This assumption is needed to compare analysis sensitivity with other CDF measurement.

By such an event selection, we get the acceptance³ curve for top quark mass as shown Fig 3.1.

³Acceptance means the efficiency with obtaining the event due to CDF detector. This value is estimated basically by Monte Carlo Simulation convoluted with CDF detector effect.

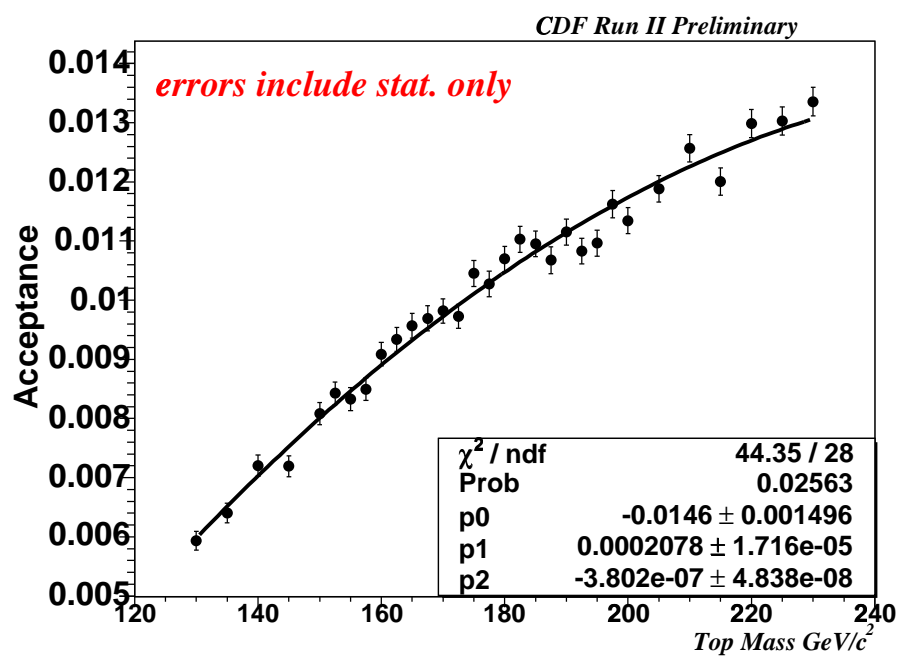


Figure 3.1: The acceptance curve as the function of top quark mass for top dilepton events.

Chapter 4

Top Quark Mass Measurement

4.1 Dynamical Likelihood Method

The dynamical likelihood method (DLM) was first proposed in 1988 [44] and developed [45, 46]. The latest formulation is described in [47].

In DLM of this thesis, the likelihood for a reconstructed parton state is defined by the differential cross section per unit phase space volume of the final partons, using the leading order matrix element as a function of M_t . Top dilepton decay channel gives a clean signature for $t\bar{t}$ events, but it statistically suffers from the low branching ratio of the two leptonic W boson decays. Additionally, due to 2 missing neutrinos, the reconstruction of full parton kinematics is difficult compared to lepton+jets and all hadronic channels. We discuss in this chapter a way to reconstruct the parton kinematics correctly. The goal is to establish a method to reconstruct top quark masses of Monte Carlo (MC) samples in the dilepton channel, and then apply the method to Run II CDF data.

4.1.1 General

Concepts of DLM and details of DLM methodology are found in reference [47]. Here, we present a summary of general formula of differential cross section part.

In $p\bar{p}$ collision process, an interested parton process is described by

$$\begin{aligned} a/A + b/B &\rightarrow C \\ C &\equiv \sum_{i=0}^n c_i, \end{aligned} \tag{4.1}$$

where a and b are initial partons, each representing a quark or an anti-quark or a gluon, in hadrons A and B respectively, and $C(c_1, c_2, \dots, c_n)$ are final state partons. In the dilepton channel, c_i 's correspond to 2 bottom quarks (b, \bar{b}), 2 charged leptons (l^+, l^-) and 2 neutrinos ($\nu, \bar{\nu}$).

Throughout this section, states of all partons are supposed to be after the initial-state radiation and before the final-state radiations, and particle symbol p also represents its 4-momentum, while \mathbf{p} its 3-momentum. We assume that final partons are on mass-shells, i.e. its 3-momentum is enough to define their states and kinematics.

We assume a head-on collision of A and B along the z -axis. Then the hadronic cross-section for process 4.2 is given by

$$d\sigma = dz_a dz_b d^2\mathbf{p}_T f_{a/A}^*(z_a) f_{b/B}^*(z_b) f_T(\mathbf{p}_T) \hat{\sigma}(a + b \rightarrow C; \boldsymbol{\alpha}) \quad (4.2)$$

where $\hat{\sigma}$ is the parton level cross section,

$$\hat{\sigma}(a + b \rightarrow C; \boldsymbol{\alpha}) = \frac{(2\pi)^4 \delta^4(a + b - C)}{4\sqrt{(a \cdot b)^2 - m_a^2 m_b^2}} |\mathcal{M}(a + b \rightarrow C; \boldsymbol{\alpha})|^2 d\Phi_n^{(f)} \quad (4.3)$$

In Eq. (4.2), symbol $\boldsymbol{\alpha}$ stands for a set of dynamical constants, e.g. masses, decay widths or coupling constants. Hereafter, we use $\boldsymbol{\alpha}$ as the top quark mass M_t . Variables $z_a = a_z / |\mathbf{A}|$ and $z_b = b_z / |\mathbf{B}|$ are momentum fractions of a and b in hadrons A and B respectively, and \mathbf{p}_T is the total momentum of the initial/final system of process 4.2 in the plane perpendicular to the beam axis. The probability density functions for these momentum components are denoted by $f_{a/A}^*$, $f_{b/B}^*$ and f_T , respectively.

In Eq. (4.3), \mathcal{M} is the matrix element of the process which is the product of $t\bar{t}$ production and top decay, and $d\Phi_n^{(f)}$ is the Lorentz invariant phase space factor.

$$d\Phi_n^{(f)} \equiv \prod_{i=1}^n \frac{d^3\mathbf{c}_i}{(2\pi)^3 2E_i} \quad (4.4)$$

In DLM, we intend to use the differential cross section as a posterior probability density function to infer the dynamical parameter $\boldsymbol{\alpha}$ which is just now the top quark mass M_t , from parton kinematics $\mathbf{c}(\mathbf{c}_1, \mathbf{c}_2, \dots, \mathbf{c}_n)$. The basic postulate is that final partons occupy an n -dimensional unit phase space in the neighborhood of \mathbf{c} . The total probability for this final state to occur is obtained by integrating Eq. (4.2) with initial state variables z_a, z_b and \mathbf{p}_T as

$$\frac{d\sigma}{d\Phi_n^{(f)}} = I(a, b) |\mathcal{M}(a + b \rightarrow C; \boldsymbol{\alpha})|^2 \quad (4.5)$$

where

$$I(a, b) = \frac{(2\pi)^4}{4|\mathbf{A}||\mathbf{B}|\sqrt{(a \cdot b)^2 - m_a^2 m_b^2}} f_{a/A}^*(z_a) f_{b/B}^*(z_b) f_T(\mathbf{p}_T) \quad (4.6)$$

is the integration factor for the initial state. Because of the δ -function in Eq. (4.3), the initial parton momenta a and b are uniquely defined by that of C .

4.1.2 Reconstruction of parton kinematics

In this subsection, we represent how the kinematics including unit phase spaces volume is defined at the parton level. The precise discussion is found in reference [47]. The parton kinematics, i.e. a set of momenta of resonances and final partons, is defined by (a) giving a full set of final parton momenta $\mathbf{c}(\mathbf{c}_1, \mathbf{c}_2, \mathbf{c}_n)$ and if necessary by (b) inferring resonance mass squared s_r to give one constraint to the momentum of a daughter particle. We assume $c_1^{(\rho)}$ is such a daughter particle. The total number of degrees of freedom for kinematics is $3n$.

The recursion formula of the phase space element is given by [48].

$$\begin{aligned} d\Phi_n &= d\Phi_j(r : c_1, \dots, c_j)(2\pi)^3 ds_r \\ &\times d\Phi_{n-j+1}(a + b : r, c_{j+1}, \dots, c_n) \end{aligned} \quad (4.7)$$

can be rewritten as

$$\begin{aligned} (a) \quad d\Phi_n^{(f)} &= d\Phi_n^{(f)} \delta(s_r - (\sum_{i=1}^j c_i)^2) ds_r \\ (b) \quad d\Phi_n^{(f)} &= \frac{E_r}{E_1^{(r)}} d\Phi_1^{(r)} d\Phi_{n-1}^{(f)}(c_2, \dots, c_n) \delta(s_r - (\sum_{i=1}^j c_i)^2) ds_r \\ &\times \delta^3(c_1^{(\rho)} - \bar{c}_1^{(\rho)}) d^3 c_1^{(\rho)} \end{aligned} \quad (4.8)$$

Integration of δ -functions simply give 1, but we keep these factors to indicate the integration variables explicitly. The δ -function of s_r requires

$$s_r = r^2 = (\sum_{i=1}^j c_i)^2 \quad (4.9)$$

If 3-momentum $\mathbf{c}^{(\rho)}(\mathbf{c}_1^{(\rho)}, \mathbf{c}_2^{(\rho)}, \mathbf{c}_n^{(\rho)})$ and masses of daughter partons are given, s_r is determined by Eq. (4.9). On the contrary, if s_r is given, Eq. (4.9) gives one constraint on $\mathbf{c}^{(\rho)}$. In Eq. (4.9), $c_1^{(\rho)}$ represents the daughter momentum determined including this constraint.

If we denote n body phase space factor by $d\Phi_n^{(*)}$ in general, where symbol * represents partons used for determination of the kinematics, phase space factors are: (a) $d\Phi_n^{(*)} = d\Phi_n^{(f)}$, and (b) $d\Phi_n^{(*)} = d\Phi_1^{(r)} d\Phi_{n-1}^{(f)}$. The cross section per unit phase volume is given by

$$\begin{aligned} (a) \quad \frac{d\sigma}{d\Phi_n^{(*)}} &= \frac{d\sigma}{d\Phi_n^{(f)}} \delta(s_r - (\sum_{i=1}^j c_i)^2) ds_r \\ (b) \quad \frac{d\sigma}{d\Phi_n^{(*)}} &= \frac{E_r}{E_1^{(\rho)}} \frac{d\sigma}{d\Phi_n^{(f)}} \delta(s_r - (\sum_{i=1}^j c_i)^2) ds_r \delta^3(c_1^{(\rho)} - \bar{c}_1^{(\rho)}) d^3 c_1^{(\rho)} \end{aligned} \quad (4.10)$$

If there are a total of n_r resonances (r_1, \dots, r_{n_r}) in the process with virtual masses squared $\mathbf{s}(s_1, \dots, s_{n_r}, |\mathcal{M}(a + b \rightarrow C)|^2)$ contains n_r propagator factors, and one can use $s_1, \dots, s_h (h \leq$

n_r) to define the parton kinematics, where choice of h depends on the process and the purpose of analysis. The cross section per unit phase volume is generally given by

$$\frac{d\sigma}{d\Phi_n^{(*)}} = F_r \frac{d\sigma}{d\Phi_n^{(f)}} \quad (4.11)$$

where we call

$$F_r = \prod_{i=i}^h \frac{E(r_i)}{E(c(\rho_i))} \quad (4.12)$$

the *resonance factor*. We define $F_r = 1$ for $h = 0$.

4.1.3 DLM in dilepton channel

The tree level process of this channel is expressed as

$$t\bar{t} \rightarrow (bW^+)(\bar{b}W^-) \rightarrow (bl^+\nu)(\bar{b}l^-\bar{\nu}) \quad (4.13)$$

In principle, the decay of $t\bar{t}$ pair production include 18 independent momentum variables due to the assumption for partons to be on shell mass, but there is only 14 observable quantities in this channel. 3 momenta of 2 leptons and 2 jets are measured by the CDF Tracking detector and the Calorimeter, respectively. As for neutrinos, CDF detector gives \cancel{E}_T information, i.e. the transverse sum of all clustered energies. In Dilepton channel, the independent quantities used as the input variables are $(\mathbf{b}, \bar{\mathbf{b}}, \mathbf{l}^+, \mathbf{l}^-)$, \cancel{E}_x and \cancel{E}_y . The expression of the likelihood for the i -th event can be written as

$$\begin{aligned} L^i(M_t) &= \frac{l_0 F_R w}{acc(M_t)} \frac{d\sigma}{d\Phi(f)} \\ &= l_0 F_R \sum_{comb} \sum_{nsol} \frac{(2\pi)^4}{Flux} f_{a/A}^*(z_a) f_{b/B}^*(z_b) |\mathcal{M}|^2 w(c|y||M_t) \\ &\quad \frac{1}{acc(M_t)} w_\nu(\nu_z, \bar{\nu}_z, U_x, U_y) \end{aligned} \quad (4.14)$$

where l_0 can be written as $l_0 = 1/\sigma_T = L_{int}\epsilon/N_{tot}$ by using the total cross section σ_T , integrated luminosity L_{int} , detection efficiency ϵ , total number of events N_{tot} . Total cross section σ_T is a function M_t , but here we interpret it an observable variable intrinsic to the given data set, and do not take the mass dependence in the on top quark mass reconstruction. F_R is a resonance factor which is already described at Eq. (4.11). As for parton distribution $f_{a/A}^*(z_a) f_{b/B}^*(z_b)$, we employ CTEQ5L in order to be consistent with leading order calculation. $w(c|y||M_t)$ is Transfer Function (T.F.) which infers parton c from observable quantities y . The more precise study will be denoted in section 4.2. “acc” stands for acceptance correction factor which is specified by Top Dilepton event selection which is described in section 3.2. w_ν is neutrino kinematics weight which is required to enhance neutrino true solution. This will be discussed in the subsection

4.1.5

Matrix element squared of this channel $|\mathcal{M}|^2$ can be written as

$$|\mathcal{M}|^2 = |\mathcal{M}_{prod}|^2 |\mathcal{M}_{decay}|^2 \quad (4.15)$$

where suffix *prod* and *decay* indicate $t\bar{t}$ production matrix element and W decay matrix element respectively. Furthermore, spin averaged production matrix element can be expressed as

$$|\mathcal{M}(q\bar{q} \rightarrow t\bar{t})|^2 = \frac{g_s^4}{9} (2 - \beta^2 \sin^2 \theta^*) \quad (q\bar{q} \rightarrow t\bar{t}) \quad (4.16)$$

$$|\mathcal{M}(gg \rightarrow t\bar{t})|^2 = g_s^4 \left(\frac{1}{6\tau_1\tau_2} - \frac{3}{8} \right) (\tau_1^2\tau_2^2 + \rho - \frac{\rho^2}{4\tau_1\tau_2}) \quad (gg \rightarrow t\bar{t}) \quad (4.17)$$

where θ^* is an angle between top and incoming quark or gluon inside the proton in the $t\bar{t}$ center of mass system, and β is a velocity of top and g_s is a strong coupling constant.

$$\beta = \sqrt{1 - 4m_t^2/\hat{s}^2} \quad (4.18)$$

$$\tau_1 = \frac{2(q \cdot t)}{\hat{s}}, \quad \frac{2(\bar{q} \cdot t)}{\hat{s}}, \quad \rho = \frac{4M^2}{\hat{s}} \quad (4.19)$$

The decay matrix element is expressed as

$$|\mathcal{M}(t \rightarrow lb\nu)|^2 = \frac{g_s^4}{4} \frac{(t \cdot l)(b \cdot \nu)}{[(S_{lb\nu} - M_t^2)^2 + M_t^2\Gamma_t^2][(S_{l\nu} - M_W^2)^2 + M_W^2\Gamma_W^2]} \quad (4.20)$$

where $S_{lb\nu}$ and $S_{l\nu}$ are invariant mass squared of top and W in this channel. In our analysis we assumed $M_W = 80.4 \text{ GeV}/c^2$ and $\Gamma_W = 2.12 \text{ GeV}/c^2$. The top decay width is given by

$$\Gamma_t = \frac{g_s M_t^3}{8\pi\sqrt{2}} |V_{tb}|^2 \left(1 - \frac{M_W^2}{M_t^2}\right)^2 \left(1 + \frac{2M_W^2}{M_t^2}\right) \quad (4.21)$$

This decay rate is simplified such that in the case of $q^2/Q^2 \ll 1$ found in reference [49]. $|V_{tb}|^2$ is one of parameters of CKM quark mixing matrix squared.

4.1.4 Neutrino kinematics

Here we describe the details of how to determine neutrino 4-momentum. There are two neutrinos in dilepton channel, while measurement of \vec{E}_T gives only two constraints. Therefore $6 - 2 = 4$ constraints are still needed to determine neutrino momenta. For this purpose, we use the mass relations of top, anti-top, W^+ and W^- . These 4 relations are reduced to a fourth-order algebraic equation and can be analytically solved.

The mass relations are

$$\begin{aligned} (b + l^+ + \nu)^2 &= S_t, & (\bar{b} + l^- + \bar{\nu})^2 &= S_{\bar{t}} \\ (l^+ + \nu)^2 &= S_{l\nu}, & (l^- + \bar{\nu})^2 &= S_{l\bar{\nu}} \end{aligned} \quad (4.22)$$

Missing E_T information is expressed below :

$$\nu_x + \bar{\nu}_x = T_x, \nu_y + \bar{\nu}_y = T_y \quad (4.23)$$

$$\mathbf{T} = (\vec{E}_x, \vec{E}_y, 0) \quad (4.24)$$

From these equations, vector momenta of neutrino are:

$$\boldsymbol{\nu} = \nu_0 \boldsymbol{\alpha} + \bar{\nu}_0 \boldsymbol{\beta} + \boldsymbol{\gamma} \quad (4.25)$$

$$\bar{\boldsymbol{\nu}} = \bar{\nu}_0 \bar{\boldsymbol{\alpha}} + \nu_0 \bar{\boldsymbol{\beta}} + \bar{\boldsymbol{\gamma}} \quad (4.26)$$

$$\boldsymbol{\alpha} = \frac{1}{\Delta_z} [g_z \bar{\mathbf{c}} - (\mathbf{g} \cdot \bar{\mathbf{c}})], \boldsymbol{\beta} = \frac{\bar{g}_z}{\Delta_z} \mathbf{c}, \boldsymbol{\gamma} = \frac{1}{\Delta_z} [\bar{g}_{0z} \mathbf{c} + g_{0z} \bar{\mathbf{c}} - d_z \mathbf{c} - (\mathbf{g}_0 \cdot \bar{\mathbf{c}}) \hat{z}] \quad (4.27)$$

where vector factors are defined by $\mathbf{c} = \mathbf{l} \times \mathbf{b}$, $\boldsymbol{\Delta} = \mathbf{c} \times \bar{\mathbf{c}}$, $\mathbf{d} = \bar{\mathbf{c}} \times \mathbf{T}$, $\mathbf{g}_0 = \tau \mathbf{b} - \kappa \mathbf{l}$, $\mathbf{g} = l_0 \mathbf{b} - b_0 \mathbf{l}$ with scalar factors $\tau = -(s_{l\nu} - l^2 - \nu^2)/2$, $\kappa = [s_{l\nu} - s_t^2 + b^2 + 2(\mathbf{b} \cdot \mathbf{l})]/2$. Vectors $\bar{\boldsymbol{\alpha}}, \bar{\boldsymbol{\beta}}, \bar{\boldsymbol{\gamma}}$ are defined by replacing each variable $x(\bar{x})$ with $\bar{x}(x)$.

$$\bar{\boldsymbol{\alpha}} = \frac{1}{\bar{\Delta}_z} [\bar{g}_z \mathbf{c} - (\bar{\mathbf{g}} \cdot \mathbf{c})], \bar{\boldsymbol{\beta}} = \frac{\bar{g}_z}{\bar{\Delta}_z} \mathbf{c}, \bar{\boldsymbol{\gamma}} = \frac{1}{\bar{\Delta}_z} [g_{0z} \bar{\mathbf{c}} + g_{0z} \mathbf{c} - \bar{d}_z \bar{\mathbf{c}} - (\bar{\mathbf{g}}_0 \cdot \mathbf{c}) \hat{z}] \quad (4.28)$$

Because mass of neutrino is equal to zero, we have got a bi-quadratic equation for energies of two neutrinos, ν_0 and $\bar{\nu}_0$, like

$$(|\boldsymbol{\alpha}|^2 - 1)\nu_0^2 + 2(\boldsymbol{\alpha} \cdot \boldsymbol{\beta})\nu_0\bar{\nu}_0 + |\boldsymbol{\beta}|^2\bar{\nu}_0^2 + 2(\boldsymbol{\gamma} \cdot \boldsymbol{\alpha})\nu_0 + 2(\boldsymbol{\beta} \cdot \boldsymbol{\gamma})\bar{\nu}_0 + |\boldsymbol{\gamma}|^2 = 0 \quad (4.29)$$

$$(|\bar{\boldsymbol{\alpha}}|^2 - 1)\bar{\nu}_0^2 + 2(\bar{\boldsymbol{\alpha}} \cdot \bar{\boldsymbol{\beta}})\nu_0\bar{\nu}_0 + |\bar{\boldsymbol{\beta}}|^2\nu_0^2 + 2(\bar{\boldsymbol{\gamma}} \cdot \bar{\boldsymbol{\alpha}})\bar{\nu}_0 + 2(\bar{\boldsymbol{\beta}} \cdot \bar{\boldsymbol{\gamma}})\nu_0 + |\bar{\boldsymbol{\gamma}}|^2 = 0 \quad (4.30)$$

Once these bi-quadratic equations are converted to one fourth-order equation, it can be analytically solved, and thus at most four solutions could be obtained. Fig. 4.1 and 4.2 indicates how they are solved about the energies of neutrino and anti-neutrino accurately, when we know correct invariant masses for t, \bar{t}, W^+, W^- .

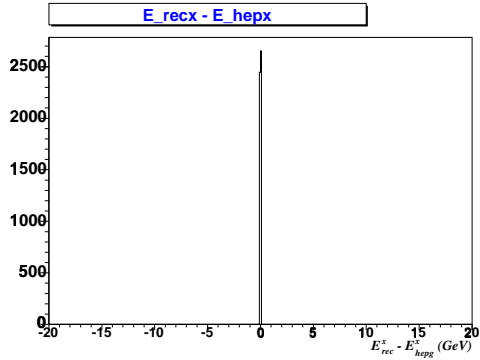


Figure 4.1: The difference of neutrino energies between reconstructed (solved) and generator input. The x component of neutrino energy can be solved well.

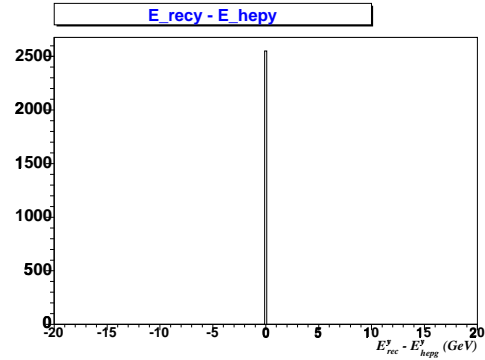


Figure 4.2: The difference of anti neutrino energies between reconstructed (solved) and generator input. The y component of neutrino energy can be solved well.

Once getting correct neutrino and anti-neutrino energies, we could reconstruct neutrino full parton kinematics by using Eq. (4.25) and Eq. (4.26). The neutrino kinematics solutions gives each of the assumed resonance invariant masses as well.

4.1.5 Neutrino kinematics weight

In this section, we present the “neutrino kinematics weight”, an additional factor to the cross section for the top quark mass estimation, using non-simulated i.e. generator sample. Throughout this thesis, generator ample indicates that where all kinematic variables in each event are those given at the parton (generator) level of the Monte Carlo events. To check the DLM machinery for the mass reconstruction, we perform two kinds of the generator level examination. Check (1) is done by using $t\bar{t}$ full kinematics at the generator level, i.e. 3-momentum of 6 tree level partons, and Check (2) is made by using observable quantities only at the generator level, i.e. the 3-momentum of $(l^+, l^-, b, \bar{b},)$ and $\vec{\cancel{E}}_T$, but not for full kinematics. In case (2), the invariant mass of each resonance is generated by random numbers according to the Breit Wigner shape to define the mass relations Eqs. (4.22).

First, we calculate the likelihood without Neutrino Kinematics Weight. Figure 4.3 shows the reconstructed top quark mass with assumption (1). In case of check (1), parton momenta including 2 neutrino momenta are all known. Figure 4.4 is an example of the reconstructed top quark mass with assumption (2), hence by solving neutrino 3-momentum as discussed in the subsection 4.1.4

Figure 4.4 gives us some understanding about the effect to solve neutrino 3-momentum by using machinery of the previous section. Although solutions can be obtained as we expect, the reconstructed mass value is higher than expected. This higher peak implies that solutions obtained by using machinery of previous subsection 4.1.4, have good and bad solutions but they

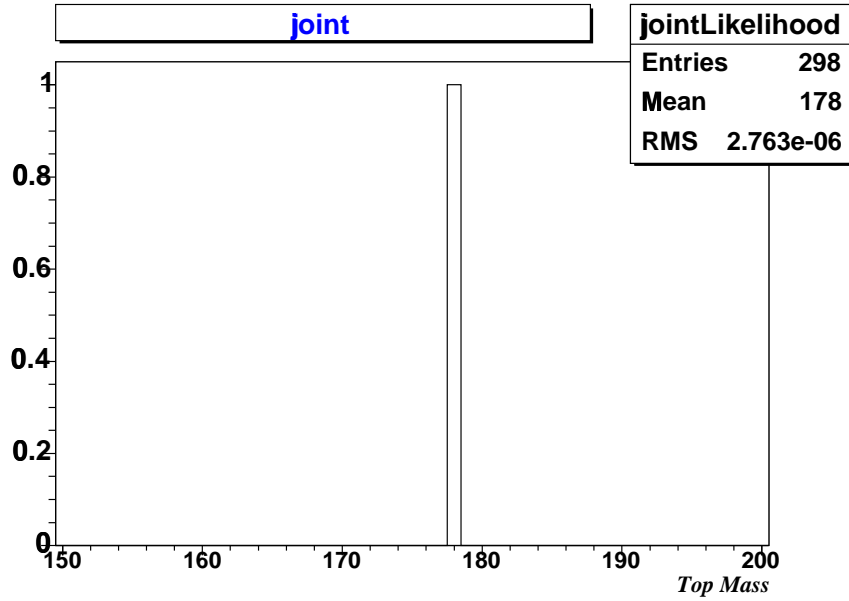


Figure 4.3: 100 event joint likelihood distribution with performance (1). If we know $t\bar{t}$ full kinematics, we can reconstruct top quark mass by using DLM likelihood. Sample is generated by HERWIG MC, $M_t = 178 \text{ GeV}/c^2$

are not distinguished with standard DLM likelihood. To solve this problem, we consider the neutrino kinematics weight to enhance only good solutions. One may say that the neutrino weight factor is a “pseudo transfer function” for unobserved components of neutrino kinematics. We employed the variables $U_x, U_y, \nu_z, \bar{\nu}_z$ as the neutrino kinematics weight. Variables U_x, U_y is orthogonal to $\cancel{E}_x, \cancel{E}_y$. Figures 4.5 and 4.6 show the typical probability density function of $(U_x, U_y), (\nu_z, \bar{\nu}_z)$. To use this neutrino kinematics weight, we fit them for 130 to 230 GeV/c^2 Top Mass MC samples with gauss convoluted exponential function, because the weights have slightly top mass dependence as can be seen in Figs 4.7 to 4.10. The fit function $f(x)$ is taken as

$$f(x) = g(x) \otimes h(x) \quad (4.31)$$

$$g(x) = \frac{k}{2} e^{-k|x|} \quad (4.32)$$

$$h(x) = \frac{1}{\sqrt{2\pi}\sigma} e^{-\frac{x^2}{2\sigma^2}} \quad (4.33)$$

Figures 4.7 to 4.10 show the top mass dependence of the parameters, k and σ . Here, we fit them with a linear function due to good agreement. As a consequence, these neutrino kinematics weights are convoluted with DLM likelihood such as in Eq. (4.14).

Once applying this neutrino kinematics weight, we can see better separation between good and bad solutions. Figure 4.11 demonstrates the separation of good/bad solutions. Figure 4.12

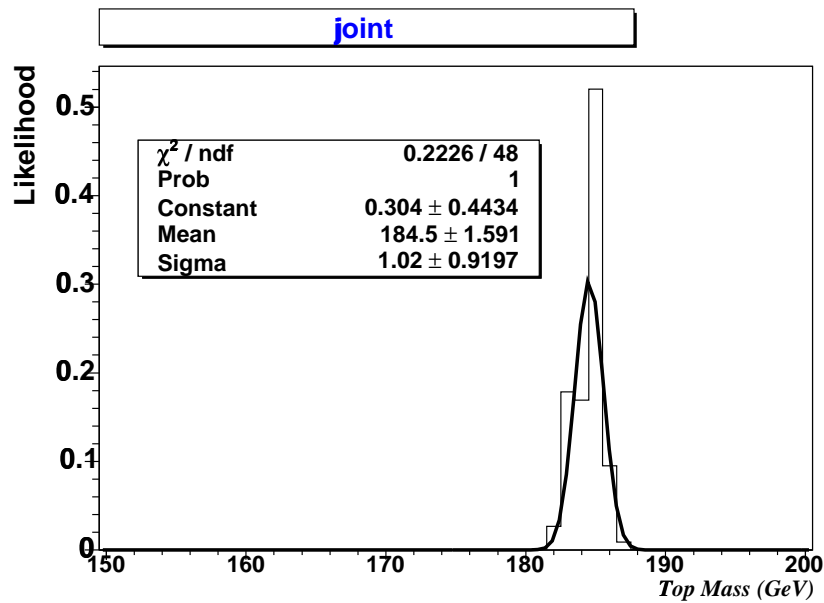


Figure 4.4: 200 event joint likelihood distribution with performance (2). The width of reconstructed top quark mass imply the ambiguity of neutrino kinematics. Reconstructed top mass is too high against input top quark mass. Sample is generated by HERWIG MC, $M_t = 178 \text{ GeV}/c^2$

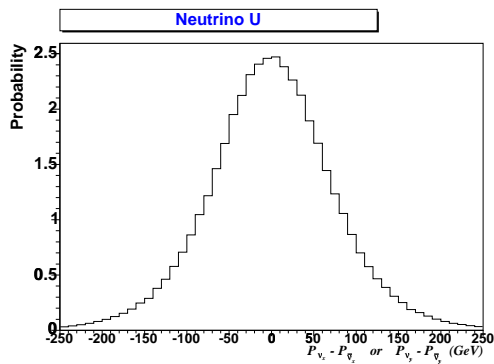


Figure 4.5: The probability density as a function of U variable. U_x and U_y have the same shape.

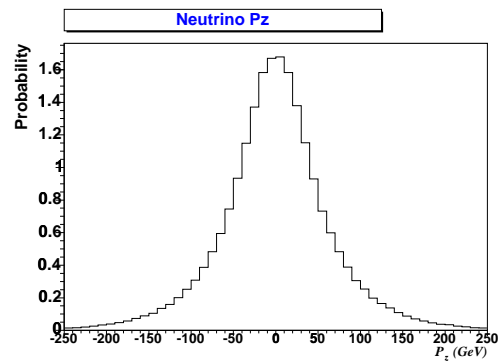


Figure 4.6: The probability density as a function of P_z variable. P_z and \bar{P}_z have the same shape.

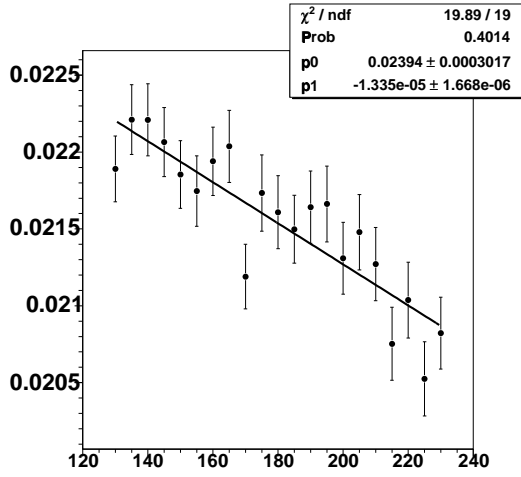


Figure 4.7: The parameter of k for P_z depends on top quark mass. We fit them with a linear function.

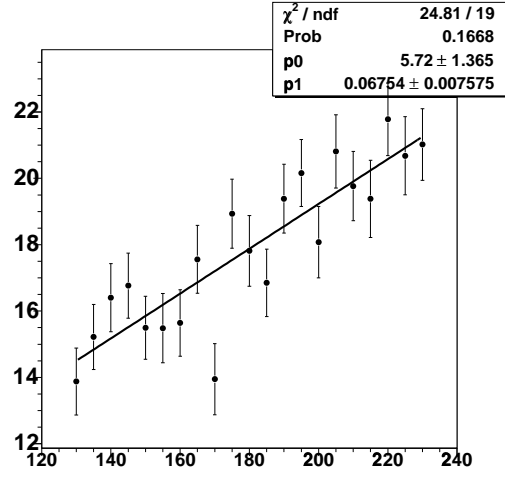


Figure 4.8: The parameter of σ for P_z depends on top quark mass. We fit them with a linear function.

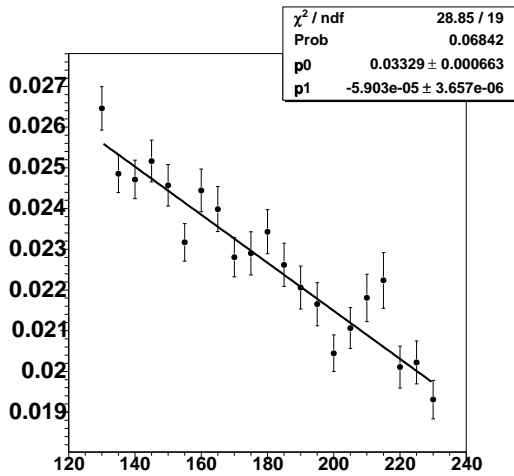


Figure 4.9: The parameter of k for U depends on top quark mass. We fit them with a linear function.

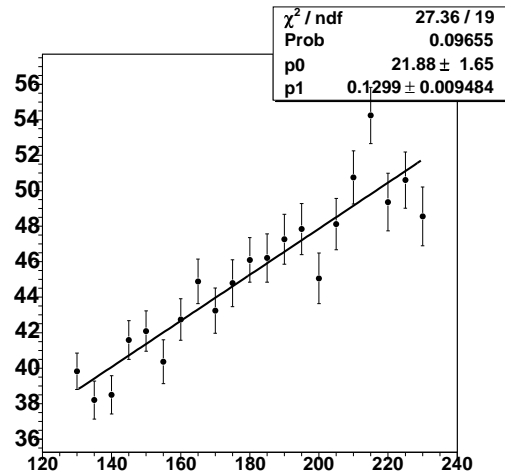


Figure 4.10: The parameter of σ for U depends on top quark mass. We fit them with a linear function.

shows the top mass reconstruction result by using 200 event joint likelihood with convolute neutrino kinematics weight.

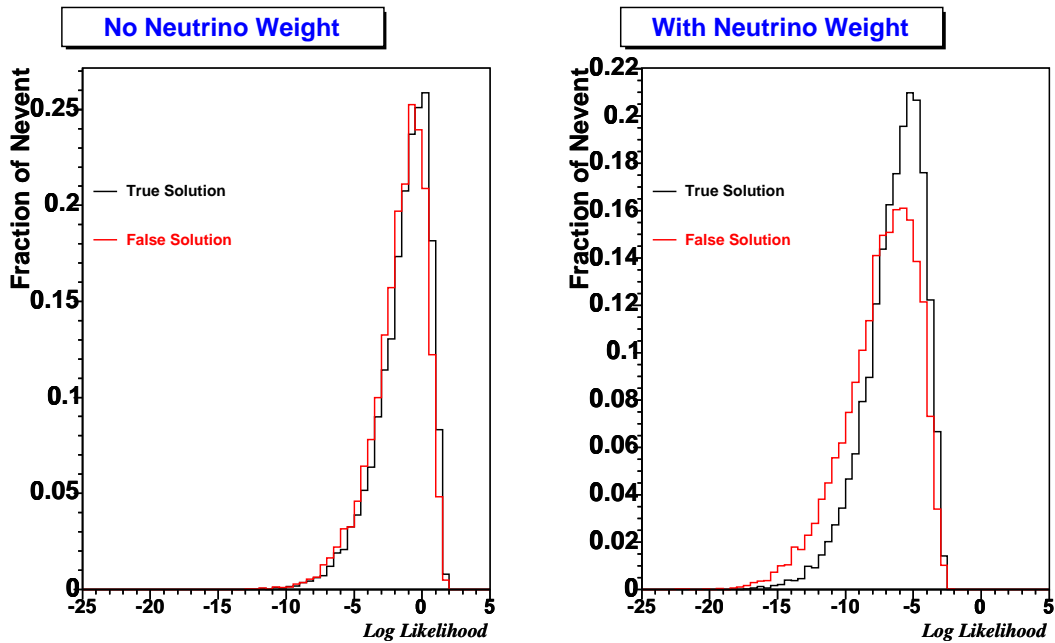


Figure 4.11: Fraction of event as a function of log likelihood of an event. Red lines show the results of the calculation for only false neutrino kinematics topology. Black lines show the results of the calculation for only true neutrino kinematics topology. These figures show the separation of good/bad solutions. By adopting neutrino kinematics weight, the likelihood ratio of good/bad solutions could be enhanced by 10 times. Here the true solution means true neutrino kinematics of an event, on the contrary the false solution means other neutrino kinematics than the truth, when we solve the neutrino momenta with the use of correct resonance invariant masses.

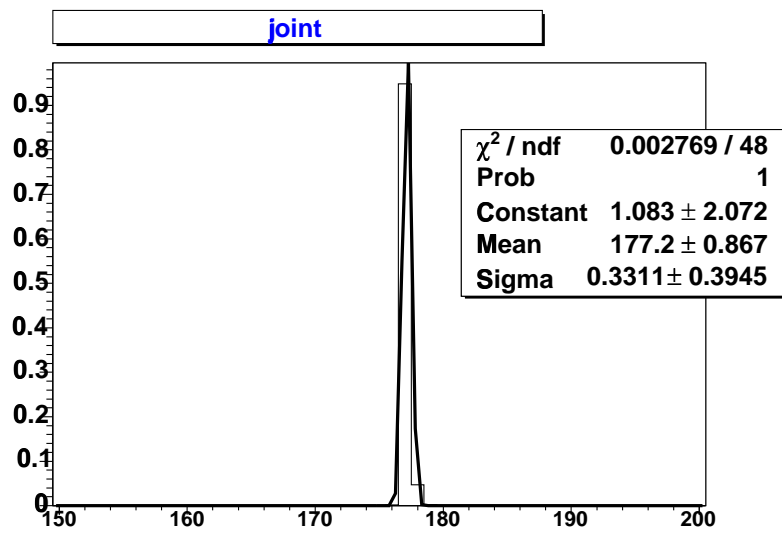


Figure 4.12: 2000 event joint likelihood distribution with performance (2). The likelihood we used is convoluted neutrino kinematics weight. Reconstructed top mass peak is better than Fig. 4.4 due to the effect of enhancing good solution.

4.2 Transfer Function

The transfer function plays a significant role in DLM calculation. The detailed discussion of Transfer function is given in reference [47]. As we argued in Chapter 2, CDF detectors have calorimeters and the tracking system. They give energies and momenta of particles respectively. A jet is generally identified with a quark (anti-quark) or a gluon. An electromagnetic shower associated with or without a track is assigned to an electron or a photon. A track passing through calorimeters with a minimum ionizing signal is identified with a muon. We call these particles *observable partons* and their measured quantities *observables*. The transfer function describes the relation between *observables* and *observable partons*, then connects to each other.

4.2.1 Transfer functions for observable quantities

Here, we present a general definition of transfer functions and their quantities.

For a real event in experiment, the final observables are known, while the parton state in process Eq. (4.2) is unknown. The event reconstruction in DLM is to infer such unknown parton state that leads to an observed variable set $\mathbf{y}(y_1, \dots, y_{N_V})$. The parton variable set corresponding to \mathbf{y} is denoted by $\mathbf{x}(x_1, \dots, x_{N_V})$. We call \mathbf{x} and \mathbf{y} transfer variables.

Prior transfer function The prior transfer function is a probability density function (p.d.f.) for \mathbf{y} when \mathbf{x} is given and denoted by $w(\mathbf{y}|\mathbf{x}||i_p, \boldsymbol{\alpha})$, where i_p is an integer to specify the process. The probability for (\mathbf{x}, \mathbf{y}) to be in $(d\mathbf{x}, d\mathbf{y})$ is

$$dP(\mathbf{x}, \mathbf{y}||i_p) = w(\mathbf{y}|\mathbf{x}||i_p, \boldsymbol{\alpha}) d\mathbf{x}d\mathbf{y}. \quad (4.34)$$

where

$$d\mathbf{x} \equiv \prod_{m=1}^{N_V} dx_m, \quad d\mathbf{y} \equiv \prod_{m=1}^{N_V} dy_m. \quad (4.35)$$

If $w(\mathbf{y}|\mathbf{x}||\boldsymbol{\alpha}) > 0$, a certain value of \mathbf{y} should exist. Hence we require the normalization condition,

$$\int_{w>0} w(\mathbf{y}|\mathbf{x}||\boldsymbol{\alpha}) d\mathbf{y} = 1, \quad (4.36)$$

for any \mathbf{x} with $w > 0$.

A typical example of a component of \mathbf{y} is the energy of a jet. The T.F. for a jet depends on models of parton-shower and fragmentation, the detector response and the jet reconstruction algorithm. Thus it is appropriate to derive the T.F. by using Monte Carlo event generators with full simulation, where the momentum of each parton and measured quantities associated with it are provided. Events are to be selected with the same criteria as applied to real data.

$w(\mathbf{y}|\mathbf{x}||\boldsymbol{\alpha})$ from Monte Carlo events The T.F. is a function of multi-dimensional variables \mathbf{x} and \mathbf{y} . To make the argument simple, we assume that the T.F. is factorisable as

$$w(\mathbf{y}|\mathbf{x}||i_p, \boldsymbol{\alpha}) = \prod_{m=1}^{N_V} w(y_m|x_m||i_p, \boldsymbol{\alpha}). \quad (4.37)$$

We denote the T.F. by $w(y|x|\alpha)$, assuming the dynamical parameter in search is one and abbreviating process number i_p and variable number m .

Let n_{xy} denote the density of generated number of the Monte Carlo events at (x, y) , and n_x that at x . T.F. $w(y|x|\alpha)$ is defined such that the number of events in (dx, dy) is given by

$$dN(x, y) = n_{xy} dx dy = n_x dx \times w(y|x|\alpha) dy. \quad (4.38)$$

With the integrated luminosity L_{int} , the number densities are given by

$$n_{xy} = L_{int} \frac{d\sigma}{dx} w(y|x|\alpha), \quad n_x = \int n_{xy} dy = L_{int} \frac{d\sigma}{dx}. \quad (4.39)$$

The y dependence of the detection efficiency is included in

From Eq. (4.38), the T.F. is given by

$$w(y|x|\alpha) = \frac{n_{xy}}{n_x} = \sum_{i=1}^{n_{xy}} \frac{1}{n_x}. \quad (4.40)$$

Thus $w(y|x|\alpha)$ is obtained by filling the (x, y) histogram with weight $1/n_x$ for each event. Weighting by $1/n_x$ is to avoid the double counting of the cross section factor which exists in the parton level likelihood. Integrating Eq. (4.40) by y and using Eq. (4.39), one obtains the normalization condition, Eq. (4.36).

Posterior T.F. $w(y|x|\alpha)$ T.F. $w(y|x|\alpha)$ discussed in the preceding paragraph is a prior T.F. since it is obtained from the Monte Carlo event distributions. We use the posterior T.F. in the reconstruction of the parton level. The posterior T.F. is given in terms of the prior T.F. as

$$w(x|y|\alpha) = w(y|x|\alpha) / \int w(y|x|\alpha) dx. \quad (4.41)$$

4.2.2 Jet transfer function

In this subsection, we move to discuss the transfer function in dilepton channel. First, we represent jet energy transfer function in dilepton DLM. Throughout this transfer function arguments, we use Monte Carlo generators HERWIG combined with CDF detector simulator. As for measured quantities, we employ the generic corrected jet after ‘‘Absolute’’ correction on 3.1.3. These generic corrections correspond to compensation of CDF detector response not including physics effects, i.e. parton radiation and hadronization effects. Jet energy transfer variable ξ (response variable) is defined by

$$\xi = \frac{E_T(parton) - E_T(jet)}{E_T(parton)} \quad (4.42)$$

where $E_T(jet)$ indicates the quantities after CDF generic corrections described in sub-section 3.1.3. All jets meet the dilepton tight jet requirement; E_T should be greater than 15 GeV.

Second, we describe jet direction transfer function in dilepton DLM. Jet direction transfer function describe the relations of direction between tree level parton and observed jet quantities after CDF generic corrections. Jet direction transfer function variable $\Delta\eta$ and $\Delta\phi$ can be expressed as

$$\Delta\eta = \eta(\text{parton}) - \eta(\text{jet}) \quad (4.43)$$

$$\Delta\phi = \phi(\text{parton}) - \phi(\text{jet}) \quad (4.44)$$

To validate the jet transfer function performance, we apply the transfer function to identified b jet under jet to parton matching¹ condition $\Delta R < 0.4$ in the events which passed the dilepton event selection is discussed in section 3.2. After applying jet transfer function, we reconstruct top invariant masses. At that point, 4-momenta of charged leptons and neutrinos at generator level are used. The energies and the directions of b jets are inferred by the random generations of the response variable according to each transfer function. After all scanning, distributions of top invariant mass is obtained for each event. To pick up the value of top invariant mass of each event, we select the mean value of its distribution at each event. A performance check for top mass reconstruction is shown in Figure 4.13.

4.2.3 Missing Transverse energies transfer function

Next, we discuss Missing transverse energy (MET) transfer function in dilepton DLM. The role of MET transfer function is to infer sum of the transverse momenta of 2 neutrinos from the observed MET. The raw \cancel{E}_T is a 2 dimensional vector $(\cancel{E}_x, \cancel{E}_y)$, in the xy transverse plane, equal to the negative of the vector sum of all the transverse energy in calorimeter. CDF offline tools give some correction to the raw \cancel{E}_T as follows.

1. **Primary vertex correction** : The raw missing energy assumes that the events primary vertex is $z = 0$, but we find the primary vertex for the event and then recalculate $(\cancel{E}_x, \cancel{E}_y)$.
2. **Muon correction** : The muons are minimum ionizing and they deposited very little energy in the calorimeter; therefore we add back to $(\cancel{E}_x, \cancel{E}_y)$ the transverse energy deposited in the calorimeter and subtract the muon transverse energy, (P_x, P_y) .
3. **Jet correction** : b jet energies are corrected by using generic correction as described section 3.1.3, so we have to compensate the effect of b jet energy generic correction against MET in the dilepton candidates.

After jet energy generic correction, there is the procedure to apply jet transfer function to corrected jet in DLM analysis as previously described. With applying jet transfer function,

¹Matching algorithm denotes parton identification for observed jet. To do this, we require the kinematical value between generator tree level parton and observed jet. Here we take it as $\Delta R < 0.4$ due to the identification.

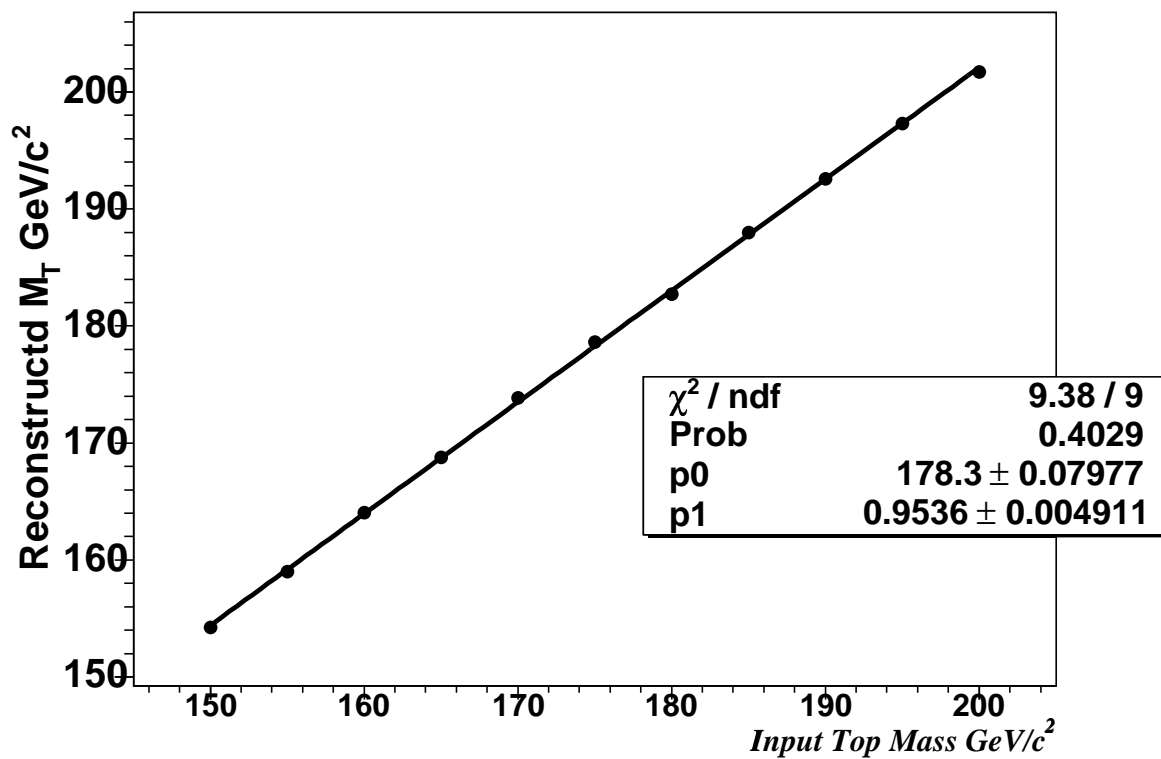


Figure 4.13: The demonstration of jet transfer function performance. Reconstructed top invariant mass: b parton momenta are inferred by using jet transfer function, momenta of lepton and neutrino are the values at generator level.

we need to additionally compensate the effect of application of jet transfer function against transverse missing energy (raw \cancel{E}_T). This procedure getting rid of correlations between jet and MET transfer function, denote MET variable doesn't depend on observed jets. The expression of correlation free MET as we called 'corrected MET' is written as

$$\cancel{E}_T^{cor} = \cancel{E}_T^{dil} - \sum_j (E_T^b - E_T^{jetcor})_j \quad (4.45)$$

where \cancel{E}_T^{dil} stands for the original dilepton \cancel{E}_T (raw \cancel{E}_T). E_T^b and E_T^{jetcor} means E_T of tree level b parton and the corrected jet after further jet transfer function correction respectively. \cancel{E}_T^{cor} means what we re-define as a MET value here.

At the end, this MET transfer function includes the resolution of unclustered energy, some soft leptons and loose jets which are not treated at all. In our analysis, we assumed lepton is well measured, therefore its resolutions involves even the uncertainty of this assumption.

MET transfer function variable ξ can be expressed as

$$\xi = \frac{|\sum_{1,2} \vec{\nu}_T| - \cancel{E}_T^{cor}}{|\sum_{1,2} \vec{\nu}_T|} \quad (4.46)$$

As we define jet direction transfer function, MET phi transfer function is defined as well. MET phi transfer function variable $\Delta\phi_{met}$ can be expressed as

$$\Delta\phi_{met} = \phi_{met}(\nu_1 + \nu_2) - \phi_{met}(cor) \quad (4.47)$$

4.2.4 Transfer Function Summary

We know that the T.F.s are strongly dependent on E_T of jets or \cancel{E}_T . Therefore we introduce these dependences by slicing E_T of jets into 11 bins, i.e. 15-25-35-45-55-65-75-90-105-140-180 < GeV, \cancel{E}_T into 9 bins, i.e. 25-35-45-55-65-75-85-100-130 < GeV, and $|\eta|$ into 3 bins, i.e. 0.0-0.2-0.6 <. It is also known to depend on pseudo rapidity η slightly. In fact, when we apply the transfer function to DLM calculation, these dependence is included.

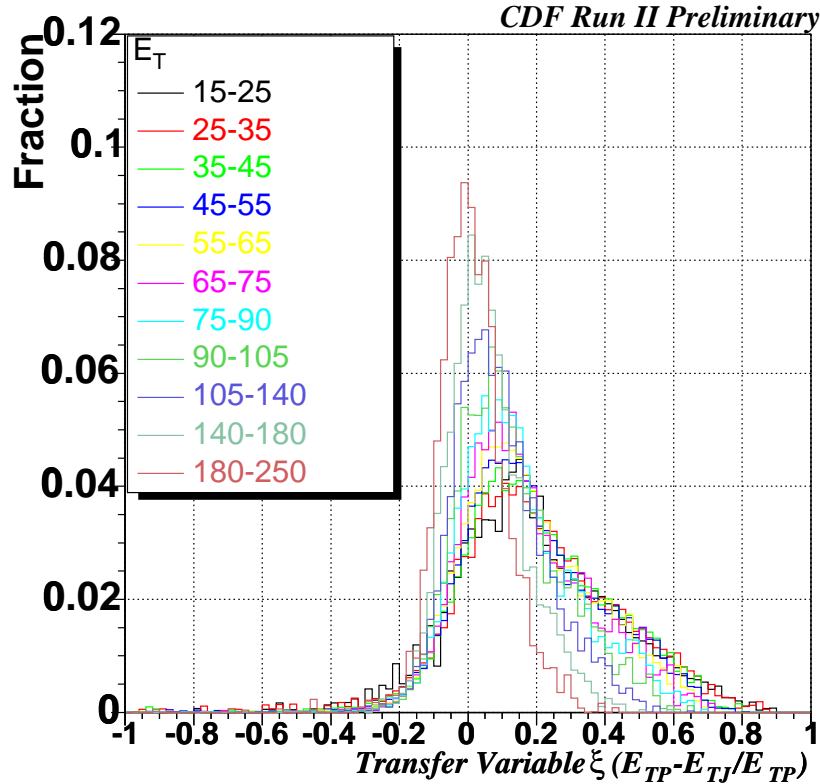


Figure 4.14: Comparisons of each jet energy transfer function. The function highly depends on jet energy.

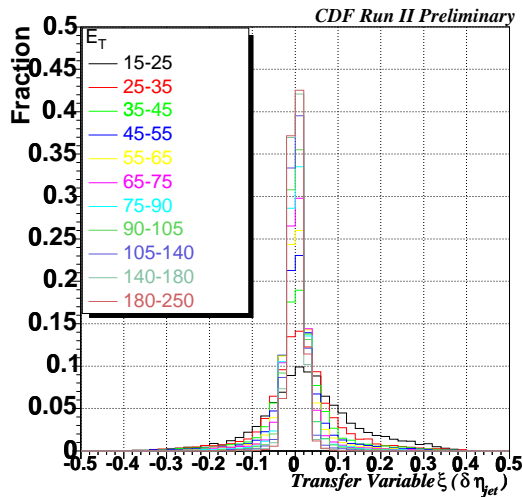


Figure 4.15: Comparisons of each jet eta transfer function. The function highly depends on jet energy.

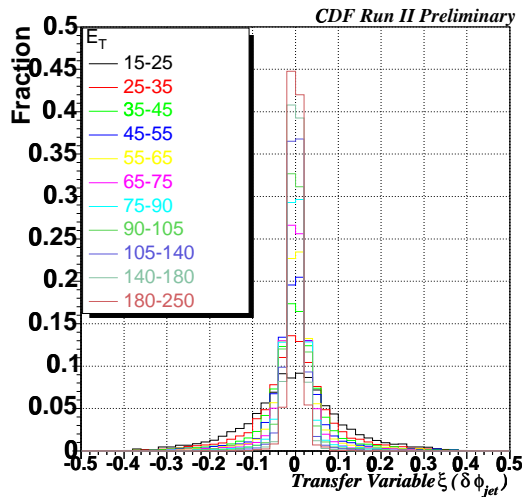


Figure 4.16: Comparisons of each jet phi transfer function. The function highly depends on jet energy.

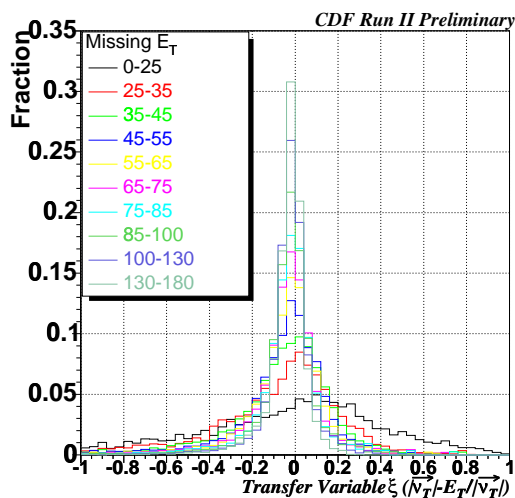


Figure 4.17: Comparisons of each MET transfer function. The function highly depends on \cancel{E}_T .

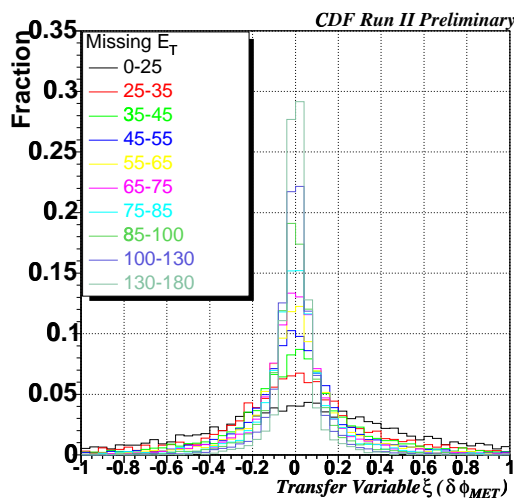


Figure 4.18: Comparisons of each MET phi transfer function. The function highly depends on \cancel{E}_T .

4.3 Top Quark Mass Estimation

In this section, we explain how we extract top quark mass by using dilepton DLM technique with top signal Monte Carlo sample.

After CDF simulation and dilepton event selection as described in Chapter 3, we obtain signal candidates with 2 or more jets to the signal MC sample. Then we examine jet to b parton matching, requiring $\Delta R(b \text{ parton, jet}) < 0.4$. We classify events into two categories throughout our analysis. The first sample is *pure* sample in which two b jets are completely matched. This matching requirement is not always satisfied even for a signal event. In this pure sample, there still remains b and \bar{b} ambiguity. The second sample is the *full* sample where jet to b parton matching is not required. The full sample includes τ decay events which do not correspond to dilepton candidate. However, “lepton + jets” events are vetoed in MC event selection. This top signal contamination² would be fake background.

4.3.1 Likelihood Calculation

In likelihood calculation, the top mass region is searched from 128 to 228 by every 1 GeV/ c^2 . Figure 4.19 show the examples of likelihood distribution for top mass between 128 GeV/ c^2 to 228 GeV/ c^2 . Figure 4.20 demonstrate the top mass linearity for reconstruction with pure sample. Figure 4.21 demonstrates the top mass slope for reconstruction with pure sample after the mapping correction. Here, the mapping correction denotes to compensate fitted top mass bias. Main role of this mapping correction is to remove background effect from our top mass fit, and thus to correct top mass systematic shift. The mapping function expression is as follows

$$M_{Rec} = A_0 + A_1 \cdot M_{Input} \quad (4.48)$$

where M_{Rec} and M_{Input} are reconstructed top mass by using dilepton DLM and input top mass for generator, respectively. A_0 and A_1 are fit parameters. Once we apply this mapping function, we can obtain input top mass by using above mapping function, and the statistical error scaled up by the inverse number of slope (A_1) of the mapping function. We further discuss theses in the next section 4.4 and also in Appendix A.

²top signal includes 3 channels, i.e. dilepton, lepton + jets, all hadronic for difference of Ws decay.

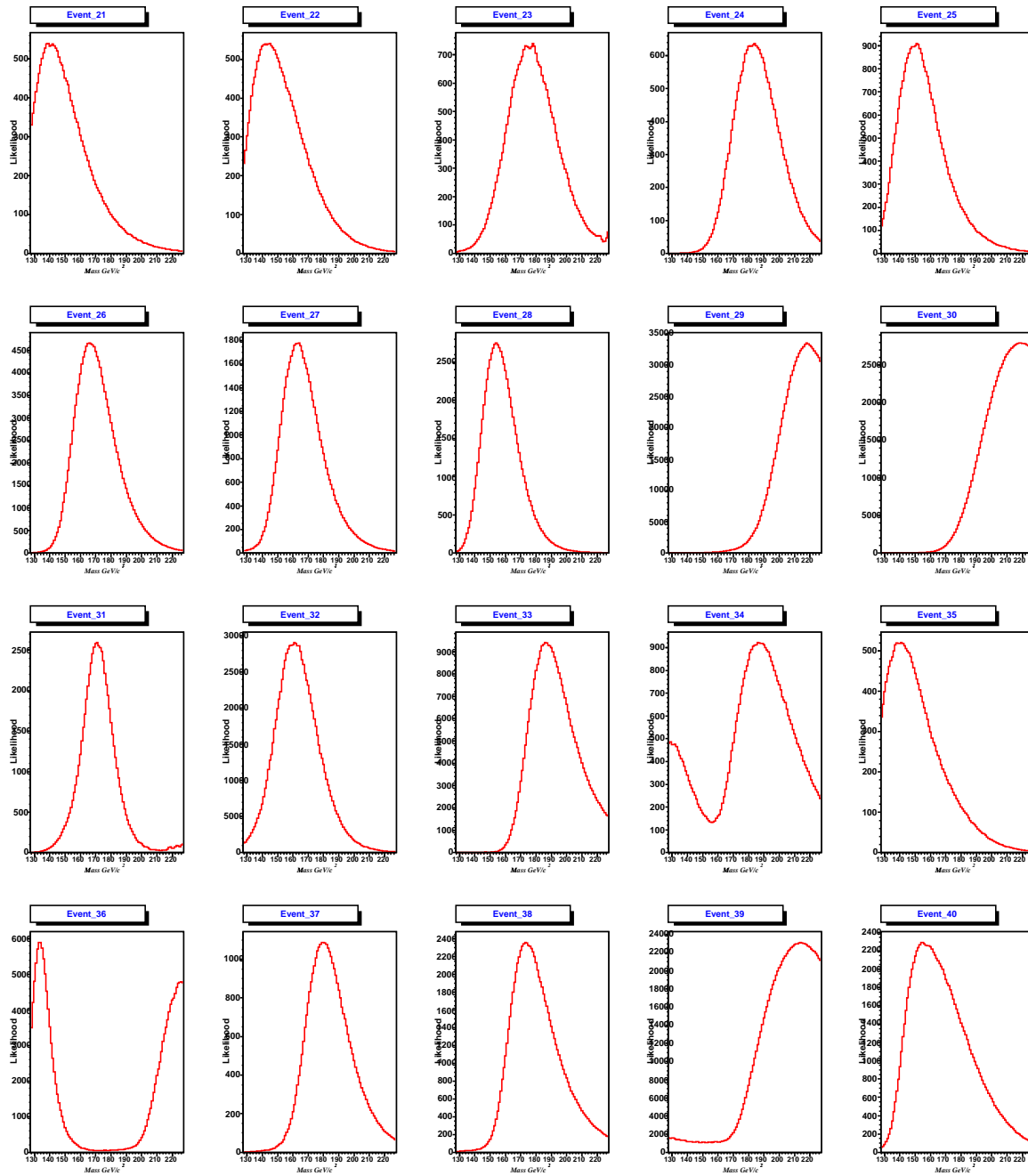


Figure 4.19: Examples of event likelihood distribution for top signal events.

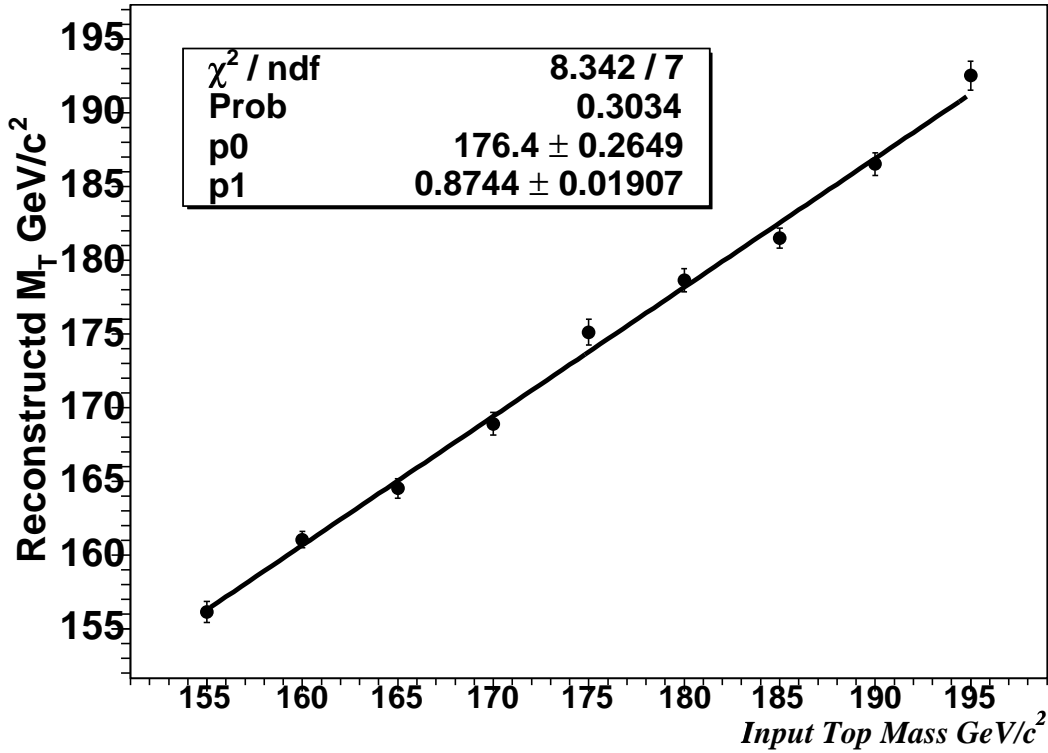


Figure 4.20: Reconstructed vs. input top mass for the pure sample. The straight line is the mapping function defined by Eq. (4.48).

4.3.2 Uncertainty of Likelihood

In this subsection, we specify the uncertainty of likelihood we calculated. Potentially, the likelihood itself doesn't have any uncertainty, but if we compute it with the use of finite MC integration, we need to further take account of the uncertainty from the numerical integration. We write down the averaged likelihood and its uncertainty in the i -th event at a certain mass as the following

$$\langle L \rangle^i = \frac{1}{N_{scan}} \sum_{k=1}^{N_{scan}} L_k^i \quad (4.49)$$

$$\delta L^i = \sqrt{\frac{\sum_k (L_k^i - \langle L \rangle^i)^2}{N_{scan}}} \quad (4.50)$$

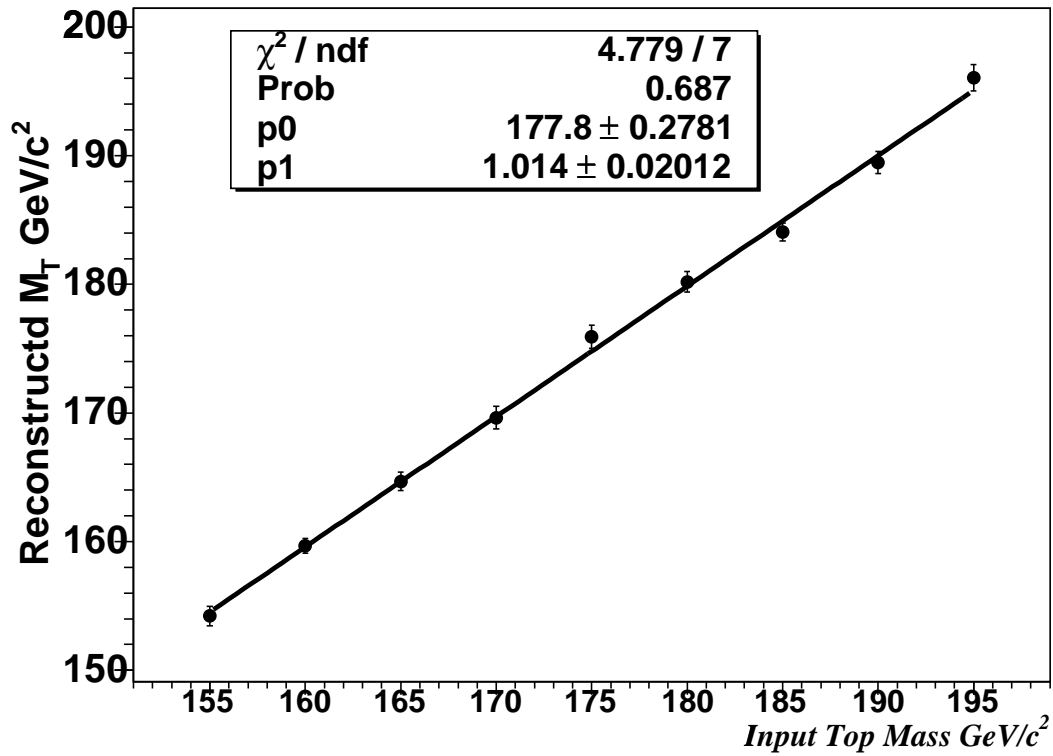


Figure 4.21: Reconstructed vs. input top masses after applying the mapping function. This result shows that the masses of pure samples are well reconstructed and corrected.

where, k is the number of the scanning of Monte Carlo integration at a certain mass. The likelihood L^i is multiplied event by event to obtain the joint likelihood. The uncertainty of the joint likelihood is obtained by the propagation of the uncertainty for each event. The fractional uncertainty of the joint likelihood is written as

$$\frac{\Delta L}{L} = \sqrt{\sum_{i=1}^{Nev} \left(\frac{\Delta \langle L \rangle^i}{\langle L \rangle} \right)^2} \quad (4.51)$$

Figure 4.22 shows examples of the event likelihood distributions and their fractional uncertainty of the likelihood.

When we extract a top quark mass, we apply the asymmetric quadratic fit to joint likelihood distribution. The fitting function is

$$f(x) = \begin{cases} p0 \cdot (p1 - M_t)^2 & (M_t > p1) \\ p3 \cdot (p1 - M_t)^2 & (M_t \leq p1) \end{cases} \quad (4.52)$$

where $p0$ and $p1$ indicate the statistical uncertainty and the reconstructed top mass from joint likelihood fit, respectively. As for fitting range of the above function, we take that gives the maximum fitting probability by changing the range in every pseudo experiment.

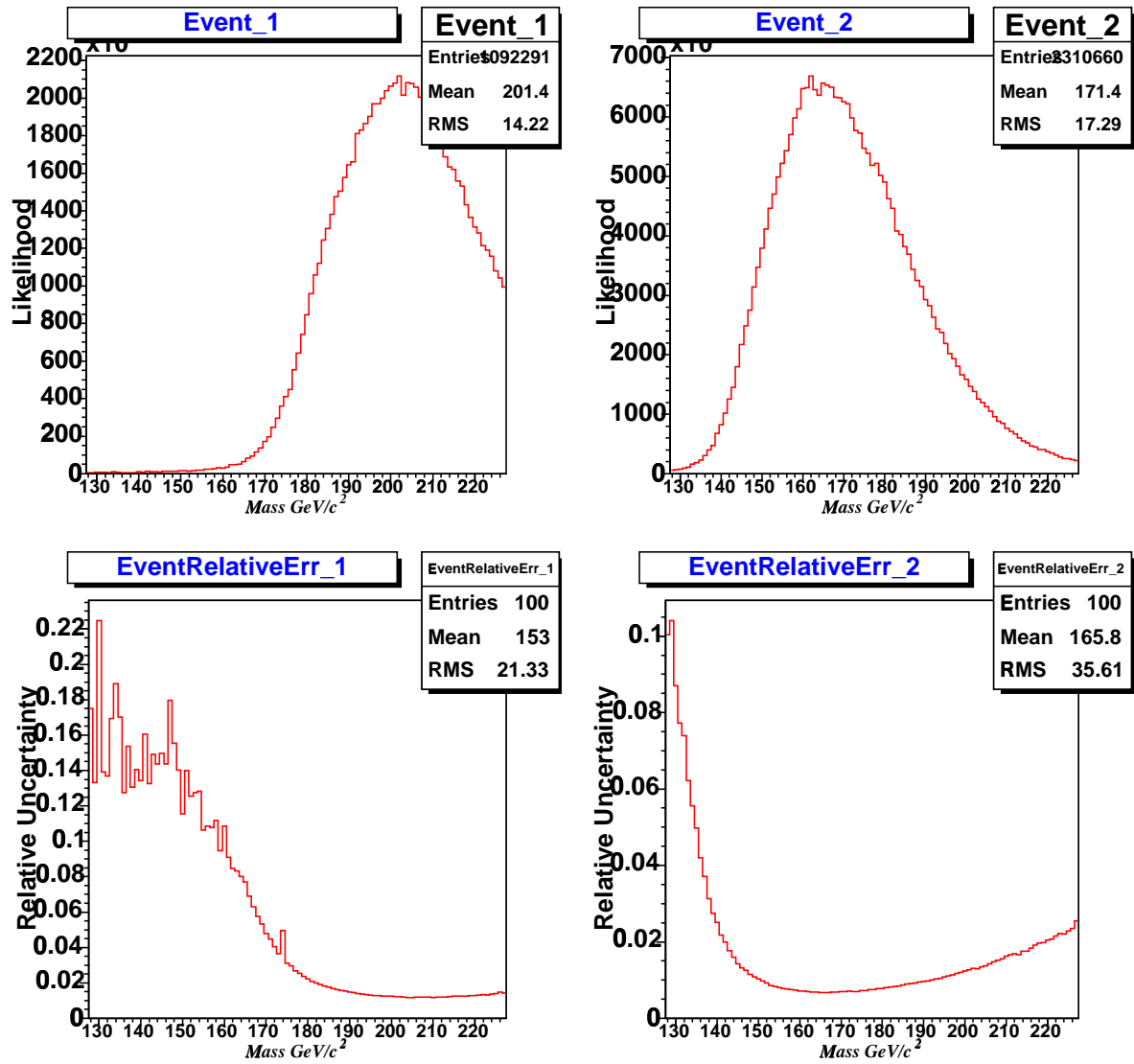


Figure 4.22: Top histograms show examples of event likelihood distributions. Bottom histogram indicate the relative uncertainty at the event corresponding to the top histograms.

4.4 Background Study

Chapters 3 and ?? represent top dilepton event selection and cross section measurement by using top dilepton events, and they describe sample composition including signal and some backgrounds. These give us the expectation numbers of signal and backgrounds in top quark mass measurement. In this section, by using their numbers and understanding we estimate reconstructed top quark mass with removal of background effects. Moreover, the expected statistical uncertainty of our measurement is established.

4.4.1 Additional Event Selection

First of all, we require additional cuts to improve the analysis quality after event reduction for dilepton event selection.

For some events, our likelihood calculation fails due to lack of the computing time. Those events which have the likelihood smooth with respect to the top mass are desirable. But even the signal sample does not always show the smooth curve ($\sim 1\%$). We consider two reasons for this. First, the integration time is not long enough, while in principle, completing MC integration requires infinite amount of time. There are other causes for the unsmooth likelihood curves, e.g. the virtual mass of the top (see Eq. (4.22)) is far from its pole mass, or the b jets are misidentified due to initial state or final state radiation. Thus we require as a cut the smoothness of the mass dependence of the likelihood function. The efficiency of this additional cut for events in various processes are shown in Table 4.1.

Sometimes events have undesired likelihood shape, especially in background events. In the low statistic pseudo-experiment test (See Appendix A), such events tend to give bumps outside the Gaussian shape of the pull distribution. Typical undesirable event such as Fig 4.23 makes bumps in joint likelihood distribution. Typical pull distribution in which we look unreasonable bump is shown in Fig 4.24. To avoid these behavior, we employ two processes. One is taking a naive undesirable event cut. The other is adding the pedestal to the likelihood curve.

As for the undesirable event cut, we define the cut parameter not to give bias to the top mass measurement. Searched top mass region is set as between 128 to 228 GeV/c^2 and top mass is scanned every 1 GeV/c^2 . Hence we calculate the likelihood at each mass point of 100 bins in an event. Here we define the N_{bin}^{pass} which means the numbers out of 100 bins to be able to pass the criterion for undesirable event cut. The criterion at each top mass bin is as follows.

$$L_{bin} > \frac{L_{max}}{1000} \quad (4.53)$$

where, suffix max means likelihood maximum value in an event. If the likelihood at a certain bin satisfies the requirement of Eq. (4.53), N_{bin}^{pass} can be counted with one. Then, if an event satisfies $N_{bin}^{pass} > 60$, such event pass the undesirable event cut. In Fig. 4.23, the line shows the

$10^{-3} \times L_{max}$. To keep the event, it is necessary to have more than 60 bins which have much likelihood greater than the line points.

As for adding pedestal, the definition of pedestal value L^p is

$$L^p = s^p \cdot L_{max} \quad (4.54)$$

where s^p is the pedestal factor. L_{max} stands for the likelihood value of maximum bin in an event. Here we employ 10^{-4} as the value of s^p . We empirically employ pedestal factor, to obtain the input mass by using mapping function. The pedestal could avoid to 0 likelihood with scanning top mass in an event. Sometimes, for background especially, the event have 0 likelihood bin for top mass, this is caused by the violation of the relation for Eq. (4.22) in the kinematics of an certain event. If 0 likelihood bin in the likelihood distribution of an event exists, joint likelihood of top mass can not be defined because multiplication is going to totally 0 at a certain bin. Therefore the help of the pedestal is necessary for multiplication of likelihood.

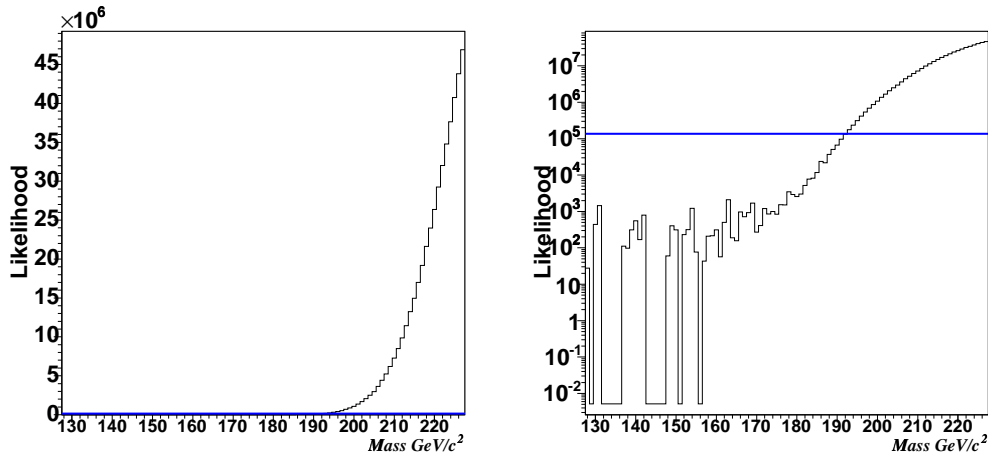


Figure 4.23: The typical pathological event. This event has big number of likelihood at high mass region and, on the contrary, has very small number or 0 likelihood at low mass region. Left plot shows the linear scale distribution, Right plot shows the log scale distribution. The line corresponds to $10^{-3} \times L_{max}$.

If we apply our additional cut, we can to check top mass bias. Figure 4.25 shows the efficiency of our additional cut which we introduced in this section. Any bias can not be seen so that we don't consider any care for that.

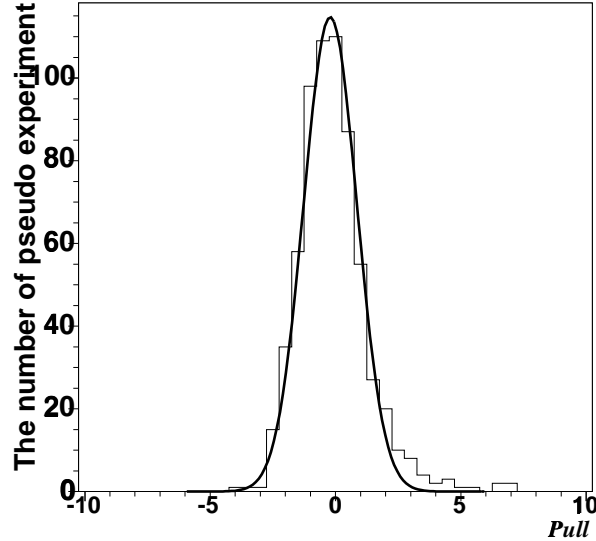


Figure 4.24: The typical pull distribution in which we could find unreasonable bump.

Source	# of events	(after DLM cut)	(after all cut)	ϵ_{cut}
WW	1.21 ± 0.24	1.13 ± 0.22	1.07 ± 0.21	$89.1 \pm 0.9\%$
WZ	0.42 ± 0.08	0.37 ± 0.07	0.36 ± 0.07	$86.1 \pm 1.0\%$
$DY \rightarrow ll$	4.60 ± 1.20	3.94 ± 1.03	3.58 ± 0.95	$76.9 \pm 4.7\%$
$DY \rightarrow \tau\tau$	0.80 ± 0.19	0.75 ± 0.18	0.69 ± 0.17	$85.8 \pm 3.5\%$
Fake	3.45 ± 1.38	3.21 ± 1.29	3.17 ± 1.28	$91.9 \pm 3.3\%$
Background	10.5 ± 1.6	9.4 ± 1.7	8.9 ± 1.6	$84.3 \pm 2.4\%$
$t\bar{t}$ (6.1pb)	15.7 ± 1.4	15.3 ± 1.2	15.3 ± 1.2	$97.4 \pm 0.2\%$
Bkg + Sig (6.1pb)	26.3 ± 2.3	24.7 ± 2.1	24.1 ± 2.0	$92.1 \pm 1.0\%$
Bkg + Sig (8.8pb)	33 ± 2.6	31.4 ± 2.5	30.8 ± 2.4	$93.2 \pm 0.8\%$
Run II DATA	33	32	32	

Table 4.1: Numbers for expected sample compositions after the event selection and the additional cuts. The number of expected $t\bar{t}$ events in the $t\bar{t}$ row is obtained by assuming $\sigma_{t\bar{t}} = 6.1\text{pb}$ and $M_t = 175 \text{ GeV}/c^2$. The $t\bar{t}$ total cross section of 8.8pb corresponds to the latest cross section measurement with CDF Run II 33 top dilepton candidates. The last column indicates our additional cut efficiency for likelihood calculation fails and undesirable event cuts. First column shows the numbers of event pre cut, i.e. the number after dilepton event selection.

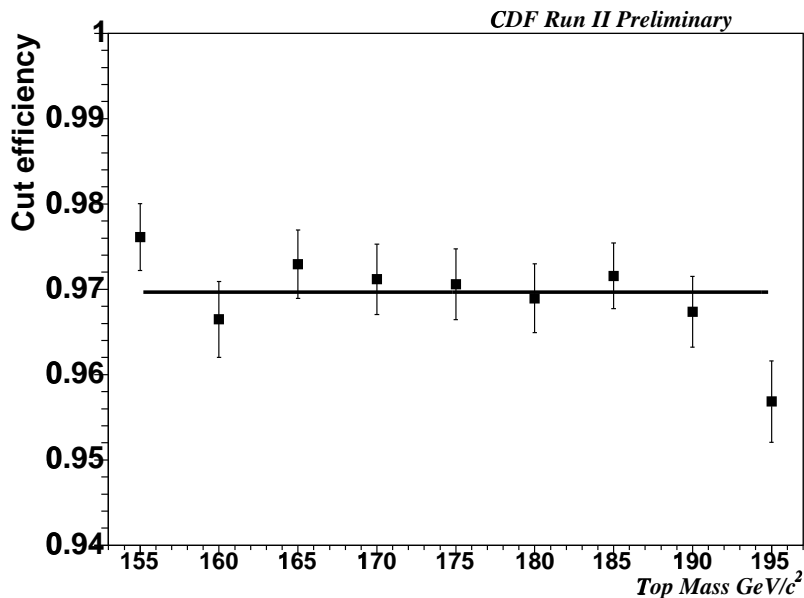


Figure 4.25: Additional cut efficiency as a function of input top mass.

4.4.2 Pseudo Experiment Test

In this subsection, we represent performance of the pseudo-experiment (PE) with samples containing all background processes. The further argument of pseudo experiment can be seen in Appendix A. Assuming the $t\bar{t}$ cross section of 6.1 pb, we generate the PE set by Poisson statistics with the mean values of 15.66 signal and 10.5 background events (see Table 4.1).

In order to reconstruct input top mass by using signal and background combined sample, we need to construct mapping function Eq. (4.48). Here we make two mapping functions to reconstruct different sample compositions. They are in order to make PE test for $\sigma_{t\bar{t}} = 6.1$ pb and for 32 events in data (See Table 4.1). Figure 4.26 shows the reconstructed mass as a function of its input mass with various background fractions. The background fraction is changed from 0% to 50% with the use of sample composition for 32 events in data. By our estimate, the fraction of the background in data is 27.8% after all event selection and our additional cuts. The fraction dependence of slopes and constant value of linear mapping fits are shown in Fig 4.27.

To validate the mapping function performance, we look into some checks after mapping correction. Figures 4.28 and 4.29 show the sanity check, residual check, the pull mean and the pull width as a function of input top mass with the use of sample composition for $\sigma_{t\bar{t}} = 6.1$ pb and for 32 events in data after mapping correction. The slope of sanity check resemble 1.0, fitted residual top mass and fitted pull mean resemble 0 in the good correction. Furthermore,

we find fitted pull width as 1.392 for $\sigma_{t\bar{t}} = 6.1$ pb and as 1.323 for 32 events in data. These numbers are so called “pull width calibration constant”, to calibrate statistic uncertainty due to accurately estimation. With their constant value, we scale up statistic uncertainty. In this thesis, we call its procedure as “calibration”.

After this calibration, we obtain good agreement of reasonable pull width as shown in Fig. 4.30.

Lastly, we obtain the expected statistical uncertainty in case of the use of sample composition for $\sigma_{t\bar{t}} = 6.1$ pb and for 32 events in data. The expected statistical uncertainties for $\sigma_{t\bar{t}} = 6.1$ pb are shown in Fig. 4.31. Comparison of data and MC expectation is put in the next section (See Fig. 5.4). The estimated statistical uncertainties are $+10.97 - 9.66$ GeV/ c^2 and $+7.97 - 7.08$ GeV/ c^2 respectively.

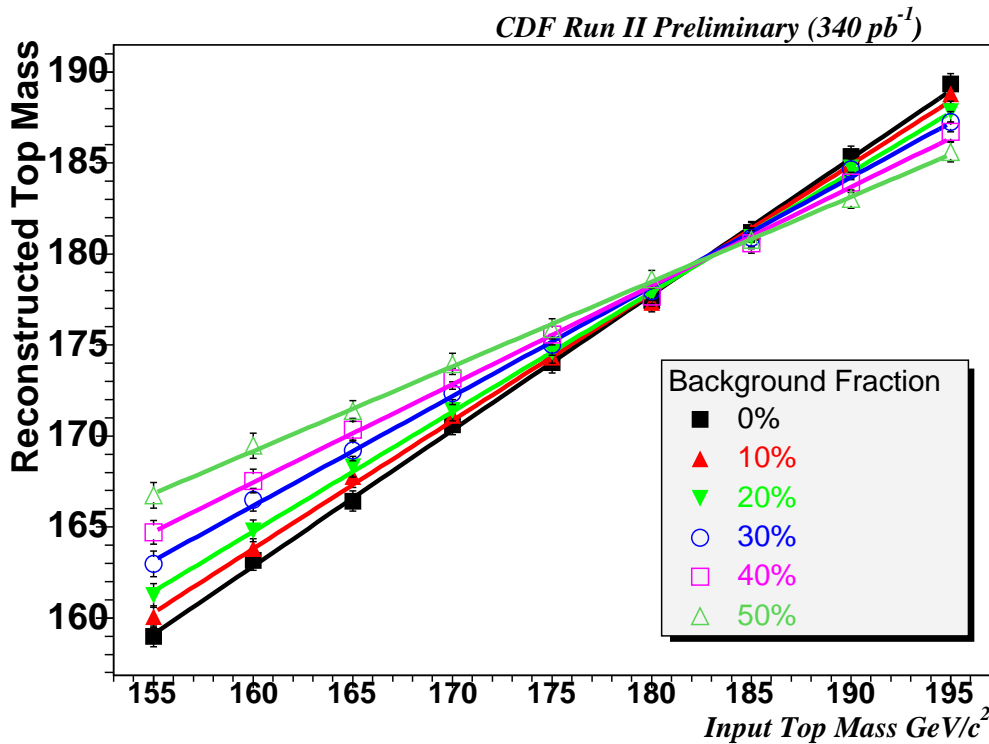


Figure 4.26: The reconstructed top mass as a function of its input mass with various background fractions. The background fraction is changed from 0% to 50% with the use of sample composition for 32 events in data.

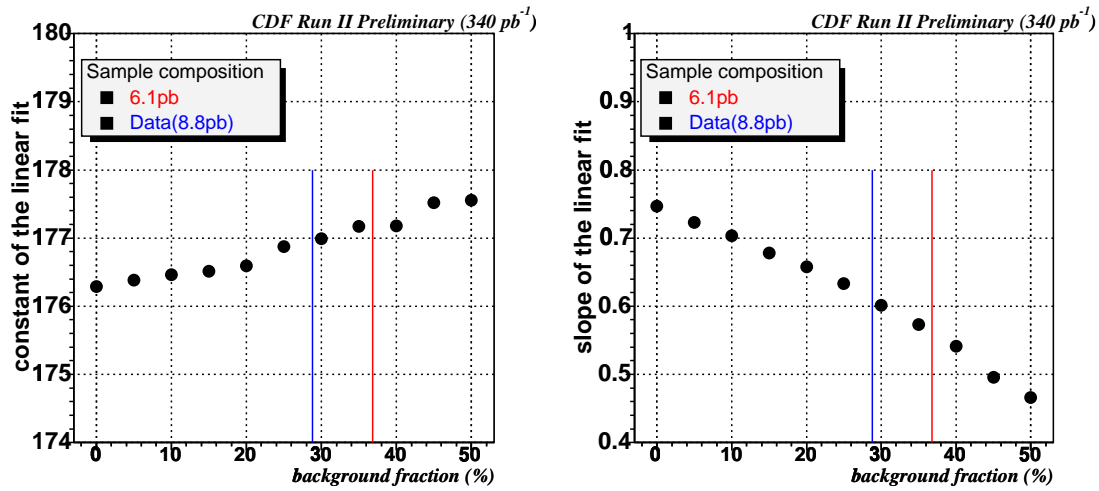


Figure 4.27: The fraction dependence of slopes and constant value of mapping linear fits.

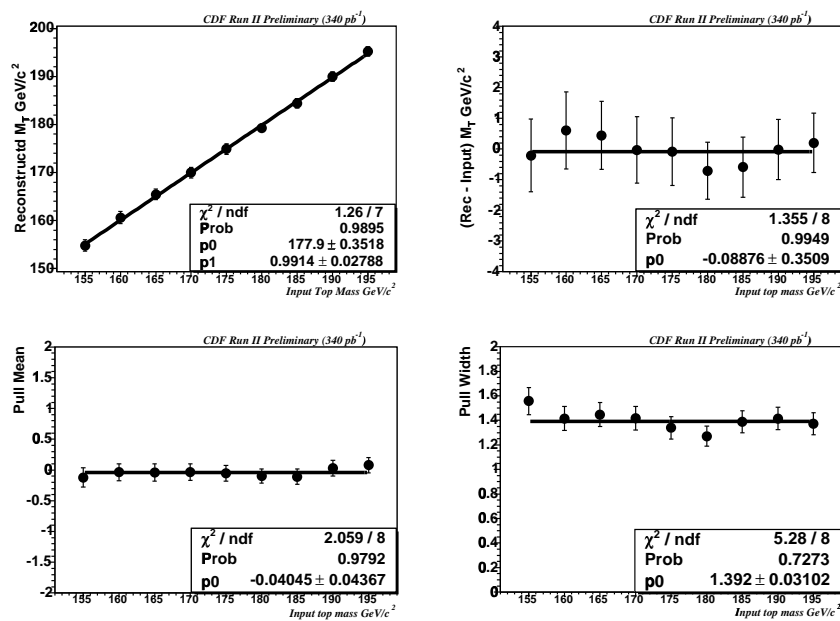


Figure 4.28: The sanity check, residual check, pull mean and pull width after applying mapping function. The sample composition is case of assumption of 6.1pb top cross section.

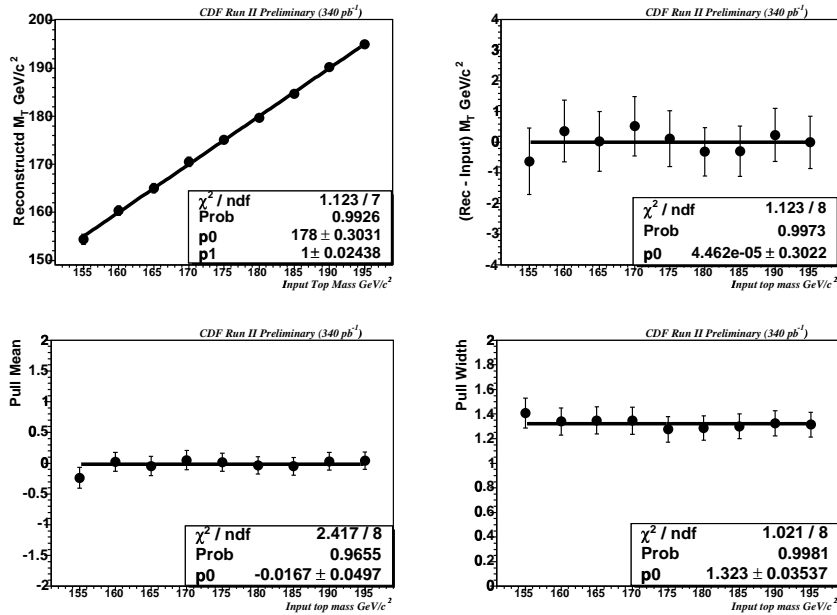


Figure 4.29: The sanity check, residual check, pull mean and pull width after applying mapping function. The sample composition is case of data.

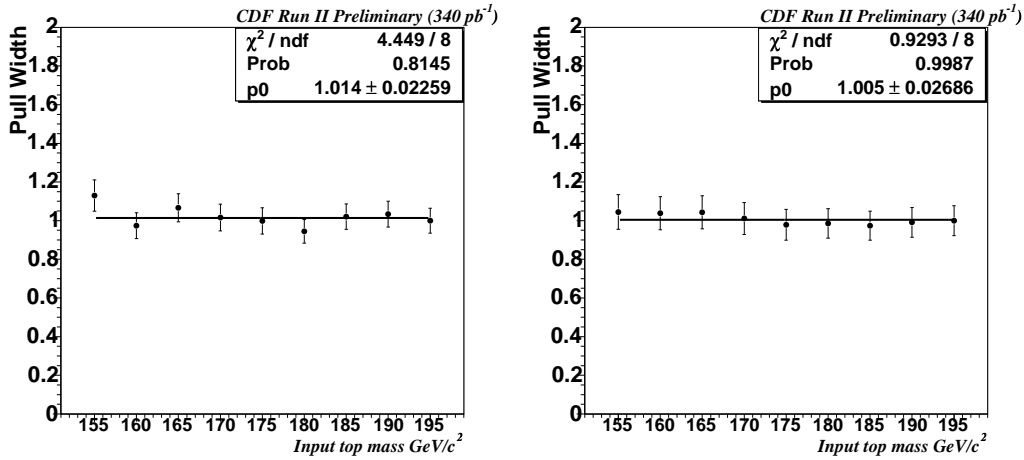


Figure 4.30: The left plot shows the pull width for input top mass after the calibration in case of the assumption of 6.1pb top cross section. The right plot shows the pull width for input top mass after the calibration in case of data.

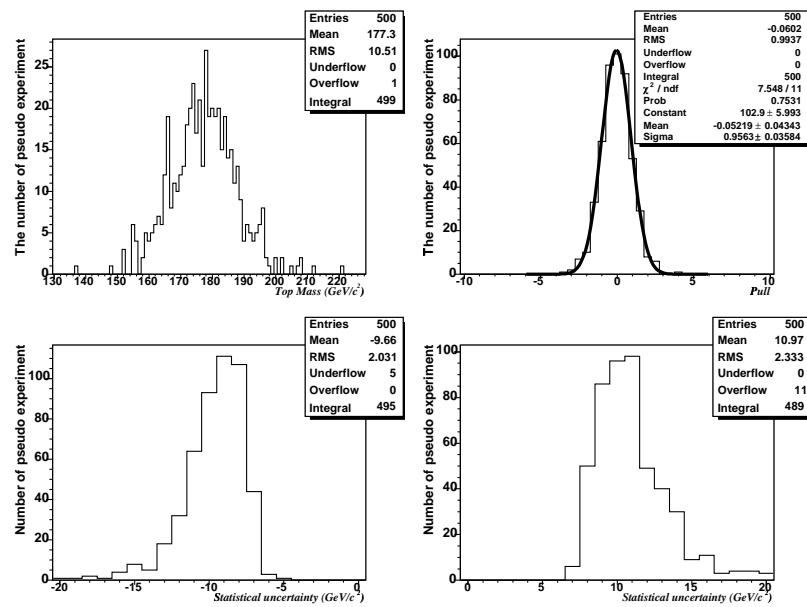


Figure 4.31: These are the results of pseudo experiment in case of 6.1pb top cross section assumption after mapping and calibration. Top left shows the top mass histogram, Top right shows the pull distribution in performing 500 pseudo experiment test, bottom two plots show the expected statistical uncertainties.

Chapter 5

Results

5.1 Data

We obtain 33 $t\bar{t}$ dilepton candidates with dilepton event selection by using CDF Run II data of $\int L dt = 340.5 \text{pb}^{-1}$. These events are identical to what CDF dilepton cross section measurement currently provides [50].

5.1.1 Latest result of cross section in dilepton channel

Figure 5.1 shows the background and signal composition of the “dil” events¹ vs jet multiplicity after dilepton event selection except for H_T and opposite charged cut have been applied. A good agreement can be seen in the control region of 0 and 1 jet bin. With 33 $t\bar{t}$ dilepton candidates, we calculate a top cross section of

$$\sigma_{t\bar{t}} = 8.79 \pm 2.24(\text{stat.}) \pm 1.02(\text{sys.}) \pm 0.53(\text{lumi})\text{pb}$$

5.1.2 Result of Top Mass Determination

Using 33 candidate events, we apply our additional cut and obtain the final number in Table 4.1. DLM calculation fails in one event out of 33 dilepton candidates. Thereby we use residual 32 events in top quark mass calculation by DLM.

At the end, the final numbers of background expectation can be 8.88, and thus the expected background fraction in data is 27.8%. We extract the top quark mass from the joint likelihood distribution of 32 dilepton candidates by fitting it with asymmetric quadratic function.

$$M_t = 169.95^{+3.37}_{-3.12}(\text{stat.}) \text{ GeV}/c^2$$

¹ dil events means dilepton candidate event with the use of CDF standard dilepton event selection.

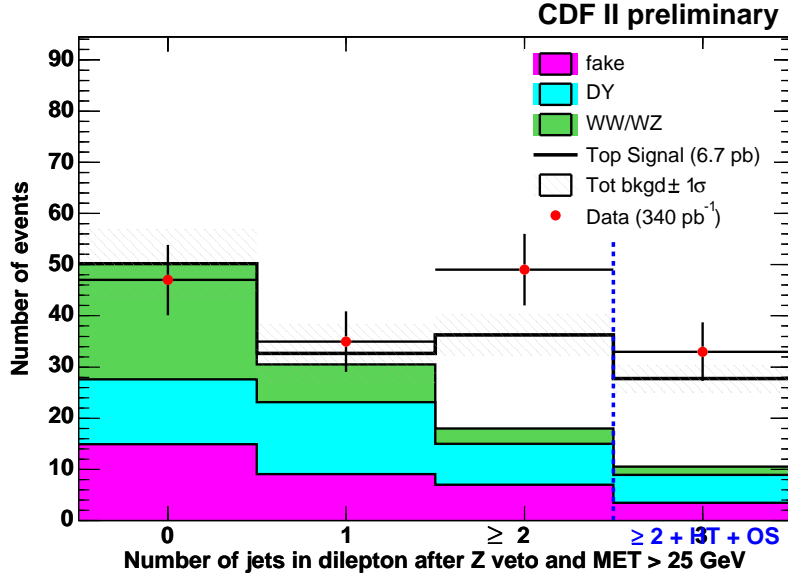


Figure 5.1: Background and signal composition of the dilepton events vs jet multiplicity after dilepton event selection except for H_T and opposite charged cut have been applied.

Figure 5.2 shows the final fit to determine top quark mass. Thereby we apply the mapping function for data. We correct mean value of top quark mass by using mapping constant A_0 and mapping slope A_1 and thus scale up the statistic uncertainty with mapping slope A_1 (See Eq. (4.48)).

$$M_t = 166.61^{+5.51}_{-5.10}(\text{stat.}) \text{ GeV}/c^2$$

Finally, pull width can be calibrated with 1.323 as we discussed in sub-section 4.4.2. Thereby, we determine the top quark mass by using CDF Run II top dilepton candidates of $\int L dt = 340.5 \text{ pb}^{-1}$ by using top dilepton channel.

$$M_t = 166.6^{+7.3}_{-6.7}(\text{stat.}) \text{ GeV}/c^2$$

The attached uncertainty is only statistics. The next Chapter 6 evaluates systematic uncertainty in addition. Figure 5.3 shows the Maximum Likelihood Mass Comparison. As a cross check between MC expectation and CDF data for Dynamical Likelihood calculation, we considered maximum likelihood mass. Maximum likelihood mass at event likelihood distribution as like as Fig 4.19 is extracted for each MC signal, background source and 32 data candidates.

This comparison can be considered as one of the validations for this method. Here we assumed $M_t = 165 \text{ GeV}/c^2$ for signal Monte Carlo.

Figure 5.4 shows the expected statistical uncertainty in case of data. Red line indicates statistical errors obtained from the data. This is the second cross check between MC expectation and CDF data for Dynamical Likelihood calculation.

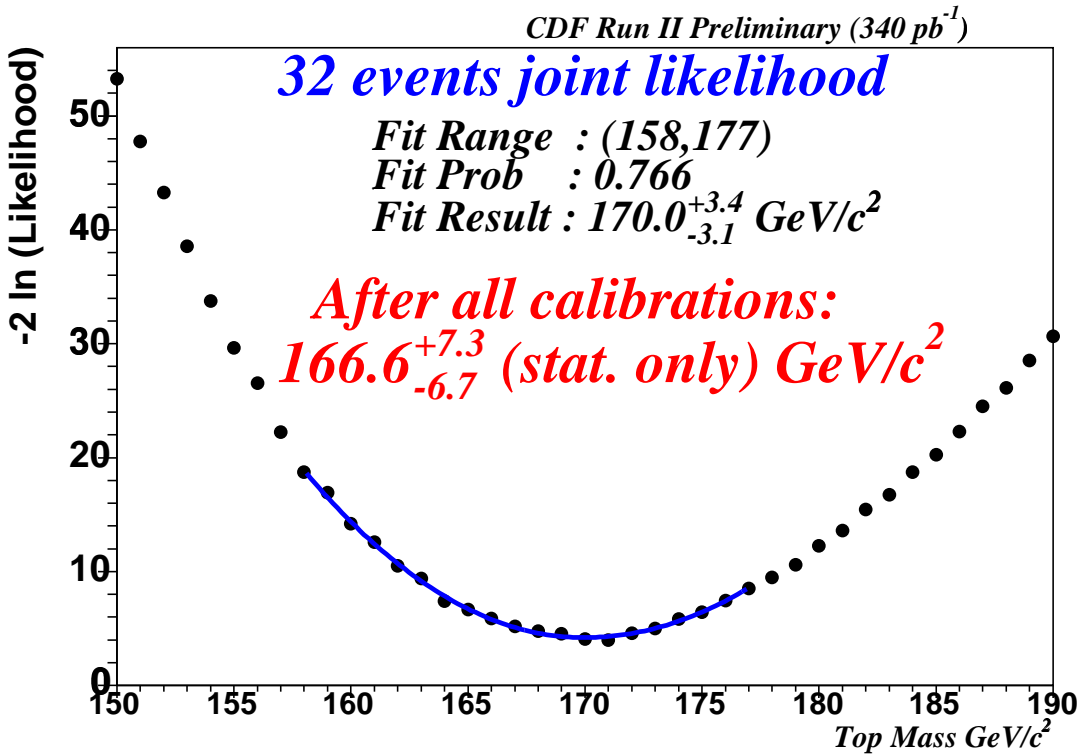


Figure 5.2: The joint natural negative log likelihood distributions of 32 events. Asymmetric quadratic fit gives $M_t = 169.95^{+3.37}_{-3.12}(\text{stat.}) \text{ GeV}/c^2$

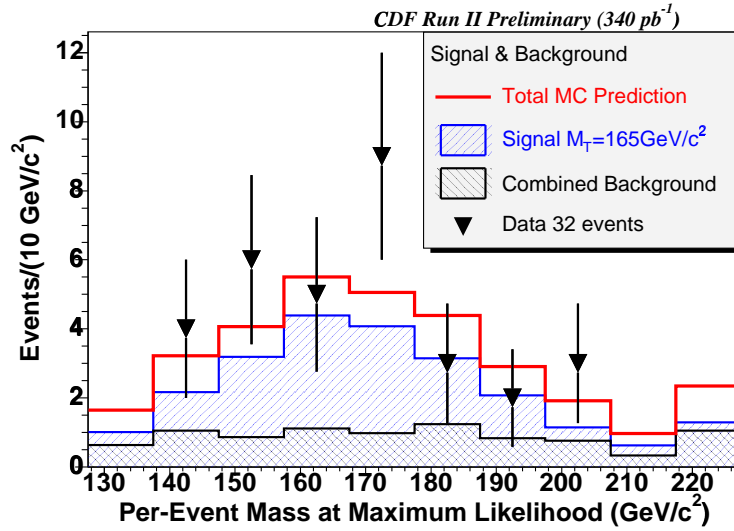


Figure 5.3: Maximum likelihood mass distribution for MC expectation and data. Normalization of MC expectation histogram is consistent with 32 data candidates.

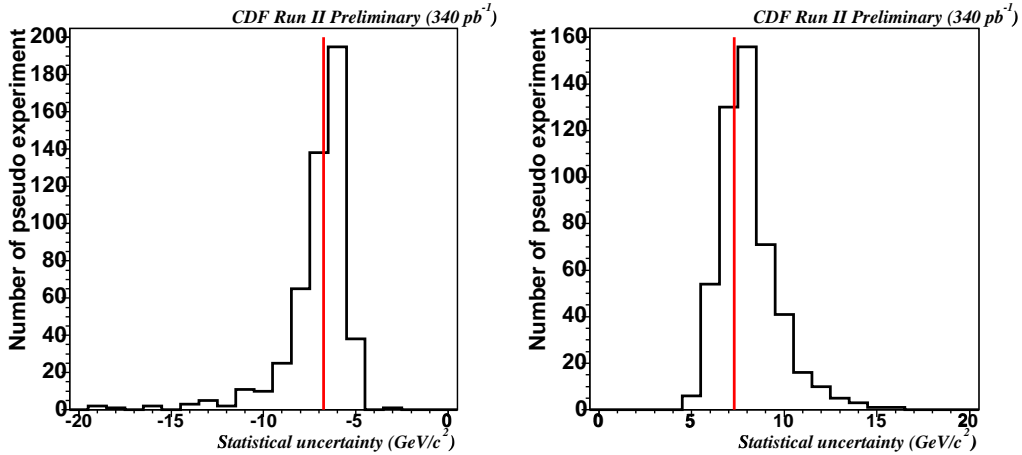


Figure 5.4: The expected statistical uncertainty in case of data cross section assumption. Red line indicates statistical errors from data.

Chapter 6

Systematic Uncertainties

6.1 Systematic Uncertainty

Our study is based on many assumptions coming from Monte Carlo simulation in modeling the data. Therefore we need to estimate the systematic uncertainties due to accurate estimation. If perfect Monte Carlo generation and perfect detector simulation would be given, this method had no systematic errors. Of course, such condition does not exist. There are differences between CDF data and our Monte Carlo description both of physical processes and of our detector in actual. The motivation of this section is to understand their effect and evaluate the systematic uncertainty of top quark mass measurement. To extract the systematic uncertainties, we perform 32 event PE test with signal and background sample. All systematics are calculated for $M_t = 178$ GeV/ c^2 except for Jet Energy Scale systematics due to limit of producing MC sample.

6.1.1 Jet Energy Scale

There are significant uncertainties on many aspects of our measurement of jet energies. Some of these are in the form of uncertainties on our energy measurements themselves; some are uncertainties on our detector simulation, which is used to derive many corrections, and ultimately to extract the top mass; still others are best understood as uncertainties on jet production and fragmentation models used in the generators. In practice, we define systematics on the jet energies corresponding to some levels of generic jet corrections as described in sub-section 3.1.3. For each shift, signal and background reconstructed mass distributions are generated using “dil” event selection and our additional cuts. The number of events of each pseudo experiment, and the background constraint, is the same as in the data candidate events. To obtain the uncertainty of jet energy scale, we shift it by $\pm 1\sigma$ for both of signal and background samples, and take a half of difference between mass values of $+\sigma$ and $-\sigma$. Table 6.1 shows the results.

Description	+1 σ GeV/ c^2	-1 σ GeV/ c^2	systematics GeV/ c^2
η dependence	178.8	177.0	0.9
Multiple Interactions	177.7	177.5	0.1
Absolute Scale	179.6	175.9	1.9
Underlying Event	178.4	178.3	0.1
Out of Cone	179.5	175.9	1.8
Splash Out	178.2	177.9	0.1
Sum of the Above			2.8
Total ($M_t = 178$ GeV/ c^2)	180.9	175.4	2.7
Total ($M_t = 165$ GeV/ c^2)	168.4	163.3	2.6

Table 6.1: The jet systematic uncertainty at each individual level of the generic jet energy corrections. Total means the output of “TotalSys” function in CDF jet correction offline tool. The value of systematics is to take a half of difference between mass values of $+\sigma$ and $-\sigma$.

The uncertainty is estimated to be 2.8 GeV/ c^2 in assumption of $M_t = 178$ GeV/ c^2 to take a quadratic sum of each jet systematic source. As previous Chapter 5 shows, our final top mass fit results in $M_t = 165$ GeV/ c^2 and we need to check the systematic uncertainty in the MC assumption of $M_t = 165$ GeV/ c^2 . It is estimated to be 2.6 GeV/ c^2 totally, so we assign it as a Jet Energy Scale systematic uncertainty.

6.1.2 B Jet Energy Scale

B jet energy scale uncertainty needs further consideration against generic Jet Energy Scale. CDF generic jet correction which is described in sub-section 3.1.3 represents generic jet i.e. Initial/Final state radiations and W jets. On the contrary, top dilepton signature deals with two b jets from top quark decay. Namely we have to identify the differences between b jet and CDF generic jet as follows.

1. **Heavy quark fragmentation** : The b hadron resulting from the b quark fragmentation carries a larger fraction of the parent quark momentum than for light quark fragmentation. This is because b quarks are much heavier and thus only slightly decelerated when combined with a light quark to form a b hadron.
2. **Color flow** : W daughter jets come from the decay of a color singlet, while b jets have a color connection with the initial state partons inside the protons.
3. **Decay**: A large fraction of the decay products of b or c hadrons are charged leptons and neutrinos from semi-leptonic decays. These particles interact very differently with

the calorimeter than more common hadronic particles. Therefore, b jets have a different response on average from W daughter jets because of the larger semi-leptonic decay fraction. These decays are modeled by the MC that is used to extract the top specific energy corrections, but the uncertainty arising from the limited precision of the measurements of semi-inclusive leptonic branching fractions has to be taken into account.

Further study of these b jet systematics is reported a [51]. This indicates a total uncertainty of $0.6 \text{ GeV}/c^2$ on the top quark mass due to the specialties of b jets. There is no significant difference between our top mass analysis and theirs, so we simply quote it as a B Jet Energy Scale systematic uncertainty.

6.1.3 Parton Distribution Functions (PDFs)

Monte Carlo Generator can choose various PDFs to approach to actual experiment configuration. We use PDFs in our likelihood calculation and changing the PDF switches the size of Initial State Radiation (ISR). Therefore we need to establish the uncertainty coming from PDFs ambiguity. To do this, we have various PDFs assumption of MC.

1. **CTEQ5L** : This is our default set of PDF [52].
2. **MRST72** : A leading order PDF using more or less the same data as our default but fitted by a different group. No significant difference is expected relative to the default, but if a difference is found, it should be taken as a systematics.
3. **MRST75** : Same as the previous one, but using a different value of α_s , corresponding to $\Lambda_{QCD} = 300 \text{ MeV}$ vs $\Lambda_{QCD} = 228 \text{ MeV}$ for the previous. The difference between these two PDFs is taken as a systematics.
4. **CTEQ6M** : This is the next to leading order PDF from the CTEQ group [53]. The possible variations are separated into contributions from 20 independent eigen vectors. Each eigen vector has “ $+1\sigma$ ” and a “ -1σ ” set, thereby we change 40 eigen vector sets.

The result of eigen vector changes is plotted in Fig. 6.1. The sum in quadrature of a half of the difference between $+1$ and -1σ shift of the CTEQ6M eigen vectors is $0.3 \text{ GeV}/c^2$

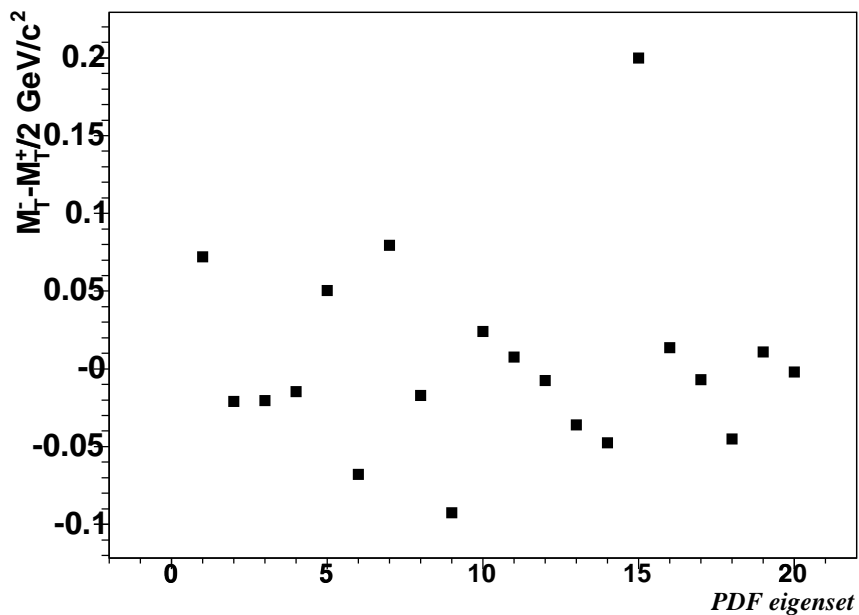
Other results are all listed in Table 6.2. We take a $0.4 \text{ GeV}/c^2$ as the PDFs systematic uncertainty.

6.1.4 Initial and Final State Radiations

In our analysis, transfer function include the ambiguity how the initial and the final state radiations behave. Thereby we prepared MC samples to be tuned PYTHIA parameter. To obtain the systematic uncertainty, we use PYTHIA MC samples which have two variations of

Source	ΔM_t GeV/ c^2
eigen vectors	0.3
MRST72 – CTEQ5L (check)	0.4
MRST75 – MRST72	0.2
Total	0.4

Table 6.2: The PDF systematic uncertainty.

Figure 6.1: The difference of extracted top mass between the positive and negative eigen vectors set. The quadrature sum to all of the difference is 0.3 GeV/ c^2 .

less or more ISR and FSR radiation. Results of applying tuned samples can be found in Table 6.3. We take $0.5 \text{ GeV}/c^2$ which is quadratic sum of ISR and FSR statistical errors as a systematic error due to 0 consistent in statistic.

Source	$M_t \text{ GeV}/c^2$
ISR less	177.5 ± 0.5
ISR more	177.7 ± 0.5
Difference/2	0.1 ± 0.3
FSR less	177.0 ± 0.8
FSR more	177.7 ± 0.5
Difference/2	0.4 ± 0.4

Table 6.3: The systematic uncertainty of the initial and final state radiation.

6.1.5 Generators

We estimate the systematic effect due to possible problems in the way our generator models its physical processes by comparing the PYTHIA and HERWIG generators. We compare two different Monte Carlo found in Table 6.4, and take $0.6 \text{ GeV}/c^2$ as a systematic error due to 0 consistent in statistic.

Source	$M_t \text{ GeV}/c^2$
PYTHIA	177.6 ± 0.4
HERWIG	177.8 ± 0.4
Difference	-0.2 ± 0.6

Table 6.4: The systematic uncertainty of Monte Carlo generators.

6.1.6 Background fraction

We employ mapping function to reconstruct input top quark mass and pull width scale factor to calibrate the statistical uncertainty due to accurately estimation. This two calibration factors would have an impact on final statistical uncertainty to change the background fraction ambiguity. Using the numbers in Table 4.1, we identify background fraction of $\pm 5\%$ (background fraction = $8.88/32$, Δ background fraction = $1.6/32$). If we consider $\pm 5\%$ background fraction uncertainty, this gives $0.6 \text{ GeV}/c^2$ top mass shift since mapping function slope is changed. Furthermore, according to the number of linear fit in Fig. 6.2, $\pm 5\%$ background fraction corresponds to ± 0.025 fluctuation of pull width. The ± 0.025 fluctuation of pull width gives 0.18

GeV/ c^2 top mass shift. Both of two systematic top mass shifts are 100% correlated with each other, so totally we assign 0.8 GeV/ c^2 as a background fraction systematic uncertainty.

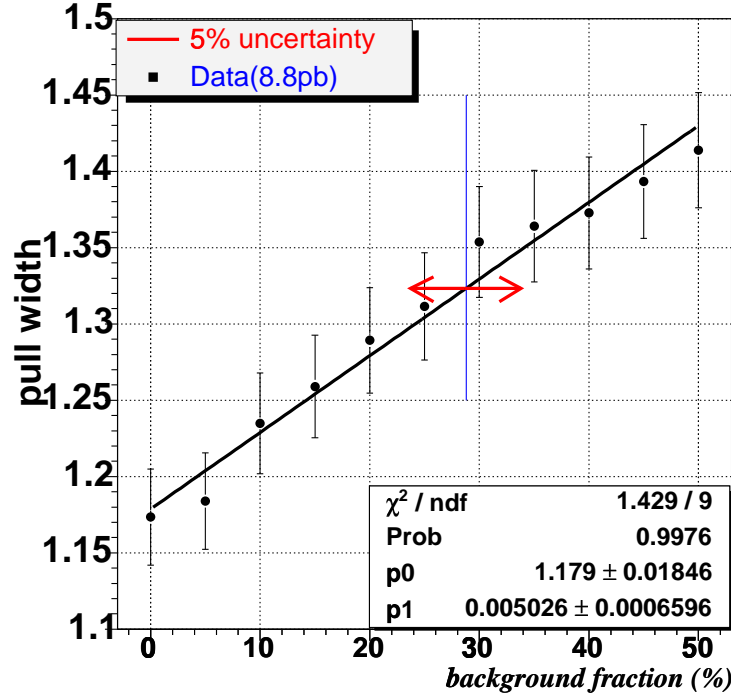


Figure 6.2: Pull width as a function of background fraction. Red arrows indicate $\pm 5\%$ background fraction error. The fitted parameter value of p1 gives ± 0.025 fluctuation of pull width calibration.

6.1.7 Background Modeling

Drell-Yan and Fake Background have complexed modeling for their matrix elements, and also they have large numbers as one of the backgrounds. Therefore we consider their background modeling systematics. The technique of this estimation has been discussed in CDF group [54].

Drell-Yan :

Drell-Yan production is difficult to model well, as it has a large cross section and a small acceptance. Since there is no real missing energy due to escaping neutrinos, there is a small probability to pass the missing energy requirement. Therefore we consider the events having high missing energy might have big impact on its modeling. The agreement of the tail on the missing energy distribution between data and MC expectation is well understand, and so we

employ the number of data events on the tails to look at the effect of Drell-Yan modeling.

To gauge our sensitivity to events on the tails of the distribution, we vary the composition of our pseudo experiments by both enhancing events and suppressing on the tails and deweighting events. We assign a weight to each event as

$$\begin{aligned} w_+ &= 1 + \frac{1}{\sqrt{n_+}} \\ w_0 &= 1 \\ w_- &= 1 - \frac{1}{\sqrt{n_+}} \end{aligned} \tag{6.1}$$

where n_+ represents the number of events further out on the tail of the missing energy distribution than the given event. The event with the largest missing energy will receive weights ($w_+ = 2, w_0 = 1, w_- = 0$). This enhances or suppresses the tail events.

Weights	M_t GeV/ c^2
w_+	177.7
w_0	177.8
w_-	177.5

Table 6.5: The results of reconstruction for enhanced Drell-Yan events.

Fake :

The fake background is very difficult to model well in the simulation, as it is sensitive to the smallest details of the detector performance. To avoid issues of modeling, the events which model this background are drawn from the data itself; the events are selected with a looser requirement on one of the leptons in order to accumulate a sample of fake candidates, and then weighted by the probability that the loose lepton would pass lepton identification requirements. These weights are calculated as a function of the P_T and isolation of the fake candidate, and each candidate has its own weight and errors.

To gauge our sensitivity to the calculation of the fake rates, we vary the fake rates in two ways. First (a), we enhance those events with large fake rate, to exaggerate their effect; second (b), we enhance events with small fake rate, to exaggerate their effect:

We assign a weight to each Fake candidate as following on Table 6.6

where δw means the error of fake probability from dilepton fake study. The results of pseudo experiment can be found on Table 6.7:

We take $0.2 \text{ GeV}/c^2$ of the half of difference between w_+ and w_- as the Drell-Yan Background Modeling error, take $0.2 \text{ GeV}/c^2$ of the difference between w_a and w_b as the Fake Background Modeling error. In quadrature sum of them, total Background Modeling error is $0.3 \text{ GeV}/c^2$.

Weights	$w > \bar{w}$	$w < \bar{w}$
w_a	$w \rightarrow w + \delta w$	$w \rightarrow w - \delta w$
w_0	$w \rightarrow w$	$w \rightarrow w$
w_b	$w \rightarrow w - \delta w$	$w \rightarrow w + \delta w$

Table 6.6: The definition of weights for fake candidate event

Weights	M_t GeV/ c^2
w_a	178.1
w_0	178.2
w_b	178.3

Table 6.7: The results of reconstruction for enhanced Fake candidate events.

6.1.8 Background Monte Carlo statistics

We generated large amount of signal MC samples but not for backgrounds. We need to rely on background MC samples to construct mapping function and calibrate pull width and so on. Hence we have to understand the uncertainty of Monte Carlo statistics we generated.

We employ the way to split current samples to two pairs, and measure M_t from an ensemble of pseudo experiments using each exclusive set. We consider the difference between these two measurements. We repeat this procedure 40 times. The difference of top mass is filled in as can be seen Figs 6.3 - 6.7. We take the root mean square of the distribution as an estimate of the statistical uncertainty associated with using each sample half the size when we perform the way of our usual pseudo experiments. So, we divide the root mean square by $\sqrt{2}$. Lastly we take 1.3 GeV/ c^2 in quadrature of five background sources as shown in Table 6.8 as a systematic uncertainty of Background Monte Carlo statistics.

Source	ΔM_t GeV/ c^2
WW	0.17
WZ	0.07
Drell Yan	0.77
$Z \rightarrow \tau\tau$	0.18
Fake	1.07
Total	1.34

Table 6.8: The summary of systematic uncertainty of MC Background statistics.

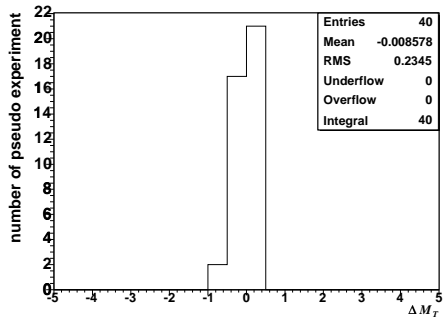


Figure 6.3: The difference of Top mass, when we perform pseudo experiment at 40 times with splitting WW background sample into 2 samples.

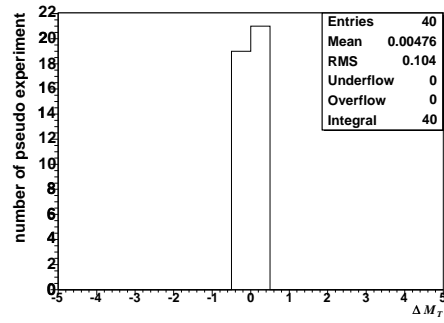


Figure 6.4: The difference of Top mass, when we perform pseudo experiment at 40 times with splitting WZ background sample into 2 samples.

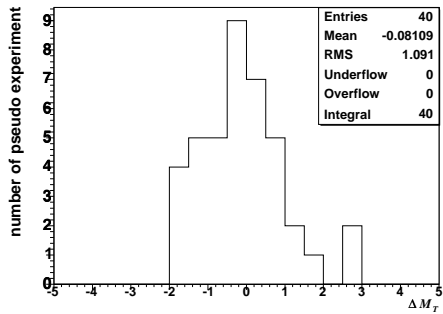


Figure 6.5: The difference of Top mass, when we perform pseudo experiment at 40 times with splitting Drell Yan background sample into 2 samples.

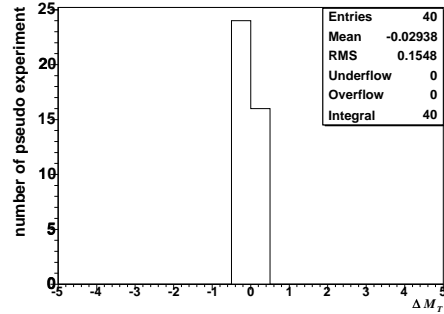


Figure 6.6: The difference of Top mass, when we perform pseudo experiment at 40 times with splitting $Z \rightarrow \tau\tau$ background sample into 2 samples.

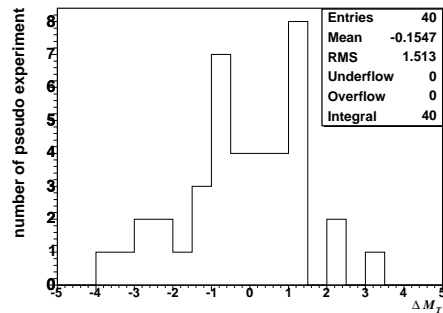


Figure 6.7: The difference of Top mass, when we perform pseudo experiment at 40 times with splitting Fake background sample into 2 samples.

6.1.9 Summary of Systematics

The systematic uncertainties are summarized in Table 6.9. The total systematic uncertainty is estimated to be $3.2 \text{ GeV}/c^2$.

Source	$\Delta M_t \text{ GeV}/c^2$
Jet Energy Scale	2.6
B Jet Energy Scale	0.6
PDFs	0.4
ISR & FSR	0.5
Generator	0.6
Background fraction	0.8
Background Modeling	0.3
Background MC Statistic	1.3
Total	3.2

Table 6.9: The summary of systematic uncertainty.

Chapter 7

Other Checks

7.1 Other Checks

This section explains some checks associated with our analysis. They are not directly related with our result, but give us important understandings.

7.1.1 Sample Quality

In $t\bar{t}$ dilepton study, signal signature consists of some source due to top signal contamination. Therefore we need to understand and make sure how much quality of the dilepton candidates. Here, the candidate means the event after top dilepton event selection.

Tau Dilepton :

First, we look at tau dilepton events in the dilepton candidates. Even if two leptonic W decays of $t\bar{t}$ exist, Ws are not permitted to tau decay in the dilepton candidates. Most of tau decay to jet, but sometimes it decays to charged electron or muon. Real data is supposed to be including such tau decays in the dilepton candidates. This tau contamination is understood by using MC generator and CDF simulation. Table 7.1 shows the fraction of tau dilepton contamination in dilepton candidates on the $t\bar{t}$ inclusive signal MC sample. Generator is HERWIG, the top mass is assumed to be $178 \text{ GeV}/c^2$.

Jet Multiplicity :

Second, we look at the jet multiplicity in the dilepton candidates. In DLM, we consider what the leading order Feynman diagram involve two b quarks at the tree level process. But after the simulation, the signal has three or more jets, and so we need to take account of them since Dynamical Likelihood does not describe its process. Table 7.2 shows the ratio of multiplicity in

Source of generator	fraction
Top dilepton	0.87 ± 0.003
Tau dilepton	0.13 ± 0.003

Table 7.1: The fraction of tau dilepton contamination in dilepton candidate events. Top dilepton means for two Ws decay to e/e , μ/μ or e/μ . Here tau dilepton means for two Ws decay to τ/τ , τ/e or τ/μ .

the dilepton candidates. Figure 7.1 demonstrates the relative fraction of each number of jets (n jet bin) as a function of top quark mass. When we select two jets out of three or more jets in the dilepton candidates, usually we regard two leading energy jets as b quark jets. To improve the b jet selection efficiency, we use additional information of SECVTX b tag¹ at CDF. In our analysis, the first priority to select b jet is to determine by the SECVTX b tag. If there are not any tagged jet in an event, the leading E_T jets are assigned as b jets. If there is one tagged jet in an event, the jet of leading E_T except for the tagged jet is assigned as a b jet. In the double tag event, tagged jets are assigned as b jets without regard to E_T .

At this point, we determine the matching efficiency² and purity³ of the samples. Table 7.3 shows the matching efficiency and purity in the dilepton candidates. Figure 7.2 demonstrates the matching efficiency of each number of jets (n jet bin) in the dilepton candidates. The efficiency of two jet bin is always 100% since we require b jet to b parton matching to the denominator of the efficiency. Figure 7.3 demonstrates the matching efficiency and purity in the dilepton candidates. In our searching top mass region, no significant bias can be seen, so we expect no bias to top quark mass search.

jet multiplicity	fraction
exact 2 jets	0.62 ± 0.005
exact 3 jets	0.29 ± 0.005
4 jets more	0.09 ± 0.003

Table 7.2: The ratio of multiplicity in dilepton candidate events.

¹The silicon vertex b jet tag algorithm (SVX tagging) searches for the displacement of the secondary vertex due to B hadron decays to the primary vertex of the event within a jet [55],[56]. It uses tracks which are within $\Delta R < 0.4$ of the jet axis and have hits in the silicon detector.

²The efficiency of which b jet is identified correctly. In principle, we can not distinguish b jet from other light quark jet and gluon jet without special technique.

³The event purity of which the candidates have assumed signature of leading order matrix element, i.e two b jets, two e or μ leptons and \cancel{E}_T .

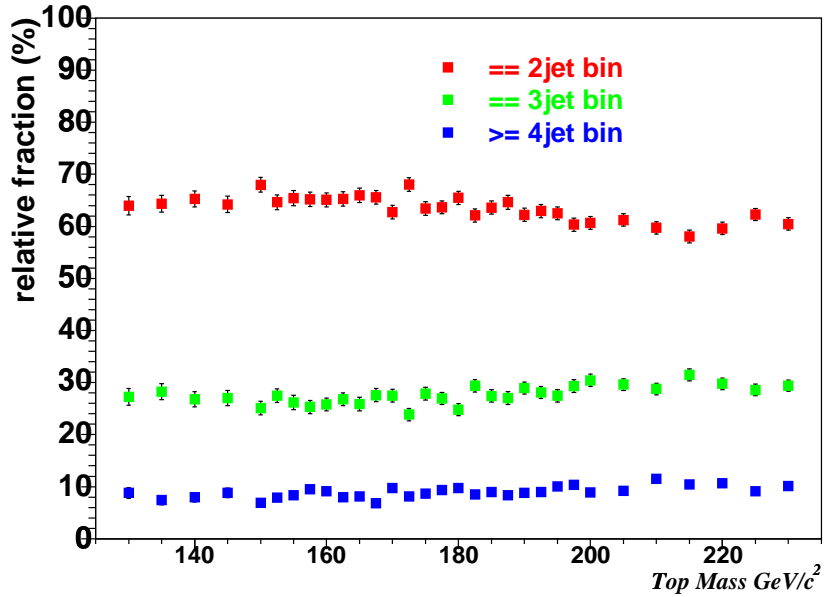


Figure 7.1: The relative fraction of each jet bin as a function of top quark masses in dilepton candidate events.

	efficiency	denominator
matching efficiency	0.88 ± 0.003	dilepton events
selected 2 jets == 2 <i>b</i> jets	0.8 ± 0.004	dilepton events
	ratio	denominator
purity (<i>above</i> $\times \epsilon_{dil}$)	0.69 ± 0.005	dilepton candidates

Table 7.3: The matching efficiency and purity in the dilepton candidates. In denominator column, dilepton events means for two *W*s decay to e/e , μ/μ or e/μ at generator level. Whereas dilepton candidates means including that two *W*s decay to τ/τ , τ/e or τ/μ additionally. ϵ_{dil} corresponds to the fraction of top dilepton in Table 7.1.

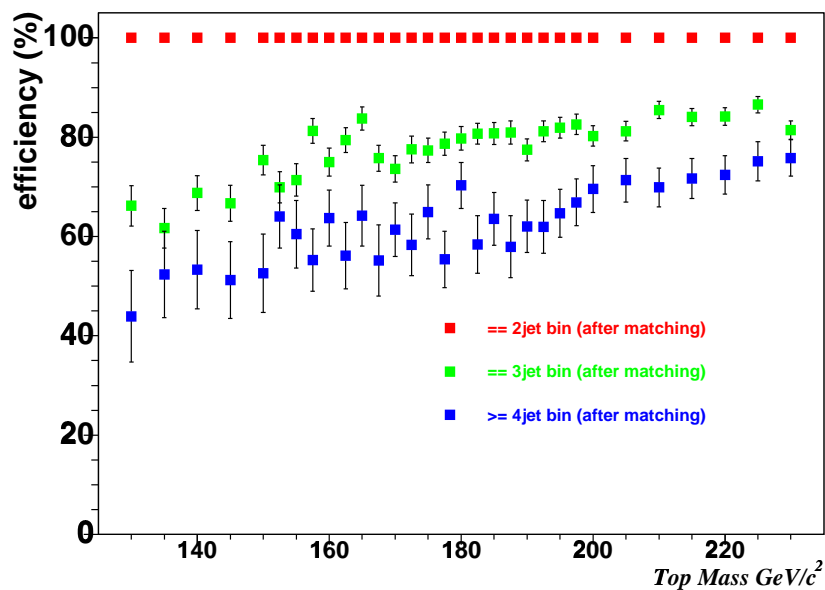


Figure 7.2: The matching efficiency of each number of jet as a function of top quark masses.

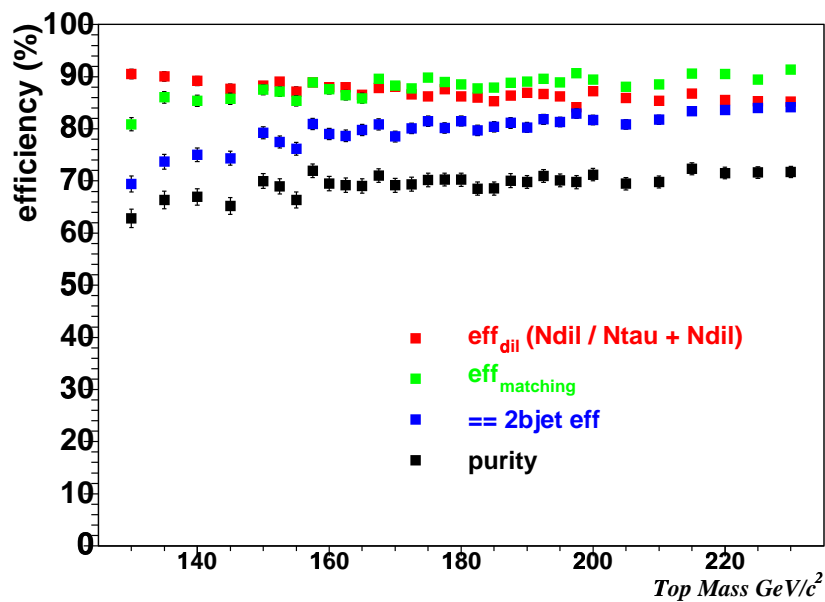


Figure 7.3: The matching efficiency and purity in the dilepton candidates as a function of top quark masses.

7.2 Pull Width

When we perform pseudo experiment with full simulation, we could obtain larger pull width than 1. Since we only consider leading order matrix element of $t\bar{t}$ production and its decay, the other process i.e. ISR or FSR, tau decay and backgrounds, violate its assumption. As a result, Dynamical Likelihood shape doesn't represent statistics properly, so that they make pull width larger than 1. In this subsection, we present such effects to pull width.

Neutrino Kinematic Weight :

We need to take account of neutrino kinematics weight. As we described in the previous subsection 4.1.5, neutrino kinematics weight is convoluted to Dynamical Likelihood to remove bad solution effect. This weight would involve cross section information, so it might be correlated to Dynamical Likelihood based on differential cross section of top event. Table 7.4 shows the comparison of neutrino kinematics weight to pull width. We observe 0.1 difference between without and with weight.

Jet Multiplicity :

We consider jet multiplicity. High jet multiplicity, especially more than three jets, strongly violate assumption of the leading order matrix element. Table 7.5 shows the comparison of jet multiplicity to pull width. We observe larger pull width in increasing number of tight jets.

Lepton Type :

We consider lepton type resolution. Table 7.6 shows the comparison of two lepton combinations to pull width. We do not observe any significant difference

Jet Angle :

We consider jet angle resolution. We use jet direction transfer function, and they include the resolution of direction ambiguity. Table 7.7 shows the comparison of direction transfer function to pull width. We do not observe any significant difference.

Mismatched Jet Event :

We consider mismatched jet event. Even if it is a signal dilepton event, b jets might not be identified perfectly, because gluon jet and b jet can not be separated without any technique such like b tagging. We compare pure sample⁴ and full sample⁵ in order to understand effect of unmatched jet event. Table 7.8 shows the effect of unmatched event to pull width.

⁴Pure sample means jet to b quark matched event after simulation

⁵Full sample condition is corresponding to data candidates. Sometimes, the selected jet might be gluon jet.

In applying data, we employ 1.323 pull width calibration constant. Moreover, in sub-section 6.1.6, the discussion of the background fraction systematic uncertainty explain the background fraction dependence of pull width. If background event is increasing in sample composition of pseudo experiment set, the possibility of breaking the assumption for Dynamical Likelihood is also increasing. At the end, we need to correct the statistical uncertainty due to accurately measurement. The largest source of breaking the assumption might be coming from background event, and also other sources exist in such this discussion.

weight	pull width
with weight	1.09 ± 0.04
without weight	0.99 ± 0.04

Table 7.4: The comparison of with/without neutrino kinematics weight. The sample is pure sample which is perfectly matched (jet to parton) events.

N_{jet}	pull width
exact 2 jet	1.04 ± 0.05
exact 3 jet	1.10 ± 0.08
4 jet more	1.14 ± 0.17
Total	1.09 ± 0.04

Table 7.5: The comparison of jet multiplicity. The sample is pure sample which is perfectly matched (jet to parton) events.

lepton type	pull width
ee	1.06 ± 0.08
$e\mu$	1.10 ± 0.05
$\mu\mu$	1.05 ± 0.07
Total	1.09 ± 0.04

Table 7.6: The comparison of various lepton pairs. The sample is pure sample which is perfectly matched (jet to parton) events.

direction transfer function	pull width
with function (our original)	1.09 ± 0.04
without function	1.08 ± 0.04

Table 7.7: The comparison of with/without direction transfer function. The sample is pure sample which is perfectly matched (jet to parton) events.

sample	pull width
pure sample	1.09 ± 0.04
full sample	1.18 ± 0.05

Table 7.8: The comparison between using pure sample and full sample of dilepton event.

7.3 Blind Test

After constructing mapping function including background contribution, we can confirm our analysis machinery by CDF blind test⁶. To apply the blind test to our top quark mass measurement, we plot the difference of between true and our reconstructed value in Fig. 7.4. Samples (1 - 3) were informed to be produced by using HERWIG Monte Carlo, samples (4 - 5) were informed to be produced by using PYTHIA Monte Carlo. The error of residual in PYTHIA sample is additionally convoluted with Generator systematic uncertainty ($0.6 \text{ GeV}/c^2$) since our mapping function to reconstruct top quark mass is produced by HERWIG samples. Good agreement can be seen between our reconstruction and blinded input top mass within the statistical uncertainty.

⁶To investigate each analysis method, CDF Top Quark Mass Working Group had generated 5 “blind samples”. Blind sample by definition, blinds its true top quark mass. Analysts of top quark mass were not informed input top masses and which Monte Carlo generator was used for those samples.

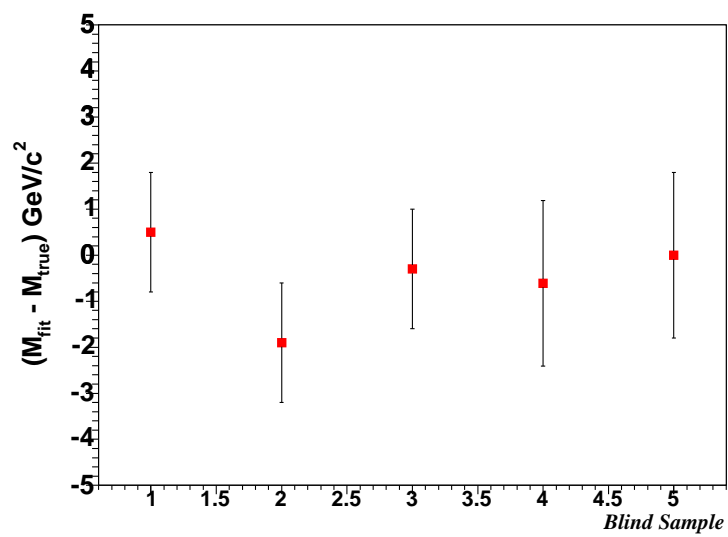


Figure 7.4: Residuals of blind samples.

Chapter 8

Conclusion

8.1 Conclusion

We have improved the top quark mass measurement by acquiring large number CDF data and obtaining 33 top dilepton candidate events and by reducing the largest systematic uncertainty, especially jet energy scale. The first DLM applying to CDF Run II data in top dilepton channel is done, and thus the top quark mass is measured using data taken between March 2002 and September 2004. The integrated luminosity is corresponding to 340.5pb^{-1} of CDF data. The final fit and corrected result of our top quark mass measurement is

$$M_t = 166.6_{-6.7}^{+7.3}(\text{stat.}) \pm 3.2(\text{sys.}) \text{ GeV}/c^2$$

totally,

$$M_t = 166.6_{-7.4}^{+8.0}(\text{stat.}) \text{ GeV}/c^2$$

Good agreement is seen for our measurement and other CDF dilepton measurement in Fig. 8.1.

Last updated top quark mass measurement in Tevatron experiment, Run I+II CDF + D \emptyset dilepton + lepton + jets + all hadronic [57] is

$$M_t = 172.7 \pm 1.7(\text{stat.}) \pm 2.4(\text{sys.}) = 172.7 \pm 2.9 \text{ GeV}/c^2$$

As a near future of CDF top quark mass measurement, we expect the measurement for 1fb^{-1} of CDF data. CDF+D \emptyset should attain an uncertainty of about $2\text{ GeV}/c^2$ on the top quark mass. At the end, CDF+D \emptyset should attain an uncertainty of about $1.5\text{ GeV}/c^2$ on the top quark mass by the end of Run II in 2009.

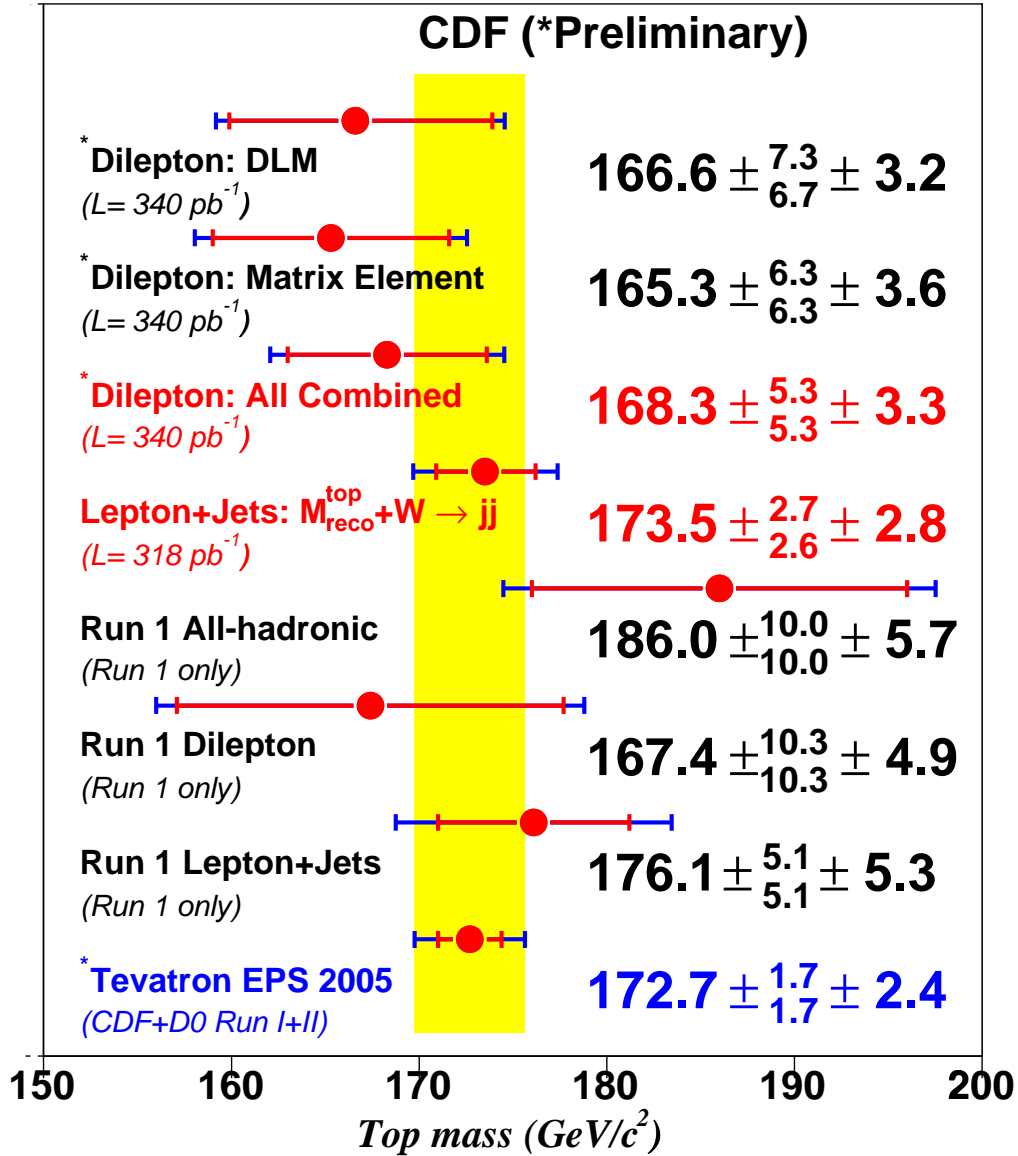


Figure 8.1: The Tevatron Run II top mass measurements in dilepton channel. All results are consistent within the uncertainties.

Appendix A

Pseudo Experiments

We would often like to characterize the expected performance of the analysis in a statistically meaningful way, for example to get the expected statistical error, or to understand the shift in the top mass caused by a given systematic effect. We use large ensembles of sets of Monte Carlo events to perform the pseudo experiments. Usually, the numbers of one set should be corresponding to the number of events to get full analysis result with real data. In this thesis case, such numbers is 32 events after full event selection and additional cuts (See Table 4.1). The full analysis machinery is used on each pseudo experiment, and the top mass, with associated uncertainties, is extracted.

In top mass measurement, each pseudo experiment consists of the assumed numbers of signal events and the expected numbers of background events from the estimation of cross section study. And the number of background events are fluctuated by Poisson statistic around each expectation number in an pseudo experiment test. Then there are two ways to chose the numbers for signal assumption in our analysis as following.

6.1 pb case :

Without depending to top cross section measurement, we need to be able to determine top quark mass. This requirement are imposed as first check of the analysis or sensitivity check statistically in CDF Top group. In this case, we assume top quark cross section as 6.1pb and the numbers of signal events are fluctuated by Poisson statistic around the expectation number in an pseudo experiment test. In this thesis, we employ the mean value of this Poisson fluctuation as 15.66. This denote the sum of the mean value of signal and backgrounds is consistent with 32 in an pseudo experiment.

Data case :

In assuming to take 32 candidate events, we determine correction function (mapping function) and factor and further expect statistical uncertainty (pull width calibration). In this case, we fixed the total number of one pseudo experiment set with 32 events. This denote the number of signal events is consistent with total fixed number (32) minus sum of fluctuated background numbers (mean = 8.9).

Main role of the pseudo experiment is to understand the significant systematic shift of our measurement by using large ensembles. With performing the pseudo experiments to measure the top mass shift due to a particular systematic source, we would like to understand the top mass bias on our likelihood determination and somehow correct them (by using mapping function) and compensate these effect. Second role is to understand the accuracy of our attached statistical uncertainty from likelihood calculation. To evaluate it we decide “pull” variable and concern the pull distribution. The “pull” is determined pseudo experiment by pseudo experiment and the variable “pull” is defined as,

$$pull = \frac{M_{rec} - M_{input}}{\sigma} \quad (\text{A.1})$$

where M_{rec} and M_{input} are reconstructed top mass and input top mass respectively. If $M_{rec} > (<) M_{input}$, σ is defined as $\sigma^{-(+)}$. In the case of an asymmetric uncertainty, variable pull is symmetries properly. The Gaussian fit to the pull distribution gives a mean value and pull width value. This pull width value denote the actual deviation per our attached statistic uncertainty, it implies the accuracy of our attached statistic uncertainty. If our uncertainty is statistically correct, the value of pull width has to be 1.0, if not, we need further correction to statistic uncertainty to evaluate true uncertainty. This procedure is so-called as “pull width calibration” throughout this thesis.

Bibliography

- [1] <http://www.fnal.gov>.
- [2] CDF Collaboration. The cdf ii detector technical design report. *FERMILAB-Pub-96/390-E*, 1996.
- [3] J.F.de Troconiz and F.J.Yndurain. *Phys. Rev.*, **D65**(093002), 2002.
- [4] S.Eidelman *et al.* <http://particleadventure.org/particleadventure/>
- [5] J.J.Thomson. *Nature*, 44(293), 1897.
- [6] D.Gross and F.Wilczek. Asymptotically free gauge theory. *Phys. Rev. Lett.*, **30**(1343), 1973.
- [7] R.P.Feynman. Qed the strange theory of light and matter. *Princeton Science Library*, 1985.
- [8] P.W.Higgs. *Phys. Lett.*, **12**(132), 1964.
- [9] CDF Collaboration. *Phys. Rev Lett.*, **93**(142001), 2004.
- [10] CDF Collaboration. *Phys. Rev.*, **D71**(052003), 2005.
- [11] CDF Collaboration. *Phys. Rev.*, **D71**(072005), 2005.
- [12] CDF Collaboration. *Phys. Rev.*, **D72**(032002), 2005.
- [13] CDF Collaboration. *hep-ex/0504053*, 2005.
- [14] CDF Collaboration. *Accepted PRL*, *hep-ex/0510049*.
- [15] CDF Collaboration. *Accepted PRD*, *hep-ex/0510048*.
- [16] CDF Collaboration. *Submitted to PRD*.
- [17] CDF Collaboration. *Phys. Rev.*, **D71**(012005), 2005.
- [18] CDF Collaboration. *Phys. Rev. Lett.*, **95**(022001), 2005.

- [19] CDF Collaboration. *Phys. Rev. Lett.*, **95**(102002), 2005.
- [20] CDF Collaboration. *Accepted PRL*, *hep-ex/0510063*.
- [21] CDF Collaboration. *Accepted PRD*, *hep-ex/0510065*.
- [22] R.Bonciani *et al.* *Nucl.Phys.*, **B529**(424), 1998.
- [23] J.Iliopoulos and L.Maiani S.L.Glashow. *Phys. Rev.*, **D2**(1285), 1985.
- [24] S.Baroiant *et al.* Proceedings 4th international workshop on very high multiplicity physics, alushta, crimea, ukraine. *FERMILAB-CONF-03/322-E*.
- [25] S. Willenbrock. *arXiv:hep-ph/0211067*.
- [26] LEP Electroweak Working Group. *Phys. Lett.*, **B565**(61), 2003.
- [27] <http://lephiggs.web.cern.ch/LEPHIGGS/www/Welcome.html>.
- [28] F. Abe *et al.*[CDF Collaboration]. *Nucl. Instrum. Meth.*, **A271**(387), 1988.
- [29] A.Sill *et al.* *Nucl. Instrum. Meth.*, **A447**(1), 2000.
- [30] T.Affolder *et al.* *Nucl. Instrum. Meth.*, **526**(249), 2004.
- [31] F.Bedeschi *et al.* *Nucl. Instrum. Meth.*, **A268**(50), 1988.
- [32] L.Balka *et al.* *Nucl. Instrum. Meth.*, **A267**(272), 1988.
- [33] S. Bertolucci *et al.* *Nucl. Instrum. Meth.*, **A267**(301), 1988.
- [34] K.Byrum *et al.* *Nucl. Instrum. Meth.*, **A364**(144), 1995.
- [35] F.Abe *et al.* *Phys. Rev. Lett.*, **73**(2662), 1994.
- [36] K.Byrum *et al.* *Nucl. Instrum. Meth.*, **A268**(46), 1988.
- [37] G.Ascoli *et al.* *Nucl. Instrum. Meth.*, **A268**(33), 1988.
- [38] T.Dorigo *et al.* *Nucl. Instrum. Met.*, **A461**(560), 2001.
- [39] W.Wagner *et al.* Fermilab-conf-02-269-e, international euophysys conference on high-energy physics (hep 2001), budapest, hungary. 12-18 Jul 2001.
- [40] B.Angelos *et al.* International conference on computing in high-energy physics and nuclear physics (chep 2000), padova, italy. 7-11 Feb 2000.
- [41] P.Canal *et al.* *IEEE Trans. Nucl. Sci.*, **47**(240), 2000.

- [42] T. Affolder *et al.* *Phys. Rev.*, **D64**(032001), 2001.
- [43] T. Affoldere *et al.* *Phys. Rev.*, **D63**(032003), 2001.
- [44] K.Kondo. *J. Phys. Soc. Jpn.*, **57**(4126), 1988.
- [45] K.Kondo. *J. Phys. Soc. Jpn.*, **60**(836), 1991.
- [46] T.Chikamatsu S.H.Kim, K.Kondo. *J. Phys. Soc. Jpn.*, **62**(1177), 1993.
- [47] K.Kondo. Dynamical likelihood method for reconstruction of quantum process. *hep-ex/0508035*.
- [48] K. Hagiwara. *Phys. Rev.*, **D66**(010001), 2002.
- [49] Roger J.N. Phillips Vernon D. Barger. Collider physics p102.
- [50] R.Tsuchiya *et al.* M.Tecchio. *CDF intenal note*, (7851), 2005.
- [51] J.-F. Arguin and P.K.Sinervo. b-jets energy scale uncertainty from existing experimental constraints. *CDF intenal note*, (7252), 2004.
- [52] J. Pumlin *et al.* *JHEP*, 0207(012,hep-ph/0201195), 2002.
- [53] D. Stump *et al.* *JHEP*, 0210(046,hep-ph/0303013), 2003.
- [54] D. Gerdes *et al.* Measurement of the top quark mass in the dilepton channel using the differential cross-section. *CDF intenal note*, (7583), 2005.
- [55] T. Affolder *et al.* *Phys. Rev.*, **D64**(032002), 2001.
- [56] D.Acosta *et al.* *submitted to Phys. Rev*, 2004.
- [57] Tevatron Electroweak Working Group CDF Collaboration, D0 Collaboration. Combination of cdf and d0 results on the top quark mass. *hep-ex/0507091*, 2005.